Rossby Wave Packets And Their Role In Temperature Extremes

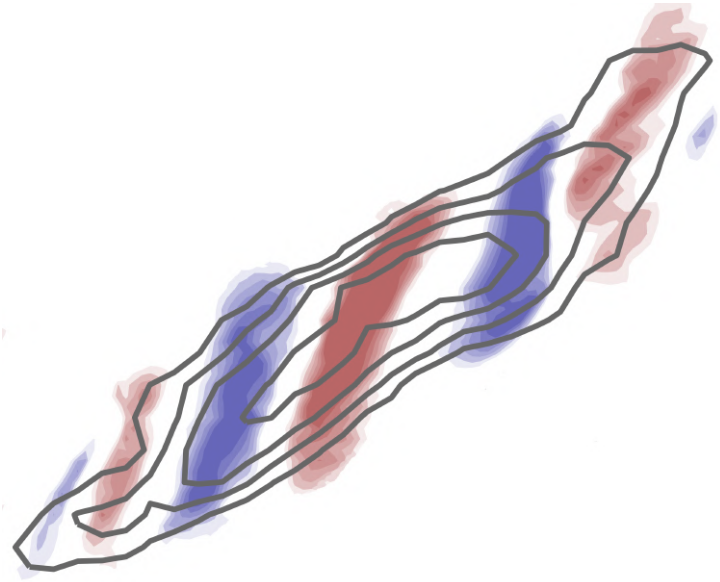

Dissertation submitted
for the award of the title

"Doctor of Natural Sciences"

to the Faculty of Physics, Mathematics and Computer Science
of Johannes Gutenberg University
in Mainz

Georgios Fragkoulidis

Born in Athens, Greece

JG|U

JOHANNES GUTENBERG
UNIVERSITÄT MAINZ

Mainz, July 2019

Date of oral examination: 23.10.2019

Summary

Eastward propagating Rossby wave packets (RWPs) are a dominant feature of the mid-latitude circulation. They are reflected in the upper-tropospheric meridional wind field as a longitudinally-confined group of northerlies and southerlies. Their documented relevance to weather extremes necessitates the development of diagnostic methods that can identify and investigate their properties locally in space and time. The overarching goal of this work is to develop such diagnostics, investigate the local properties of RWPs and quantify their role in temperature extremes.

The diagnostic methods are based on the analytic signals of the filtered upper-tropospheric meridional wind and its envelope function along latitude circles. RWP properties like the local amplitude, wavelength, phase velocity, and group velocity collectively provide the main characteristics of the upper-tropospheric flow in the mid-latitudes at any instance in time, but also reveal its distinct climatological patterns. Based on them, the role of RWPs in the occurrence and duration of temperature extremes is investigated. In particular, regression analyses show that the probability for a temperature extreme in many parts of the Northern Hemisphere increases significantly with RWP amplitude; a linkage that cannot be revealed so clearly when employing non-local metrics like the Fourier amplitudes of meridional wind. The role of RWPs as large-scale upstream precursors is further emphasized in an investigation of Southeastern European hot and cold extremes.

Identifying and following the spatiotemporal evolution of RWPs also proves beneficial in exploring the lifetime of the 2003 and 2010 heat waves in Western Europe and Russia respectively. In doing so, it is shown that a single one or several successive non-circumglobal RWPs can create the large-scale environment where temperature anomalies can amplify and — in combination with physical processes of smaller scale — lead to extreme events. During such cases of persistent temperature extremes the role of below-normal RWP phase velocity is found to be critical. The combined effect of RWP amplitude and phase velocity in the occurrence and duration of temperature extremes is quantified using a sufficiently large sample of short-lived and persistent events in 40 years of reanalysis data (1979–2018).

Global climatologies of local RWP amplitude, phase velocity and group velocity are produced for the first time and reveal the major differences in the upper-tropospheric circulation of the Northern and Southern Hemispheres. Moreover, important aspects of the seasonal variability in particular regions are discussed. Finally, an investigation of medium-range forecast biases of the Northern Hemisphere RWP properties using 6 years of ECMWF operational forecasts (2013–2018) suggests possible implications for the practical predictability of temperature extremes occurrence and duration.

Overall, this work contributes to the overarching goal of improving our understanding of RWPs and temperature extremes. The aforementioned findings and the novel diagnostics will be beneficial for future research on the processes that affect the RWP evolution and its implications to the occurrence and predictability of extremes at both the weather and climate time scales.

Contents

List of Publications **iii**

1 Introduction **1**
1.1 Rossby waves . . . 1
1.2 Rossby wave packets . . . 4
1.3 Role of Rossby wave packets in temperature extremes . . . 9
1.4 Objectives and outline of this work . . . 13

2 Data and methods **15**
2.1 Overview . . . 15
2.2 Anomaly fields computation . . . 15
2.3 Spatial filtering in the meridional wind field . . . 16

3 Linking Northern Hemisphere temperature extremes to Rossby wave packets **20**
3.1 Introduction . . . 21
3.2 Data and methods . . . 23
3.2.1 Reanalysis data . . . 23
3.2.2 Computation of anomalies . . . 23
3.2.3 Diagnosing Rossby wave packets . . . 24
3.2.4 Heat wave index . . . 25
3.3 Connection between upper-tropospheric waviness and lower-tropospheric temperature anomalies . . . 26
3.3.1 Analysis for a European region in summer . . . 26
3.3.2 Extension to the entire Northern Hemisphere extratropics . . . 29
3.3.3 Near-surface temperature anomalies . . . 31
3.4 The heat waves of 2003 and 2010 . . . 33
3.5 Summary and discussion . . . 38

4 Synoptic circulation patterns during temperature extremes in south-eastern Europe **44**
4.1 Introduction . . . 45
4.2 Data and methods . . . 45
4.2.1 Data . . . 45
4.2.2 Methodology . . . 45
4.3 Results . . . 46
4.4 Conclusions . . . 50

5 Local Rossby wave amplitude, phase velocity, and group velocity: Seasonal variability and their role in temperature extremes 52
5.1 Introduction . . . 53
5.2 Data . . . 55
5.3 Diagnosis of local phase and group velocity . . . 55
5.3.1 Analytic signal and local phase . . . 55
5.3.2 Local Rossby wave phase velocity . . . 57
5.3.3 Local Rossby wave group velocity . . . 58
5.3.4 Exemplary cases . . . 60
5.4 Seasonal climatologies . . . 64
5.4.1 Northern Hemisphere . . . 65
5.4.2 Southern Hemisphere . . . 67
5.5 Role of RWP amplitude and phase velocity in temperature extremes . . 70
5.6 Summary and further remarks . . . 75
5.7 Supplemental Material . . . 77
5.7.1 Local phase diagnosis . . . 77
5.7.2 Derivatives in the "wrapped" phase function . . . 80
5.7.3 Wavelet analysis on meridional wind along a latitude circle . . . 82
5.7.4 Additional climatologies . . . 83
5.7.5 Phase velocity – RWP amplitude distribution . . . 83
5.7.6 Central European temperature extreme statistics . . . 85
5.7.7 Computation methods . . . 85

6 Medium-range forecast biases in Rossby wave packet properties 88
6.1 Introduction . . . 88
6.2 Data and methods . . . 88
6.3 Mean biases in RWP amplitude and phase velocity . . . 89
6.4 Seasonal variability in the RWP amplitude and phase velocity biases . . 92
6.5 Summary and further remarks . . . 93

7 Conclusion 95
7.1 Summary . . . 95
7.2 Outlook . . . 97

Appendix A Local wavenumber through wavelet analysis 98

List of Figures 100

List of Tables 109

Bibliography 111

Acknowledgements 122

List of Publications

Publications included as chapters in this dissertation and notes on the contributors:

- **Fragkoulidis G**, Wirth V, Bossmann P and Fink AH. 2018. Linking Northern Hemisphere temperature extremes to Rossby wave packets. *Quarterly Journal of the Royal Meteorological Society* **144**(711): 553-566, doi:10.1002/qj.3228.

  – *Contributions:* The ideas and analyses presented in this article are the result of my collaboration with the co-authors listed above as part of the "Waves to Weather" project C4. Pila Bossmann provided the heat wave index (section 3.2.4) and produced Fig. 3.9. I did all the other analyses and drafted the manuscript. Andreas Fink had invaluable comments throughout the process and contributed to the revision of the manuscript. Volkmar Wirth had the initial idea for section 3.3 that motivated the work, supervised the analyses, and contributed to the revision of the manuscript.

- **Fragkoulidis G**, Wirth V. 2018. Synoptic circulation patterns during temperature extremes in southeastern Europe. *Proceedings of the 14th International Conference on Meteorology, Climatology and Atmospheric Physics, Alexandroupoli, Greece*, ISBN: 978-960-98220-4-6.

  – *Contributions:* The analyses in this publication were conceived and conducted by me. I also produced the figures and drafted the manuscript, which was then revised by Volkmar Wirth.

- **Fragkoulidis G**, Wirth V. 2019. Local Rossby wave amplitude, phase velocity, and group velocity: Seasonal variability and their role in temperature extremes. *Journal of Climate. submitted.*

  – *Contributions:* The need for a local phase velocity diagnostic became evident in the two aforementioned publications. The basic mathematical principle used in this regard was developed by (Gabor 1946) in view of analyzing the instantaneous frequency in time-varying signals. I then developed the methodology steps for this work with invaluable input from Volkmar Wirth. I conducted all the analyses and drafted the manuscript which was then revised by Volkmar Wirth.

Other publications:

- Sprenger M, **Fragkoulidis G**, Binder H, Croci-Maspoli M, Graf P, Grams CM, Knippertz P, Madonna E, Schemm S, Škerlak B, Wernli H. 2017. Global climatologies of Eulerian and Lagrangian flow features based on ERA-Interim. *Bulletin of the American Meteorological Society* **98**(8): 1739–1748, doi:10.1175/BAMS-D-15-00299.1.

- Ghinassi P, **Fragkoulidis G**, and Wirth V, 2018. Local Finite-Amplitude Wave Activity as a diagnostic for Rossby Wave packets. Monthly Weather Review **146**(12): 4099-4114, doi:10.1175/MWR-D-18-0068.1.

- Zschenderlein P, **Fragkoulidis G**, Fink AH, Wirth V. 2018. Large-scale Rossby wave and synoptic-scale dynamic analyses of the unusually late 2016 heatwave over Europe. Weather **73**(9): 275-283. doi:10.1002/wea.3278.

Chapter 1

Introduction

1.1 Rossby waves

Rossby waves are a dominant feature of the large-scale circulation in the mid-latitude upper-troposphere (Rossby and Collaborators 1939; Rossby 1940; Haurwitz 1940). The basic dynamics of Rossby waves in a single-layer barotropic flow were originally formulated by Rossby and Collaborators (1939), effectively illustrating their driving mechanism and providing some of their basic properties.

In the following, I assume flow with small variations in latitude on a plane that is tangent to the surface of the Earth at latitude ϕ_0. In this so-called "β-plane" approximation, the Coriolis parameter varies in the y-direction and is given by: $f = f_0 + \beta y$, where $f_0 = 2\Omega sin\phi_0$, where Ω is the angular velocity of the Earth, and $\beta = \partial f/\partial y = (2\Omega cos\phi_0)/a$ (with a the radius of the Earth). In this case, the horizontal momentum equation in conservative conditions is given by:

$$\frac{\partial \boldsymbol{u}}{\partial t} + (\boldsymbol{u} \cdot \nabla)\boldsymbol{u} + f\boldsymbol{k} \times \boldsymbol{u} = -\frac{1}{\rho}\nabla_z p \tag{1.1}$$

where $\boldsymbol{u} = (u, \upsilon)$ is the two dimensional wind field (u: zonal wind, υ: meridional wind) and $\boldsymbol{k}$ is the unit vector in the direction perpendicular to the plane.

For large-scale motions in the atmosphere the characteristic horizontal velocity U=10ms^{-1}varies at a length scale L=1000 km. Moreover, the Coriolis parameter in the mid-latitudes is in the order of 10^{-4}s^{-1}. In this case, the ratio of the advective term (second term in the l.h.s) to the Coriolis term in (1.1) is small; a scaling that is formally described by the Rossby number: $R_o \equiv U/(fL)$. If in addition, U does not vary much with time, then the first term in the l.h.s is also small and the effects of Earth's rotation become important. The resulting balance between the Coriolis and pressure gradient forces, is known as geostrophic balance:

$$fu_g = -\frac{1}{\rho a}\frac{\partial p}{\partial \phi}, \quad f\upsilon_g = -\frac{1}{\rho a cos\phi}\frac{\partial p}{\partial \lambda} \tag{1.2}$$

where u_g, υ_g represent the geostrophic wind components and λ denotes the longitude. It can be seen that for the Northern Hemisphere ($f > 0$) the flow in a low pressure system is anticlockwise and the flow in a high pressure system is clockwise. Defining

the geostrophic streamfunction as: $\psi \equiv p/(f_0\rho_0)$, (1.2) becomes:

$$u_g = -\frac{\partial \psi}{\partial y}, \quad \upsilon_g = \frac{\partial \psi}{\partial x}, \tag{1.3}$$

and the vertical component of vorticity, ζ, is given by:

$$\zeta = \boldsymbol{k} \cdot \nabla \times \boldsymbol{\upsilon} = \frac{\partial \upsilon}{\partial x} - \frac{\partial u}{\partial y} = \nabla_z^2 \psi \tag{1.4}$$

In the barotropic model the atmosphere is a single homogeneous incompressible fluid layer of depth h, assumed here to be constant (zero wind divergence). In this case, the potential vorticity is equal to the absolute vorticity:

$$q \equiv \zeta + f_0 + \beta y \tag{1.5}$$

and is conserved under unforced horizontal adiabatic motion on the β-plane (e.g., Holton and Hakim 2013):

$$\frac{D_h q}{Dt} = \frac{D_h}{Dt}(\zeta + f_0 + \beta y) = 0 \quad \Rightarrow \tag{1.6}$$

$$\Big(\frac{\partial}{\partial t} + u\frac{\partial}{\partial x} + \upsilon\frac{\partial}{\partial y}\Big)\zeta + \beta\upsilon = 0 \tag{1.7}$$

The flow can be assumed to consist of a constant zonal basic state, $\bar{u}$, and a small horizontal perturbation, $(u', \upsilon') = (-\partial\psi'/\partial y, \partial\psi'/\partial x)$:

$$u = \bar{u} + u' = \bar{u} - \partial\psi'/\partial y, \quad \upsilon = \upsilon' = \partial\psi'/\partial x, \quad \zeta = \zeta' = \nabla^2\psi' \tag{1.8}$$

Linearizing (1.7) yields:

$$\Big(\frac{\partial}{\partial t} + \bar{u}\frac{\partial}{\partial x}\Big)\nabla^2\psi' + \beta\frac{\partial \psi'}{\partial x} = 0, \tag{1.9}$$

Next, a solution of the oscillatory form:

$$\psi' = Re[\tilde{\psi}e^{i(kx+ly-\omega t)}], \tag{1.10}$$

is assumed, where $\tilde{\psi}$ is the amplitude, k and l are the zonal and meridional wavenumbers, and ω is the angular frequency. Substituting (1.10) into (1.9) yields the *dispersion relation*:

$$\omega = \bar{u}k - \frac{\beta k}{k^2 + l^2} \tag{1.11}$$

From (1.11) one can obtain the zonal phase and group velocities, c_p and c_g respectively, of this wave motion:

$$c_p \equiv \frac{\omega}{k} = \bar{u} - \frac{\beta}{k^2 + l^2}, \quad c_g \equiv \frac{\partial \omega}{\partial k} = \bar{u} + \frac{\beta(k^2 - l^2)}{(k^2 + l^2)^2} \tag{1.12}$$

Since phase velocity depends on the wavenumber Rossby waves are *dispersive*. More specifically, in the absence of $\bar{u}$ the phase velocity is always negative (westward) and its

magnitude increases with the zonal wavelength. On the other hand, group velocity can either be negative or positive and gets more eastward with increasing zonal wavelength. Moreover, it follows from (1.12) that:

$$c_g = c_p + \frac{2\beta k^2}{(k^2 + l^2)^2}. \tag{1.13}$$

Therefore, the group velocity is always larger than the phase velocity; a property of the Rossby waves known as *downstream development* (Simmons and Hoskins 1979). More on group velocity will follow in the next section, where the notion of wave packets is introduced.

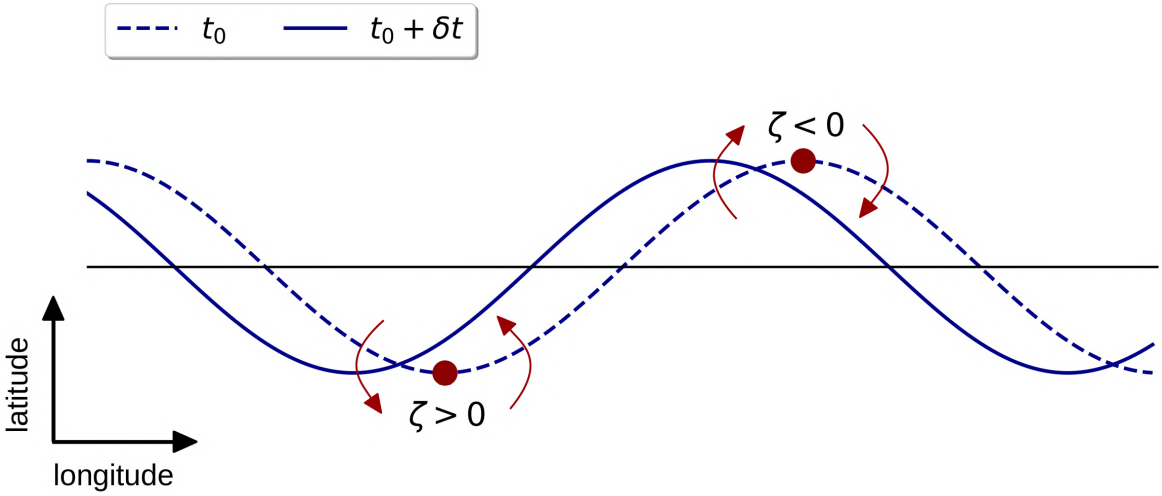

Fig. 1.1: *Schematic depiction of the Rossby wave mechanism on a β-plane. See description in the text.*

Figure 1.1 depicts the underlying mechanism of Rossby wave generation based on the above considerations. Shown is a material line of a barotropic fluid on the β-plane at t_0 (dashed blue line), that has been perturbed away from its initial fixed latitude (black solid line; where $\zeta = 0$ and the absolute vorticity is fixed). The red dots depict two fluid parcels that are displaced to the north and south of the initial latitude. A northward displaced parcel ($+y$) ends in a region of higher planetary vorticity which, due to absolute vorticity conservation ($\zeta + f_0 + \beta y$), leads to the generation of negative relative vorticity. For a β-plane in the Northern Hemisphere, this anticyclonic anomaly is tantamount to a clockwise flow that advects the material line in a way that the wave phase propagates westward at $t_0 + \delta t$ (blue solid line). The same applies for a southward displacement and the induced cyclonic flow anomaly. Overall, the pattern that results from this initial displacement moves westward and constitutes a Rossby wave. It can thus be seen that the restoring force for Rossby waves is the change of the Coriolis parameter with latitude (meridional gradient of planetary vorticity; β-effect). Therefore, the underlying drivers are the spherical geometry and rotation of the Earth.

Manifestations of Rossby waves in more complex models of the atmosphere have been investigated in the decades following the original formulations by C. G. Rossby (e.g., Dickinson 1978). Except from freely propagating Rossby waves, previous studies

have investigated the excitation and evolution of (stationary) Rossby waves to topographic and thermal forcing (Held 1983). Moreover, conceptual ideas about their refraction and reflection in various background flow configurations have been postulated (e.g., Hoskins and Karoly 1981; Hoskins and Ambrizzi 1993). Regarding the considerably more complex situation of the real atmosphere, such theoretical concepts are inevitably violated to some extent. Nevertheless, as will be shown in the next section, Rossby wave theory continues to provide a solid background and intuition for the observed large-scale motions in the atmosphere.

1.2 Rossby wave packets

The mathematical expression of group velocity was introduced in the previous section. Group velocity is a notion that appears when Rossby waves are not purely sinusoidal, but organize in wave packets (e.g., Vallis 2017). In this case, the velocity at which a packet travels is the group velocity and, as shown before, exceeds the velocity of the individual wave crests (phase velocity). An important feature of the group velocity is that it constitutes the velocity with which information and energy in a Rossby wave propagate (e.g., Pedlosky 2003; Cai and Huang 2013).

A one-dimensional wave packet can be formulated as :

$$\upsilon(x,t) = E(x,t)cos(kx - \omega t), \tag{1.14}$$

where E is the envelope of the meridional wind and $cos(kx - \omega t)$ is the carrier wave. Figure 1.2 gives an example of a wave packet (blue solid line). The envelope modulates the wave on a scale that is larger than the wavelength of the carrier wave and it can be used to define the local amplitude of the Rossby wave packet.

The concept of Rossby wave packets (RWPs) is particularly relevant in the real atmosphere where it can provide a more appropriate description of Rossby waves. The reason is that the upper-tropospheric circulation in the mid-latitudes tends to organize in transient RWPs that extend over a longitudinal range and propagate eastward (e.g., Lee and Held 1993; Chang 1993). Cases of a single circumglobal sinusoidal Rossby wave essentially never occur. If anything, structures that resemble a circumglobal Rossby wave may appear in correlation maps that depict teleconnection patterns or temporally averaged fields of the upper troposphere meridional wind field (Branstator 2002; Kornhuber *et al.* 2017a). In the other end, the downstream development of disturbances in the mid-latitude flow (e.g., Orlanski and Chang 1993) ensures that solitary troughs or ridges are also highly improbable. It is therefore meaningful to think in terms of RWPs when considering the circulation at synoptic to planetary scales.

Figures 1.3 and 1.4 show two instances of the upper-tropospheric circulation in late August 2016 using ERA5 reanalysis data [Copernicus Climate Change Service (C3S) 2017], where anomaly fields refer to deviations from the 1979–2018 mean climatology; computed as described later in section 2.2. The presented plots collectively provide a representative paradigm of a transient RWP and the imprint of its progression in relevant meteorological fields. On 20 August, small amplitude undulations in the upper-tropospheric flow over North America and the North Atlantic are evident

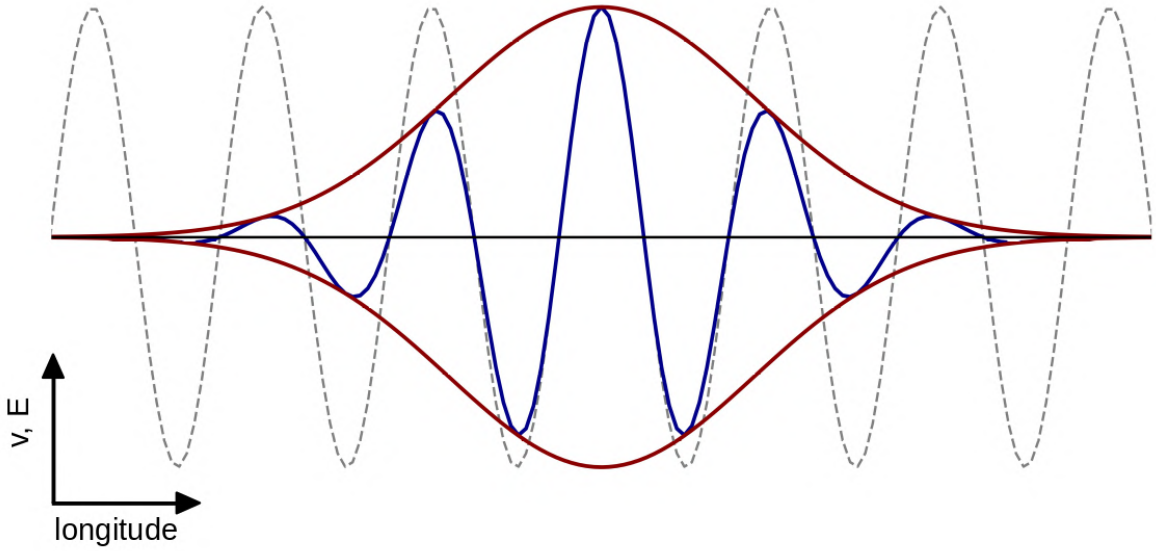

Fig. 1.2: *Schematic depiction of a one-dimensional sinusoidal Rossby wave (gray dashed line) and a Rossby wave packet (blue solid line) modulated by an envelope (E; red solid line).*

in the fields of potential vorticity (PV) anomaly*, meridional wind anomaly, and the jet (Figs. 1.3a,b,e). This area of relatively increased waviness is reflected in the envelope of meridional wind at 300 hPa (Fig. 1.3d; computed as described in section 5.3). Three days later, this RWP has amplified substantially and is located over the North Atlantic (Fig. 1.4d). The jet stream has acquired a significant meridional component and a succession of troughs and ridges is evident in the fields of PV and geopotential height (Z) at 500 hPa anomaly (Figs. 1.4a,b,c,e). As seen by the enhanced temperature anomaly at 850 hPa field (Figs. 1.4b,c), the resulting synoptic situation over Western Europe was associated with the early stages of a heat wave in Western Europe (Zschenderlein *et al.* 2018). Over the North Pacific, the axis of the PV anomaly filaments on 20 August has a northeast–southwest tilt and is associated with a nonlinear flow configuration that is not translated into enhanced RWP amplitude (Fig. 1.3d). On 23 August, however, a more archetypal waviness in the flow forms a well-shaped RWP at that location (Fig. 1.4d).

To obtain improved understanding, the evolution of RWPs has been increasingly investigated in the past few decades. Their occurrence has been reported and investigated in both observations and a hierarchy of models (Lee and Held 1993). Studies have examined the role of RWPs in storm track activity, weather extremes, and predictability (Hakim 2003; Wirth and Eichhorn 2014; O'Brien and Reeder 2017; Grazzini and Vitart 2015; Quinting and Vitart 2019; Baumgart *et al.* 2019). In a recent review, Wirth *et al.* (2018) summarize the key developments in understanding RWPs and present the state of the art and open questions. The introductory sections in chapters 3–6 provide a more detailed account in this regard.

Important properties of the RWPs are their amplitude, wavelength, phase veloc-

*The calculation of anomalies is described in section 2.

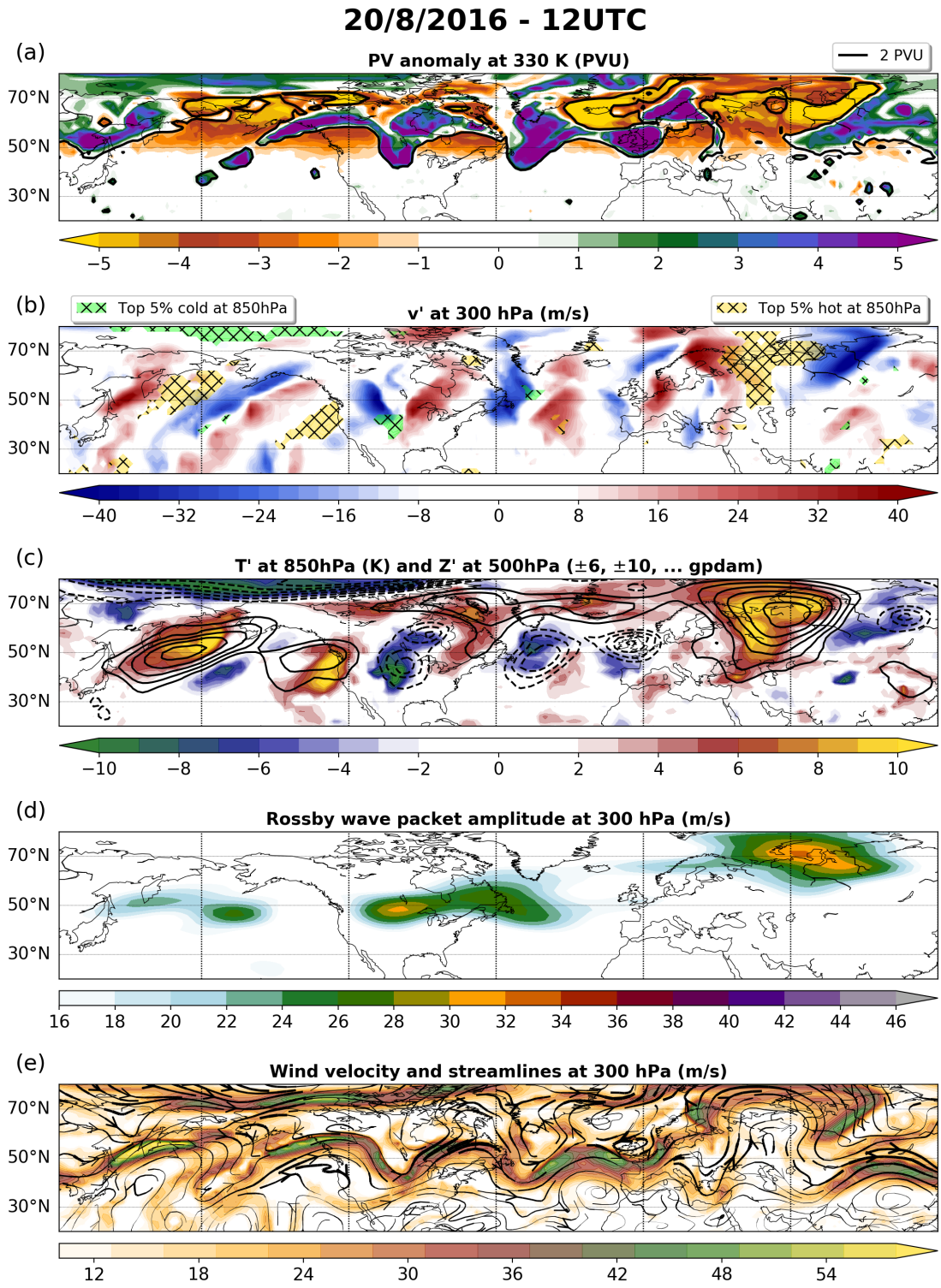

Fig. 1.3: *Upper-tropospheric circulation properties on 1200 UTC 20 August 2016. (a) PV anomaly (color shading; in PVU) and isoline of 2 PVU (black contour) at 330 K. (b) Color shading depicts meridional wind anomaly at 300 hPa (in ms^{-1}). Yellow (green) hatching represents areas where temperature anomaly at 850 hPa is greater (less) than the 95^{th} (5^{th}) percentile. (c) Color shading depicts temperature anomaly at 850 hPa (in K) and black contours represent geopotential height anomalies at 500 hPa. (d) RWP amplitude at 300 hPa (in ms^{-1}). (e) Wind velocity (color shading; in ms^{-1}) and wind streamlines at 300 hPa.*

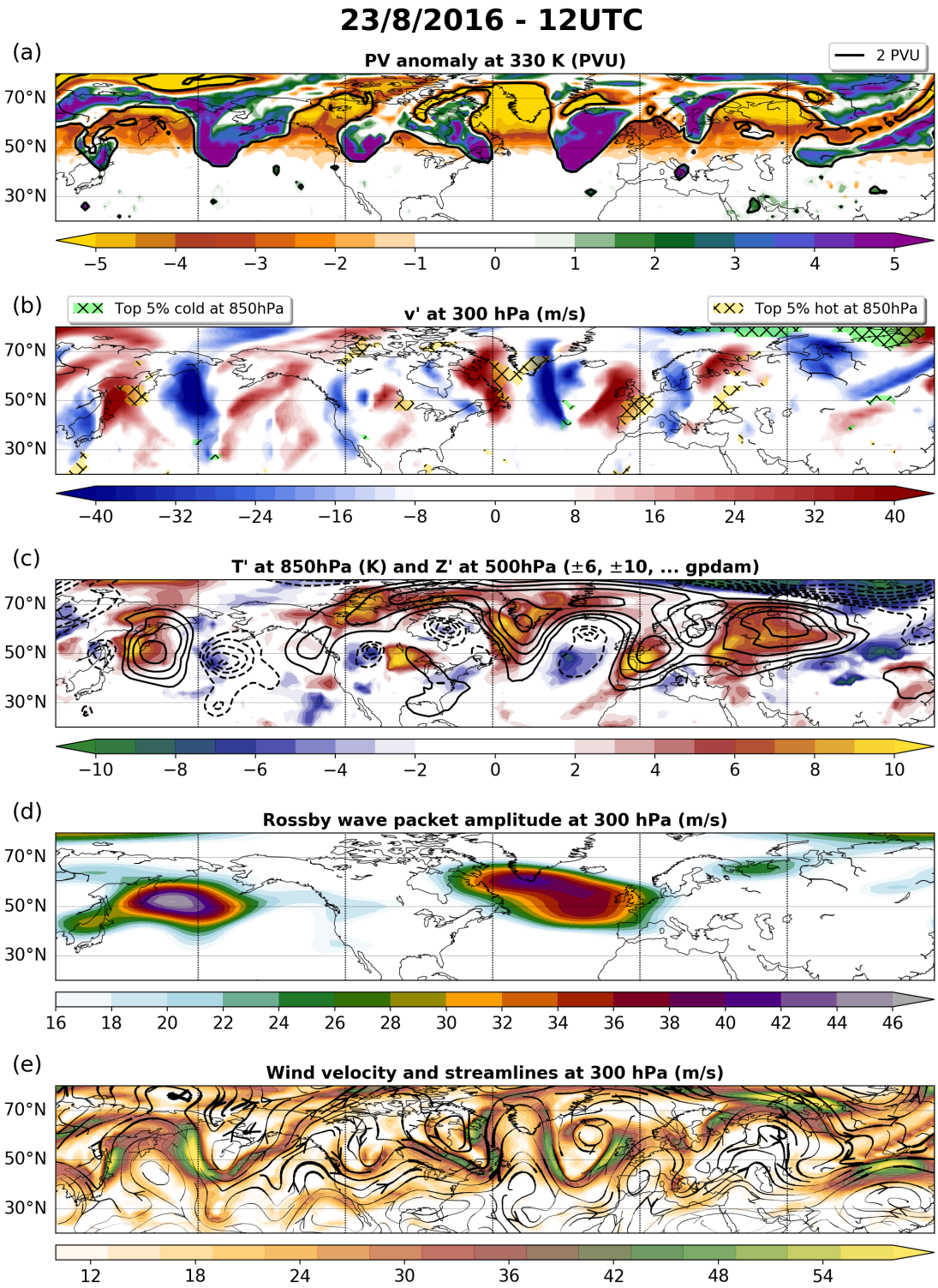

Fig. 1.4: *Same as Fig. 1.3, but for 1200 UTC 23 August 2016.*

ity, and group velocity. The schematic in Fig. 1.5 serves to illustrate these aspects in an idealized two-dimensional RWP case. The depicted succession of northerlies and southerlies propagate eastward at a similar rate (phase velocity), under the influence of a westerly background flow. The corresponding envelope function along a latitude circle (solid gray line) reflects the fact that the amplitude of the RWP reaches a maximum close to its centre with a gradual decay both westward and eastward. The rate at which the packet as a whole propagates (group velocity) can be inferred from the evolution of the envelope function, that in this case is also influenced by a newly developed small area of southerlies downstream. Finally, the distance between longitudes with the same phase corresponds to the local wavelength of the wave.

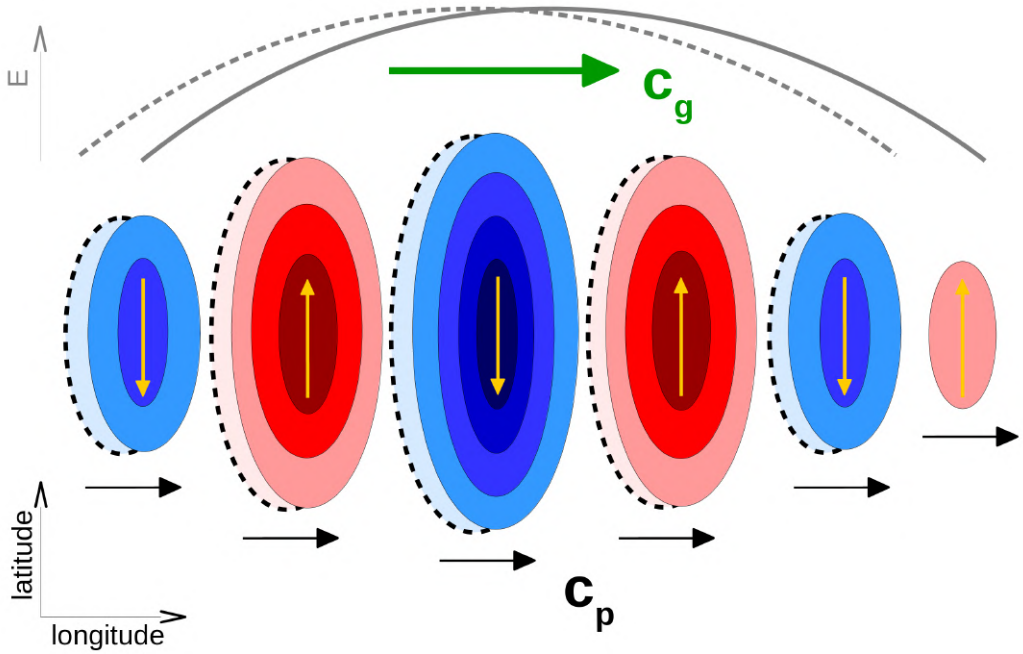

Fig. 1.5: *Schematic depiction of the main RWP properties. Shaded color represents meridional wind velocity in the latitude–longitude domain (yellow arrows show direction). The gray line indicates the corresponding envelope, E, along a latitude circle. The schematic involves two successive timesteps with the initial time step represented by the dashed contours. Phase velocity, c_p, and group velocity, c_g, are indicated by the black and green arrows respectively.*

One of the main goals of this study is to emphasize that these fields are important properties of RWPs that vary in space and time, thus necessitating the employment of local diagnostics in RWP investigations. Previous diagnostic methods in this regard have been non-local in space or time and are summarized in section 5.1.

1.3 Role of Rossby wave packets in temperature extremes

Better understanding the physical processes that lead to weather extremes is essential in investigating the predictability limits of these events (Rodwell *et al.* 2013), as well as formulating hypotheses on how their characteristics may vary with climate change (Shepherd 2014). As mentioned before, recent studies have emphasized the role RWPs play in various contexts relevant for both weather and climate (Martius *et al.* 2008; Wirth and Eichhorn 2014; Souders *et al.* 2014b; Quinting and Jones 2016; Wirth *et al.* 2018). Weather extremes in the midlatitudes are often linked to strong Rossby wave activity in the upper troposphere and the associated meridional displacements of the jet stream (Schubert *et al.* 2011; Lau and Nath 2014). Large-amplitude RWPs are important in this regard, because they embody the synoptic-scale systems (cyclones, blocks, etc.) that are associated with regional flow patterns and physical processes that favour the occurrence of temperature extremes (Kyselý 2008; Pfahl and Wernli 2012; Bieli *et al.* 2015b; Chang *et al.* 2016).

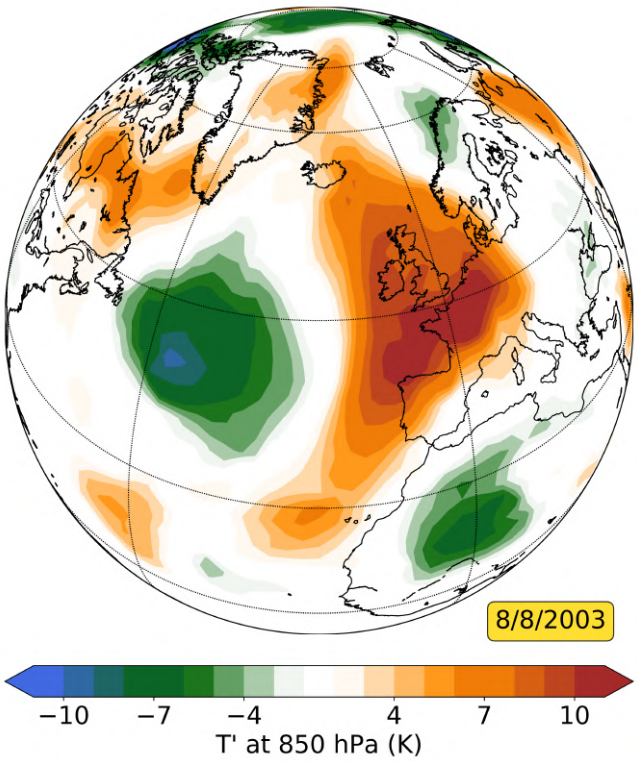

Fig. 1.6: *Daily mean temperature anomaly at 850hPa on 8 August 2003.*

Heat waves and temperature extremes in general pose a profound threat to natural ecosystems, human health, and the economy (e.g., Horton *et al.* 2016). Recent examples include the unprecedented and severe heat waves of 2003 and 2010 over Western Europe and Russia respectively (Fink *et al.* 2004; García-Herrera *et al.* 2010; Matsueda 2011). Due to the ongoing global warming, it is projected that events like these will occur on average every other summer by the end of the 21st century (Schär *et al.* 2004; Russo *et al.* 2014). Therefore, heat waves pose an increasingly serious threat

that the society needs to consider and tackle (Meehl and Tebaldi 2004; Rahmstorf and Coumou 2011; Stocker 2014) and the scientific community needs to better understand the relevant physical processes across scales. When possible, early warnings of their onset, intensity, and duration have to be issued.

Figure 1.6 shows an example from the 2003 heat wave in Western Europe, namely the daily mean temperature anomaly at 850 hPa on 8 August. It is evident, that a large area of cold anomaly occurs over the North Atlantic while an even more extended pattern of warm anomalies affects a large part of continental and maritime Europe. It is natural to assume that for events of this scale, a large-scale forcing must be to a certain extent responsible. In this regard, it is important to investigate whether aspects of heat waves such as magnitude and duration are associated with the spatiotemporal evolution of RWPs and their embedded troughs and ridges.

Figure 1.7 shows a Hovmöller diagram of the same event, which will be studied in more detail in section 3.4. This time–longitude diagram nicely illustrates the spatiotemporal evolution of the upper-tropospheric circulation, as it is reflected in the field of meridional wind at 300 hPa. In the right panel of the same figure shown is a time series of the normalized temperature anomaly at 850hPa averaged over the [38°N –58°N , 6°W –14°E] area. Evidently, the occurrence of the 2003 heat wave over Europe was associated with a slowly propagating RWP ($c_g \approx 15°$ longitude per day) that formed at around 110°W in early August and dissipated two weeks after at around 70°E . Similarly, Figure 1.8 shows a Hovmöller diagram and a time series of temperature anomaly at 850 hPa for the compound heat wave in Europe during August–September 2016 (Zschenderlein *et al.* 2018). A succession of three RWPs of pronounced amplitude, with short time intervals in between, was associated with three peaks of extremely warm temperatures (the first one was previously presented in Fig. 1.4).

Both heat waves were associated with a large-amplitude quasi-stationary ridge over Europe that was embedded in a larger-scale RWP. Such an environment favors the occurrence of temperature extremes in direct and indirect ways. Sustained southerlies advect the basic state isotherms and may bring hot air masses from the subtropics toward Europe. The increased geopotential height and high pressure over Europe are associated with clear skies (Fig. 1.9) and subsidence due to dynamical processes (see "omega" equation; e.g., Davies 2015a) or diabatic processes such as radiative cooling in the free atmosphere (Zschenderlein *et al.* 2019). This subsidence leads to adiabatic compressional warming and further suppression of clouds and precipitation. As a result, increased downward short-wave radiation and land–atmosphere feedbacks due to decreased evaporation of the drying soil lead to decreased latent cooling and thus a further intensification of the near-surface temperature. Details about the relative importance and interactions of these factors during heat waves are still under investigation and raise questions that are increasingly investigated in recent years (Fischer *et al.* 2007b; Bieli *et al.* 2015a; Quinting and Reeder 2017; Fragkoulidis *et al.* 2018; Zschenderlein *et al.* 2019).

Recent studies have connected the occurrence of major heat waves to large-amplitude circumglobal waves as quantified by Fourier amplitudes in the temporally averaged wind field (Petoukhov *et al.* 2013a; Kornhuber *et al.* 2017b). Central to these studies is the hypothesis that Rossby waves are trapped within circumglobal mid-latitude waveguides and a quasi-resonance with orographic forcing turns them

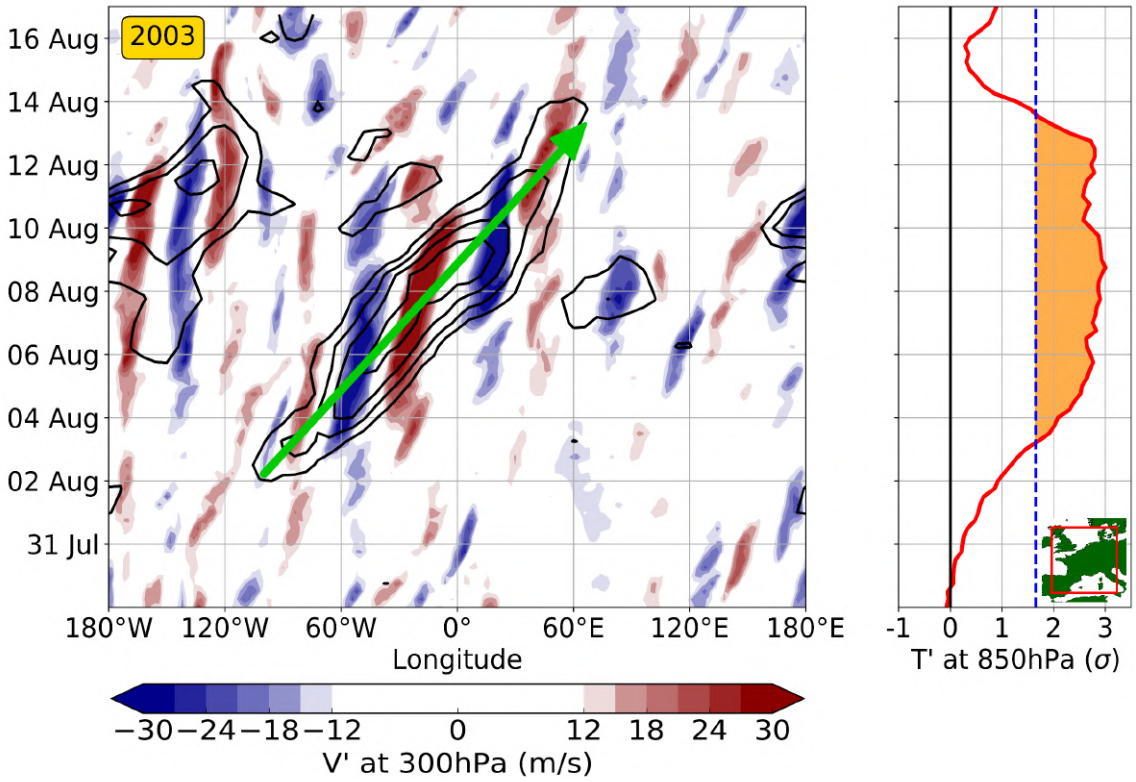

Fig. 1.7: *Left: Hovmöller diagram illustrating the upper tropospheric circulation during the 2003 heat wave (ERA-Interim data). The black contours depict RWP amplitude at 300hPa (every 4ms^{-1}from 22 to 38ms^{-1}). Color shading represents the meridional wind anomaly at 300 hPa; blue for southward anomaly and red for northward. The two fields are meridionally averaged over a 20° latitude band which self-adjusts (within the 30°N–70°N band) to those latitudes in which the highest RWP amplitudes occur. The time resolution is 6 hours. A weak bivariate interpolation using cubic Hermite splines is applied in view of smoother RWP contours. The slope of the drawn green dashed arrow indicates the group velocity of the eastward propagating RWP. Right: The red line depicts the time series of the normalized temperature anomaly at 850hPa for the same time period (given in standard deviations), averaged — with a weighting to the cosine of latitude — over the [38°N–58°N , 6°W–14°E] area (red rectangle in the lower right corner). Orange shading indicates that at the respective time the temperature anomaly exceeds the 95th percentile of JJA temperature anomalies in the period 1979–2016 (blue dashed line).*

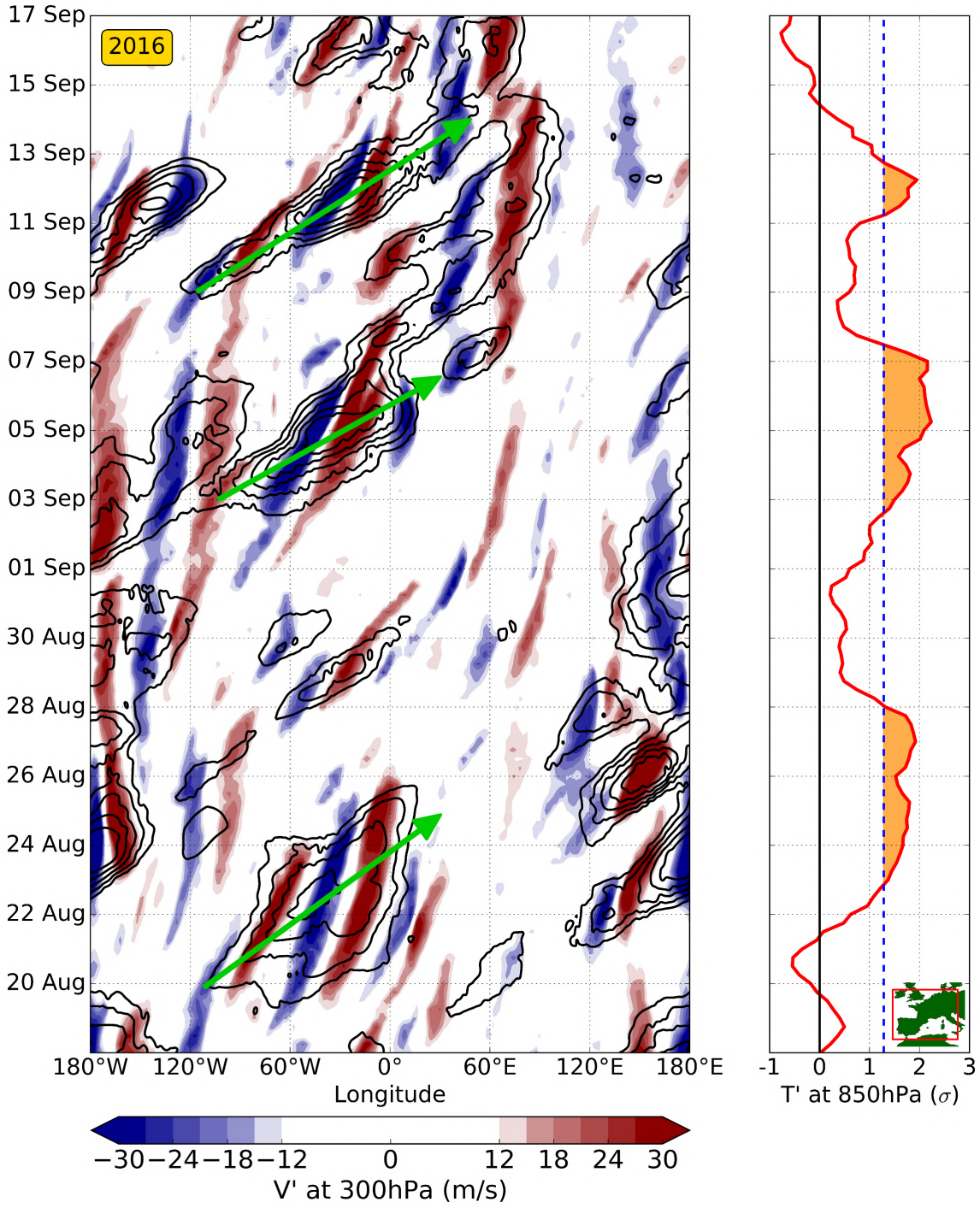

Fig. 1.8: *Same as Fig. 1.7 but for the 2016 compound heat wave in Western Europe. The normalized temperature anomaly at 850 hPa in the right panel is now averaged over the [35°N–55°N, 11°W–15°E] area (red rectangle in the lower right corner). Orange shading corresponds to temperature anomaly values in excess of the 90th percentile for the months of August and September (blue dashed line). Adapted from Zschenderlein* et al. *(2018).*

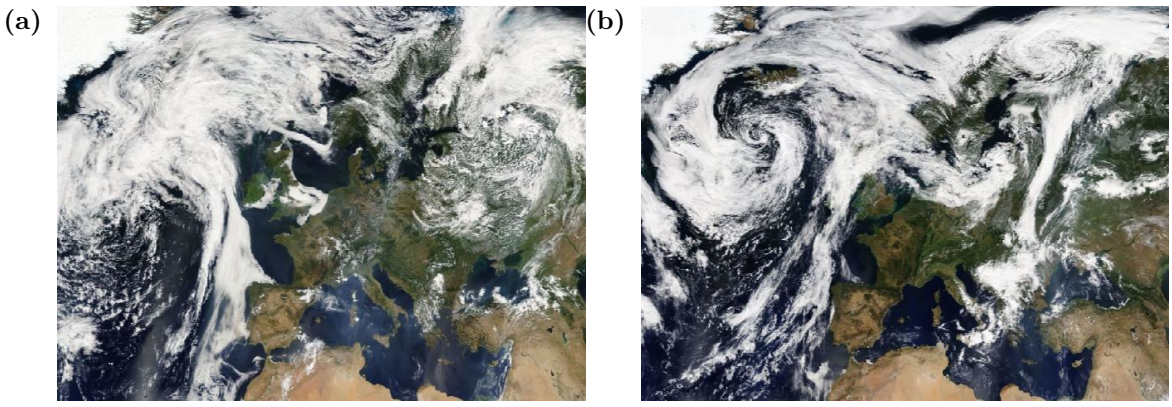

Fig. 1.9: *Satellite imagery of Europe from the Moderate Resolution Imaging Spectroradiometer (MODIS) instrument on board NASA's Terra satellite*[†] *on: (a) 8 August 2003 and (b) 23 August 2016.*

quasi-stationary, thus triggering extreme weather. In contrast, an immediate outcome from the brief investigation above is that waviness in the upper-tropospheric flow is often restricted to a non-circumglobal longitudinal range and the associated RWPs act as far-upstream precursors to temperature extremes. This motivates the hypothesis that the transient RWP properties provide a more direct link to lower-tropospheric temperature extremes. Most importantly, if a RWP of enhanced amplitude is associated with embedded troughs and ridges that have a small phase velocity, an extended episode of unusually warm or cold weather is likely to occur.

1.4 Objectives and outline of this work

The overarching goal of this work is to investigate the role of RWPs in temperature extremes. The main objectives to this end are the following:

- Develop diagnostics of RWP properties (amplitude, wavenumber, phase velocity, group velocity) locally in space and time. Produce global climatologies of their typical values and explore their seasonal variability.
- Conduct regression analyses in reanalysis data of the past decades in order to investigate the role of RWP amplitude and phase velocity in the occurrence and duration of temperature extremes. Compare results to similar analyses using a circumglobal waviness metric that is based on the Fourier spectrum of meridional wind.
- Construct composite maps and Hovmöller diagrams that will reveal the characteristic synoptic circulation patterns associated with temperature extremes in Europe

[†]The images are retrieved from the NASA Worldview Snapshots application (https://wvs.earthdata.nasa.gov/), part of the Earth Observing System Data and Information System (EOSDIS).

- Investigate the influence of the upper-tropospheric Rossby wave circulation in the past heat waves of 2003 and 2010 in Western Europe and Russia respectively.
- Report on medium-range forecast biases of RWP properties that may affect the predictability of temperature extremes.

In light of the aforementioned research questions and objectives, this study is organized as follows. Chapter 2 gives an overview of the data and some methods that are used extensively in this work. The specific methodologies used in each of the investigations, however, are presented in the introductory sections of the respective chapters. Chapter 3 includes a statistical analysis on the linkage between RWP amplitude and Northern Hemisphere temperature extremes, a comparison to Fourier analysis as well as case studies of the 2003 and 2010 heat waves. Composites of the synoptic circulation patterns leading to short-lived and persistent temperature extremes in Southeastern Europe are shown in chapter 4. Their representation in deterministic medium-range forecasts is also explored. In chapter 5, novel diagnostic methods of RWP phase and group velocity are presented, together with an evaluation of the seasonal variability in RWP properties. In the same chapter, the effect of RWP amplitude and phase velocity in the occurrence and duration of Central European temperature extremes will be quantified. Medium-range forecast biases of RWP properties are reported in chapter 6. Finally, chapter 7 provides a summary of the key results and an outlook.

Chapter 2

Data and methods

2.1 Overview

Several datasets from the European Centre for Medium-Range Weather Forecasts (ECMWF) have been used over the course of this dissertation. At first, ERA-Interim (Dee *et al.* 2011) and ERA5 [Copernicus Climate Change Service (C3S) 2017] reanalysis data spanning most to all years from 1979 to 2018 have been used. These fields include zonal and meridional wind at 300 hPa, geopotential at 300 hPa and 500 hPa, and temperature at 850 hPa and 2 metres. These were retrieved at a 6-hourly temporal resolution (daily at 0000, 0600, 1200 and 1800 UTC) on a grid of $2^\circ \times 2^\circ$ horizontal resolution. In addition, for the analyses in chapters 4 and 6 I use ERA-Interim and operational deterministic forecasts of meridional wind at 300 hPa and temperature at 850 hPa. These fields are retrieved at the same or lower temporal resolution and the same horizontal resolution as the reanalysis. Finally, in chapter 5 I use output from a barotropic model simulation of (Ghinassi *et al.* 2018). More details on the above are given in the methodology sections of the respective chapters.

Investigating the properties of RWPs and their role in temperature extremes involved some processing of the retrieved data. A description of the annual cycle computation and the 6-hourly anomalies of the aforementioned fields is described in the next section. In addition, section 2.3 provides insight in the spatial filtering of the meridional wind field, which appropriately smooths the data and restricts our attention to the relevant scales of the RWP evolution. A large portion of the efforts behind the analyses in chapters 3–6 was focused at developing or refining diagnostic methods relevant to the evolution of RWPs as well as data analysis techniques for the investigation of their relevance to temperature extremes. Most importantly, sections 3.2, 4.2, and 5.3 describe in detail the diagnosis of RWP amplitude, wavenumber, phase velocity, and group velocity locally in space and time.

2.2 Anomaly fields computation

This section describes how the anomaly fields are computed for the analyses in chapters 3–6. Given the 24-hourly time series of a variable at a given grid point and time of the day (i.e., 0000, 0600, 1200, 1800 UTC) the goal is to compute the anomaly of each

time step from the multi-year climatology. Figure 2.1 serves to illustrate the procedure for 0000 UTC T at 850 hPa at 50°N , 10°E as an example. The first step is to compute the annual cycle as the mean of every day in the year (blue line in Fig. 2.1), which is evidently a noisy function due to the shortage of years in the reanalysis data. The annual cycle is smoothed by decomposing it to a Fourier series and restricting it to the first 4 harmonics (red line). The procedure is repeated separately for the other 3 times of the day (0600, 1200, 1800 UTC) in order to preserve information of the diurnal cycle (which for the case of lower-tropospheric temperature may be significant). Finally, to get the T anomaly, from each step in the complete 6-hourly time series the value of the respective step in the smooth annual cycle is subtracted.

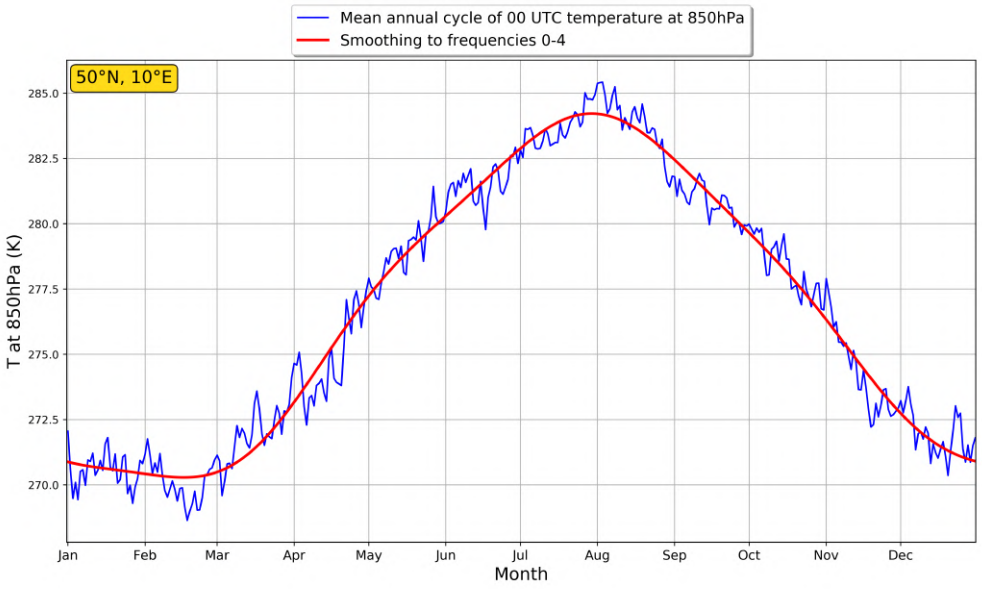

Fig. 2.1: *Mean annual cycle calculation and smoothing.*

2.3 Spatial filtering in the meridional wind field

The meridional wind field is first zonally filtered in order to focus attention to the scales of interest. Namely, I restrict each meridional wind latitude circle to the 2000–10000 km wavelengths (Fig. 2.2). Filtering in wavelength rather than wavenumber, ensures that structures of a given size range will be considered regardless of the latitude they are found. This is done by weighting the respective Fourier wavenumbers with an adjustable Tukey window*. The Tukey window is designed in a way, such that a smooth transition between latitudes is achieved. Depending on the latitude, it spans the spectral range from [low wavenumber limit – 1.5] to [high wavenumber limit + 1.5] and has smooth tails. The Tukey window at 50°N and its filtering effect on an exemplary meridional wind latitude circle is shown in Figure 2.3. As desired for the mid-latitudes, this filtering discards the very high frequencies that account for features in the flow that

*The Tukey window is a cosine lobe convolved with a rectangular window (Harris 1978).

cannot be attributed to the large-scale Rossby wave motion. In addition, planetary waves of wavenumber 1 are discarded and the contribution of wavenumber 2 is weighted by a factor of ∼0.4.

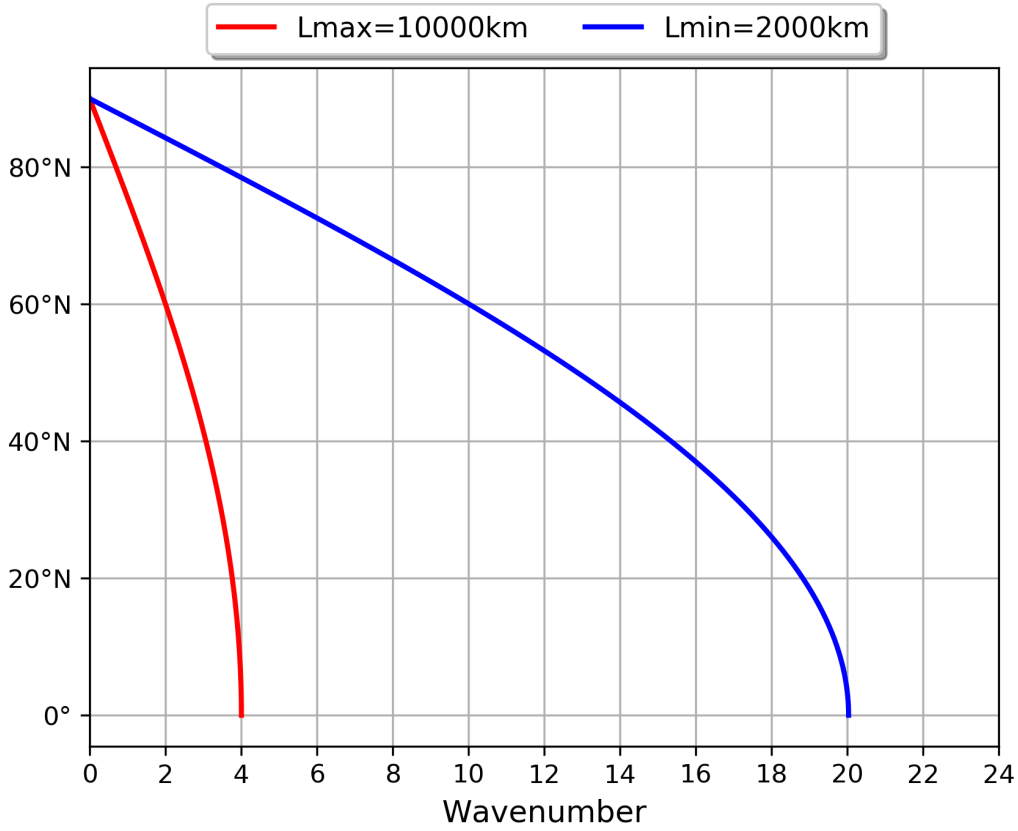

Fig. 2.2: *Wavelength limits in the zonal filtering of meridional wind at 300 hPa. The blue and red lines show for each latitude the wavenumber limits that correspond to wavelengths of 2000 km and 10000 km respectively.*

Figure 2.4 shows the effect of zonal filtering at all latitudes of the 1200 UTC 24 August 2016 meridional wind field. The yellow contour represents the 20ms^{-1}isoline of the corresponding envelope field (computed as described in section 5.3). Panel (c) in the same figure depicts the effect of an additional step that involves a meridional convolution with a Hann window of 7° width at half maximum (Harris 1978). This last step acts to minimize possible discontinuities in the meridional direction, caused by the zonal filtering. The resulting meridional wind and envelope fields are thus effectively smoothed without obscuring the main characteristics of the waves.

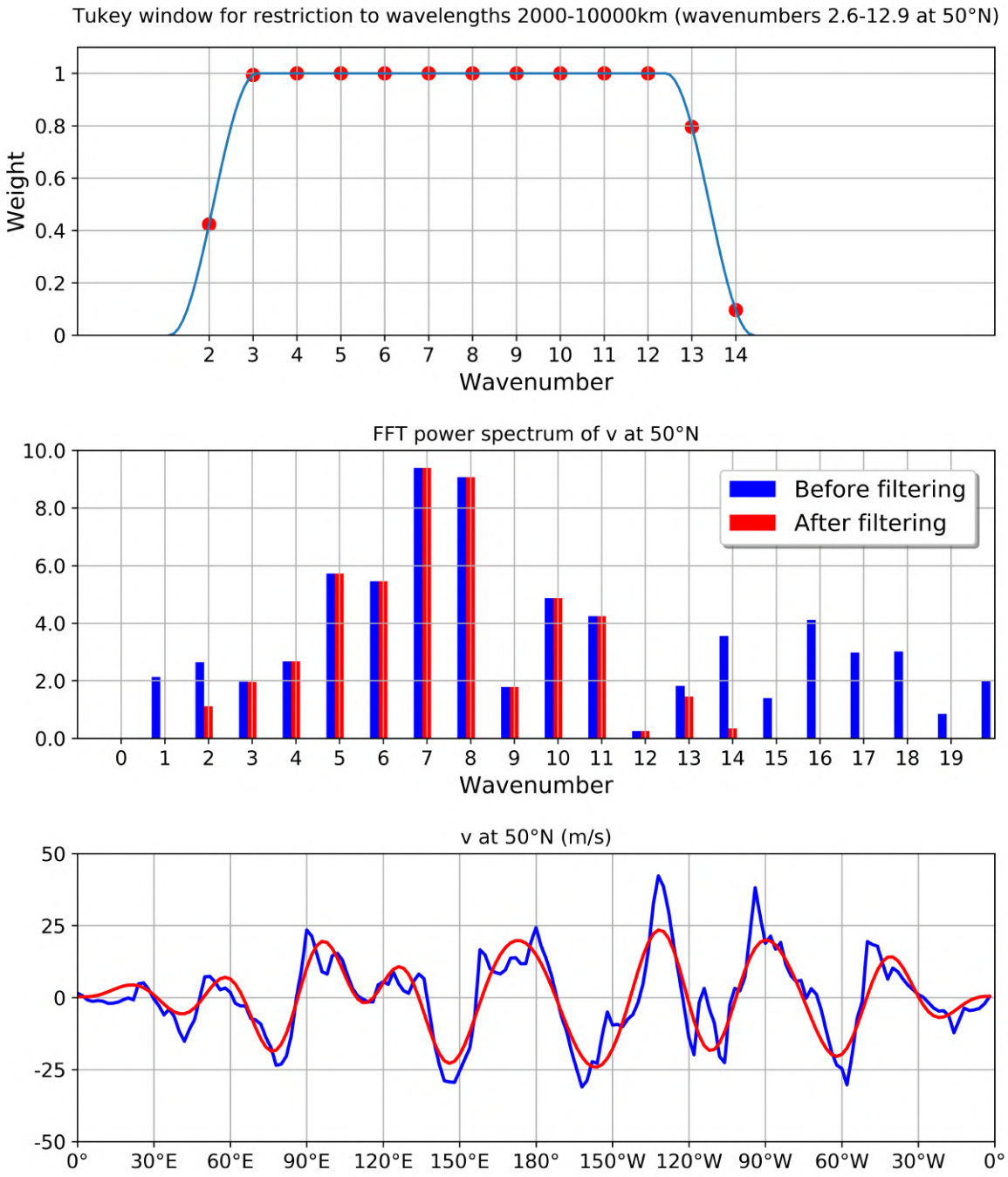

Fig. 2.3: *Example of zonal wavelength restriction to 2000–10000 km. The upper panel shows a Tukey window of α=0.3 (70% of the window has a weight of 1 and 30% is cosine-tapered) in the wavenumber domain. At 50°N, the 2000–10000 km restriction corresponds to wavenumbers of approximately 2.6–12.9. As per our methodology, the Tukey window limits are placed at wavenumbers 1.1 and 14.4 and wavenumbers that are close to the tails will have a lower contribution. For example, the power at wavenumber 14 is multiplied by a factor of 0.1 and the power at wavenumber 13 by a factor of 0.8. The middle panel shows the effect of the Tukey window in the Fourier spectrum of an exemplary meridional wind latitude circle. The lower panel shows the smoothing effect in the signal itself.*

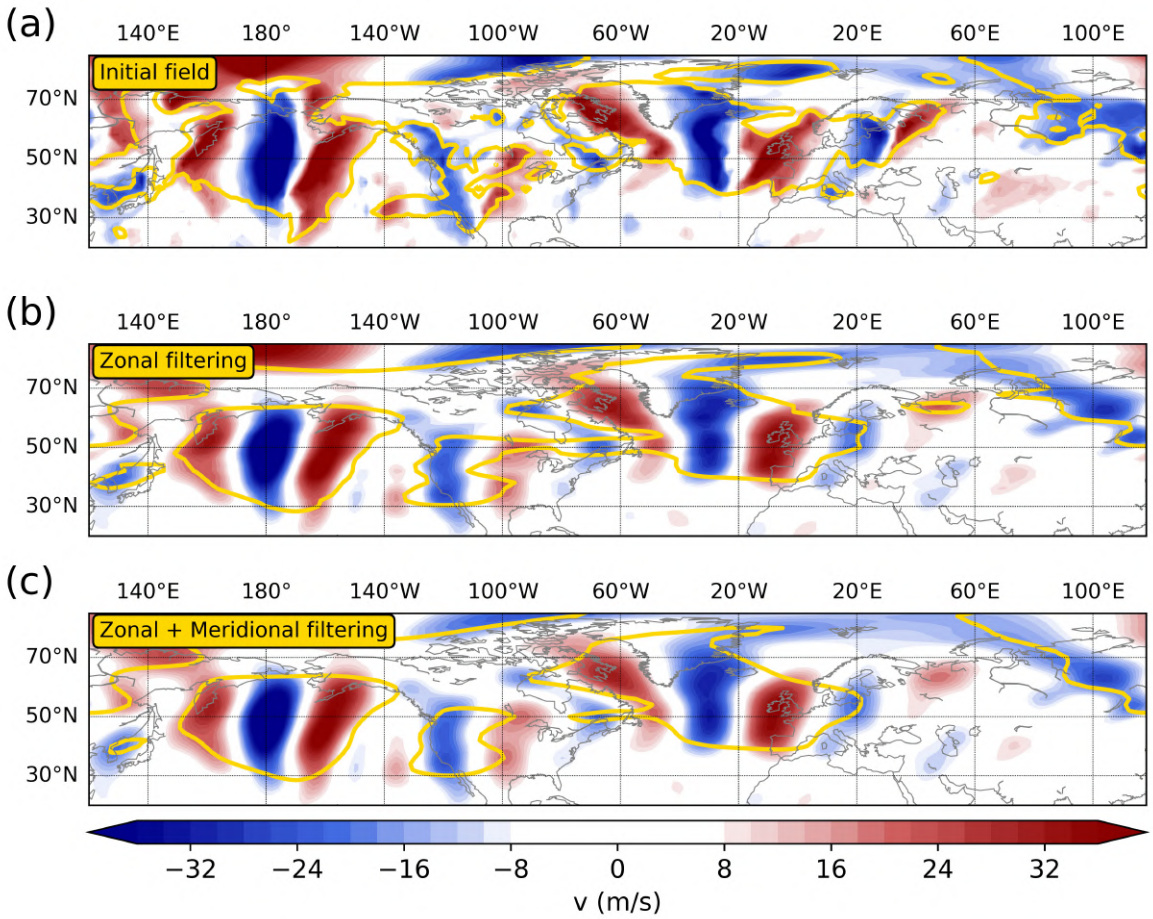

Fig. 2.4: *Spatial filtering example on 1200 UTC 24 August 2016. a) Original meridional wind field, b) zonal restriction to 2000–10000 km, c) zonal restriction to 2000–10000 km followed by meridional convolution with a Hann window of 7° width at half maximum. In all panels the yellow contour corresponds to* $E{=}20 ms^{-1}$.

Chapter 3

Linking Northern Hemisphere temperature extremes to Rossby wave packets

G. Fragkoulidis[a*], V. Wirth[a], P. Bossmann[b] and A. H. Fink[b]

[a] *Institute for Atmospheric Physics, Johannes Gutenberg University, Mainz, Germany*
[b] *Institute of Meteorology and Climate Research, Karlsruhe Institute of Technology, Karlsruhe, Germany*
[*] *corresponding author e-mail: gfragkou@uni-mainz.de*

This chapter is equivalent to the peer-reviewed article of homonymous title by the authors listed above that was published in the January 2018 issue of the Quarterly Journal of the Royal Meteorological Society (Fragkoulidis et al. *2018)* [†]*. The manuscript is integrated as is into the dissertation and the section and figure numbers are adjusted accordingly. The references are listed in the unified bibliography at the end of the dissertation.*

Abstract

The present work investigates the statistical linkage between upper-tropospheric transient Rossby wave packets (RWPs) and lower-tropospheric temperature extremes on the Northern Hemisphere during the period 1979–2015. Data from ERA-Interim reanalyses are used for the diagnosis of RWP amplitude and temperature anomalies as well as the systematic examination of their connection. Areas of large RWP amplitude are found to be associated with an increased probability of lower-tropospheric temperature extremes in many regions of the mid-latitudes. Although a seasonal and inter-regional

variability is apparent, this link is always stronger compared to an analysis using a circumglobal waviness metric based on Fourier wavenumber amplitudes.

Further insight is gained by complementing the climatological results with an investigation of the two most severe heat waves in the recent history of Europe, viz. during the 2003 and 2010 summers. Both events are found to be associated with conspicuous non-circumglobal RWPs, but differences between the two events suggest that the mechanisms linking RWPs and temperature extremes are case dependent. The aforementioned results underscore the important role of upper-troposphere dynamics and unveil avenues for future research on heat waves and cold spells at both weather and climate time scales.

3.1 Introduction

Episodes with extreme temperatures near the Earth's surface have profound impacts on natural ecosystems, human health, and the economy (e.g. Horton *et al.* 2016). Recent examples include the 2003 heat wave over Europe (Fink *et al.* 2004; García-Herrera *et al.* 2010), the 2010 heat wave over Russia (Matsueda 2011), or the cold winter over eastern North America in 2014 (Davies 2015b). Owing to global warming, heat waves are expected to become a more serious problem in future decades (Meehl and Tebaldi 2004; Rahmstorf and Coumou 2011; Stocker 2014). For instance, an event like the 2003 European heat wave, which at that time was unprecedented in recorded history, is likely to occur every other summer by the end of the 21st century (Schär *et al.* 2004; Russo *et al.* 2014).

Mid-latitude temperature extremes near the surface are often associated with strong Rossby wave activity in the upper troposphere (Schubert *et al.* 2011; Lau and Nath 2014). In particular, perturbations in the meridional flow component associated with Rossby wave activity lead to the advection of the basic-state isotherms and the consequent formation of troughs and ridges (Lackmann 2011). This large-scale setting is conducive to physical processes that may lead to the formation of air masses with extreme temperatures (Bieli *et al.* 2015b). If, in addition, the individual troughs and ridges within the wave pattern move with a small phase velocity or are quasi-stationary, they constitute a large-scale setting where an extended episode of unusually warm or cold weather is likely to occur (Kyselý 2008).

Investigating the linkage between near-surface temperature extremes and upper-tropospheric "waviness" is essential for at least two reasons. Firstly, from a climate perspective, changes of temperature variability at regional scale are, to a certain extent, controlled by large-scale dynamical processes (Garfinkel and Harnik 2017), therefore uncertainties in the future evolution of the dynamic aspects of atmospheric circulation limit the robustness of regional climate projections (Shepherd 2014). The rapid warming near the surface in the Arctic (Arctic amplification), the enhanced warming in the tropical upper troposphere, and the cooling in the polar stratosphere are all likely to affect the variability of the mid-latitude flow, but the resulting impact on weather extremes is not entirely clear yet (Butler *et al.* 2010; Sun *et al.* 2013; Harvey *et al.* 2014; Barnes and Screen 2015; Schneider *et al.* 2015; Hoskins and Woollings 2015). Secondly, from a weather forecast perspective, it has been argued that the occurrence of

long-lived Rossby wave packets (RWPs) can lead to enhanced predictability in certain situations (Lee and Held 1993; Grazzini and Vitart 2015). Associated with that, it has long been known that smaller scale weather features may inherit predictability from larger scale dynamical features (Anthes *et al.* 1985). Therefore, it is highly desirable to have a sound understanding of the linkage strength between upper-tropospheric waviness and lower-tropospheric temperature extremes, along with its inter-regional and seasonal variability.

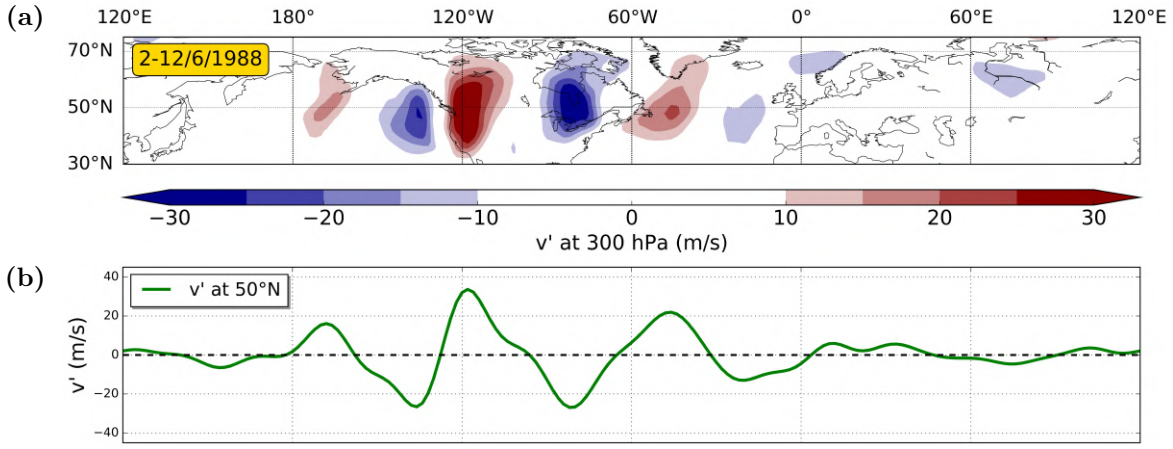

Fig. 3.1: *(a) Map of the 10-day mean (2–12 June 1988) meridional wind anomaly v' (colour, in ms^{-1}) at 300 hPa; (b) meridional wind anomaly v' at 50°N (green line, in ms^{-1}).*

The present paper aims to further our understanding of these aspects. Since upper-tropospheric Rossby waves tend to organize in spatially confined and possibly coherent wave packets (Chang 1993), we propose a novel perspective that focuses on RWPs rather than circumglobal Rossby waves (e.g. Screen and Simmonds 2014). A RWP is said to exist whenever the amplitude of a Rossby wave varies with longitude such that it reaches a maximum over a certain longitude with a gradual decay both westward and eastward (Chang 2001b). Such structures are found in both observations and in a hierarchy of models (Lee and Held 1993). Coherent RWPs propagate eastward with the so-called group velocity, while the embedded eddies propagate with their individual phase velocities, which are typically smaller than the group velocity (Chang 1993; Esler and Haynes 1999a). In recent studies, it is increasingly recognized that RWPs play an important role in various contexts relevant for both weather and climate (Martius *et al.* 2008; Wirth and Eichhorn 2014; Souders *et al.* 2014b; Quinting and Jones 2016; Teubler and Riemer 2016).

Figure 3.1 gives an example from June 1988, when the western part of the Northern Hemisphere was characterized by a large-amplitude RWP, while the flow was close to zonal in the eastern part of the Northern Hemisphere. This RWP was associated with a pronounced heat wave over the Midwest of the U.S.A. (Lyon and Dole 1995; Schubert *et al.* 2011), which was mediated by a quasi-stationary ridge over that region. It is well known that persistent ridging over a region during summer facilitates the formation of a heat wave, and Figure 3.1 shows that even in a 10-day running mean (that tends to produce smooth hemispheric-wide wave patterns) this does not require

the Rossby wave to be of circumglobal nature by necessity (see also Röthlisberger *et al.* 2016). Nevertheless, this is worth pointing out and investigating further, in view of recent studies connecting the occurrence of some major heat waves to large-amplitude circumglobal waves as quantified by Fourier wavenumber amplitudes (Petoukhov *et al.* 2013a; Kornhuber *et al.* 2017c).

In this paper we suggest that the local amplitude of propagating RWPs is a more appropriate metric of the upper-tropospheric waviness in the present context than the Fourier amplitudes of circumglobal waves. We will quantify the statistical connection between RWP amplitudes and lower-tropospheric temperature extremes and show that, indeed, this is an improvement over the use of Fourier amplitudes. In addition, we will compute the spatial distribution of this statistical linkage over the entire Northern Hemisphere for both the summer and winter seasons. Finally, we complement our statistical analysis with case studies of two prominent recent heat waves (2003 in western Europe and 2010 in Russia) in terms of their associated RWP signatures. These studies will seek an illustration of the case-to-case variability (within the sample used in our statistical analysis) in aspects of the temperature extremes and the corresponding role of RWPs.

The article is organized as follows. First, the data used, the calculation of anomaly fields, the diagnosis of RWPs, and a heat wave index are introduced in section 3.2. Thereafter, results regarding the statistical linkage between upper-tropospheric waviness (RWP amplitude) and lower-tropospheric temperature extremes are presented in section 3.3. This analysis is complemented in section 3.4 with an investigation of the RWPs role during the 2003 and 2010 heat waves. Finally, a summary of our main results and some discussion are provided in section 3.5.

3.2 Data and methods

3.2.1 Reanalysis data

Our investigation is based on data from the ERA-Interim reanalysis project (Dee *et al.* 2011) of the European Centre for Medium-Range Weather Forecasts (ECMWF). We used the meridional wind v at 300 hPa, geopotential, Φ, at 300 hPa, and temperature, T, at both 850 hPa and 2 metres. Note that the 2-metre temperature field analysis in ECMWF is performed using a relatively simple data interpolation scheme following the upper-air atmospheric 4-dimensional variational analysis. We retrieved the data on a $2^\circ \times 2^\circ$ horizontal resolution with a temporal resolution of 6 hours (daily at 0000, 0600, 1200 and 1800 UTC), spanning the period from January 1979 to December 2015. Unless stated otherwise, daily means obtained by averaging the four values corresponding to the respective day are used. In cases where an averaging over a limited region was applied, the mean over the respective grid points was computed with a weighting to the cosine of latitude, in order to be consistent with a true area average.

3.2.2 Computation of anomalies

In this paper we are primarily concerned with synoptic-scale transient features. Therefore, we defined 6-hourly anomalies (denoted by a prime) as deviations from climatology

as follows:

$$\psi'(\lambda, \phi, t) = \psi(\lambda, \phi, t) - \overline{\psi}(\lambda, \phi, t_d) - \psi_l(\lambda, \phi, t) \; . \tag{3.1}$$

Here, ψ represents any of the variables v, Φ, or T, λ denotes longitude, ϕ denotes latitude, t denotes time, and t_d denotes a particular timestep within the climatological year (e.g. 1800 UTC February 5). In the above equation, $\overline{\psi}(\lambda, \phi, t_d)$ represents the climatology at t_d; it was obtained by first averaging the 37 values of the variable for each t_d over the 37 years available (1979–2015). By design, the resulting function is periodic in time (with a period of one year), but it shows strong noise owing to the relatively small number of years to be averaged over. We, therefore, performed a Fourier series expansion and discarded the higher harmonics keeping only the lowest four frequencies 1–4 year^{-1}. In addition, we detrended the anomalies by subtracting the 1979–2015 linear regression $\psi_l(\lambda, \phi, t)$ of the variable at each grid point.

3.2.3 Diagnosing Rossby wave packets

The diagnosis of upper-tropospheric RWPs was performed using the meridional wind anomaly $v'(\lambda, \phi, t)$ at 300 hPa (Figure 3.2a). In particular, we computed the envelope $E(\lambda, \phi, t)$ of $v'(\lambda, \phi, t)$ following the ideas of Zimin *et al.* (2003). The envelope field is non-negative everywhere and can be taken as a measure of RWP amplitude. By design, it eliminates the phase of the carrier wave (i.e. the location of troughs and ridges) and, thus, allows one to focus on the RWP as a whole. We modified the algorithm of Zimin *et al.* (2003) by implementing a number of refinements. For instance, we filtered the fields by multiplying the Fourier coefficients with an adjustable Tukey window (cosine lobe convolved with a rectangle window, Harris 1978) instead of a boxcar window; this allows us to achieve a smoother transition between latitudes. In addition, following the approach of Wolf and Wirth (2015), we computed the envelope in semigeostrophic coordinate space. This is motivated by the desire to reduce spurious fragmentation of RWPs, which arises from the semi-geostrophic nature of Rossby waves in combination with the method of Zimin *et al.* (2003). In summary, we performed the following steps:

(i) For each latitude, we filtered the fields of v' and Φ' in the zonal direction, keeping wavelengths roughly between λ_1 =2000 km and λ_2 =10000 km. This is done by multiplying the Fourier coefficients with a Tukey window. First we calculated the (non-integer) zonal wavenumber limits s_1 and s_2 corresponding to λ_1 and λ_2, respectively. The non-zero part of the Tukey window then spans the total zonal wavenumber range $[s_2 - 1.5, s_1 + 1.5]$, with its cosine-tapered parts accounting for 30% of the total window range.

(ii) We applied a semi-geostrophic coordinate transformation as described in Wolf and Wirth (2015) using the filtered Φ'.

(iii) The transformed v' field in the new coordinate system was linearly interpolated back to a regular (latitude-longitude) grid and was filtered again, as in step (i).

(iv) Lastly, the envelope E was computed from v' separately for each latitude with the so-called Hilbert transform method (Zimin *et al.* 2003) without applying any additional filter (Figure 3.2b).

Repeating these steps for every latitude resulted in the two-dimensional $E(\lambda, \phi, t)$ field (Figure 3.2c).

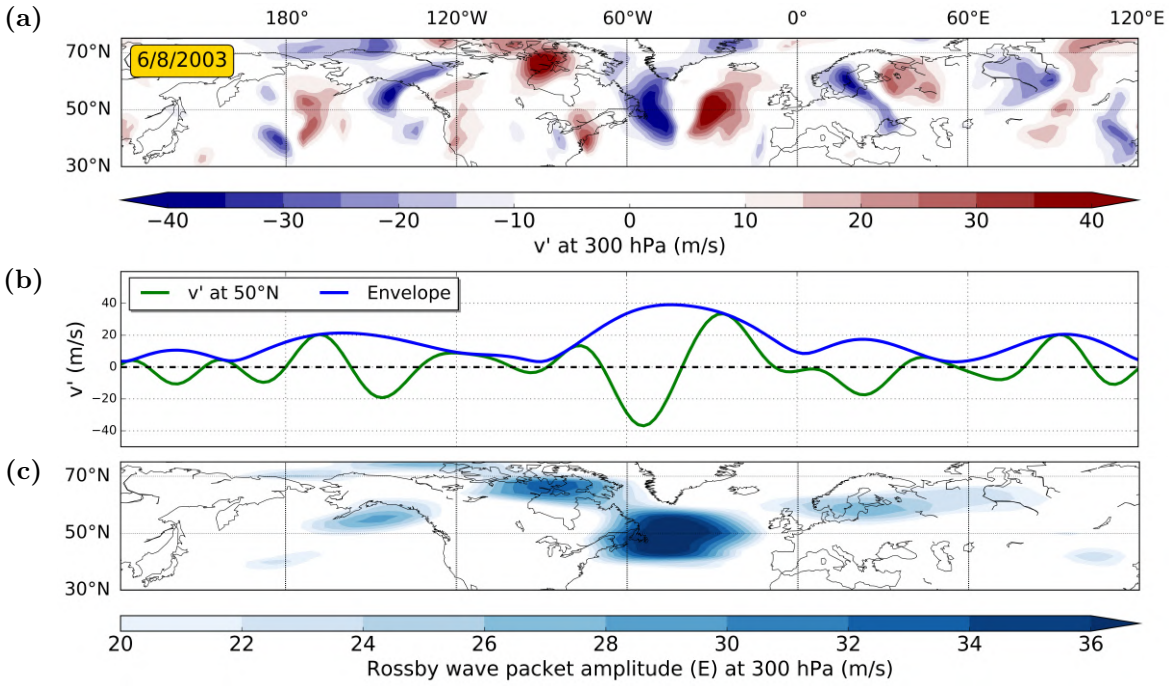

Fig. 3.2: *RWP diagnosis example for 6 August 2003 0000 UTC. (a) Map of the meridional wind anomaly v' (colour, in ms^{-1}) at 300 hPa; (b) meridional wind anomaly v' at 50°N (green line, in ms^{-1}) and its envelope E (blue line, in ms^{-1}); (c) map of the envelope field E (RWP amplitude, ms^{-1}).*

3.2.4 Heat wave index

We used a modified version of the heat wave magnitude index daily (HWMId) by Russo *et al.* (2015) to detect regions that are affected by abnormally high surface temperatures. This index measures the extremeness of the daily maximum 2-metre temperature T_{dm} at each grid point compared to climatology. In this study, the climatology was obtained from the ERA-Interim data. The HWMId was computed as the sum of the "daily magnitude" M_d of all days from the considered heat wave episode; the daily magnitude M_d, in turn, was defined as

$$M_d(T_{dm}) = \begin{cases} \frac{T_{dm} - T_{25\mathrm{p}}}{T_{75\mathrm{p}} - T_{25\mathrm{p}}} & \text{if } T_{dm} > T_{25\mathrm{p}} \ , \\ 0 & \text{if } T_{dm} \leq T_{25\mathrm{p}} \ , \end{cases} \tag{3.2}$$

where $T_{25\mathrm{p}}$ and $T_{75\mathrm{p}}$ denote the 25^{th} and the 75^{th} percentile of the climatological distribution of T_{dm}, respectively, and $T_{75\mathrm{p}} - T_{25\mathrm{p}}$ is the corresponding interquartile range. Owing to its reference to local climatology, the HWMId allows one to compare heat wave periods in different climatic regions in a meaningful way. In contrast to Russo *et al.* (2015), here the climatological distribution of T_{dm} was estimated from the reference period 1979–2015 using the $31 \times 37 = 1147$ values of T_{dm} which correspond to the

31-day window centered on the respective day of each year (thus achieving a smooth day-to-day variation of $T_{25\mathrm{p}}$ and $T_{75\mathrm{p}}$). This way, it takes into account the annual cycle in 2-metre temperature and the heat wave identification is not biased toward summer, allowing one to study anomalously hot events year-round. In summary, the HWMId combines a measure of the deviation from climatology with a measure of the length of the episode.

3.3 Connection between upper-tropospheric waviness and lower-tropospheric temperature anomalies

3.3.1 Analysis for a European region in summer

The connection between RWP amplitudes at 300 hPa and temperature anomalies at 850 hPa, is first exemplarily quantified for the Northern Hemisphere summer (June, July, and August — JJA) in a region of Europe. In the following subsection it will be extended to the entire Northern Hemisphere extratropics for both the summer and winter seasons. All results presented in this and the following section are reasonably robust in the sense that small changes in user-defined parameters do not lead to qualitative changes in the results. Details about related sensitivity tests can be found in Appendix A.

A temperature is considered to be anomalous to the extent that its daily anomaly T' deviates from climatology in either direction (warm or cold). In other words, we consider daily mean $|T'|$ at 850 hPa as our metric for anomalous temperature. The daily mean RWP amplitude at 300 hPa is quantified through the daily mean envelope E, as described in section 3.2. We focus our attention on synoptic-scale temperature extremes, therefore both $|T'|$ and E are averaged over an area covering parts of South and Central Europe, viz. 36–56°N and 0–20°E . We draw on the data from all available summers (1979 to 2015), but we use only every third day in a consecutive sequence of summer days in order to minimize the impact of serial correlation on the results, without strongly decreasing our sample size.

Figure 3.3a shows the result in form of a scatter plot. The two time series have been normalized by subtracting their means and dividing by their standard deviations. This facilitates the comparison with the Fourier amplitude analysis discussed below. Evidently, there is an increase of $|T'|$ with RWP amplitude and the Spearman's rank correlation coefficient of $\rho = 0.44$ suggests a not too strong yet significant (p-value well below 1‰) connection between the two fields. The data points are then divided into 10 equally populated bins, indicated by the dashed vertical lines, which will be referred to as E-bins hereinafter. The 90^{th} percentile of the $|T'|$ distribution is indicated by the horizontal blue line. In the following, we are going to refer to a temperature anomaly as "extreme" if it exceeds the 90^{th} percentile, i.e. if the data point on the scatter diagram lies above the blue line.

Focusing on the temperature extremes, Figure 3.3a shows that the fraction of points above the blue line is significantly larger for the rightmost E-bin in comparison with the lower-lying E-bins. This means that the probability for a temperature extreme

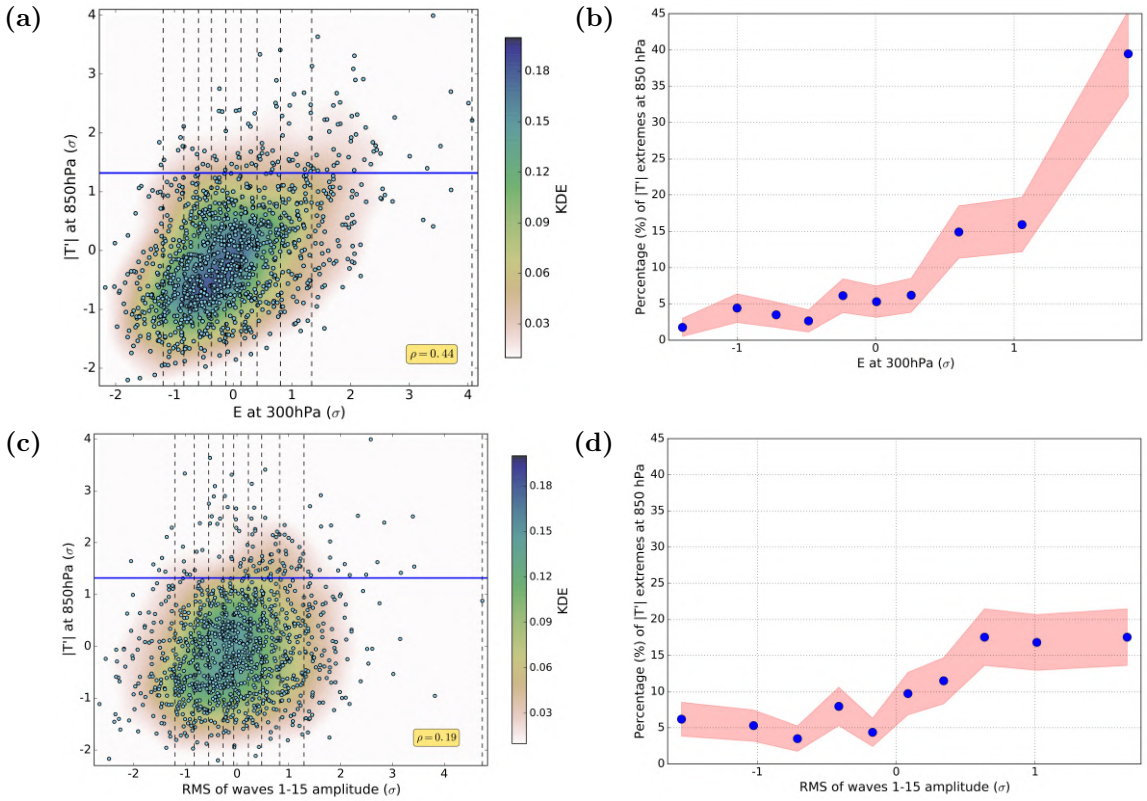

Fig. 3.3: *Analysis of the temporal correlation between daily mean RWP amplitudes at 300 hPa and temperature anomalies at 850 hPa for the 36–56°N , 0–20°E region in Europe during JJA. (a) Scatter plot of normalized $|T'|$ against normalized E. The colour shading depicts a kernel-density estimate using Gaussian kernels. The vertical dashed lines indicate specific quantiles of the values for E separating the data in 10 equally populated bins. The horizontal blue line depicts the 90^{th} percentile of the temperature distribution. The Spearman's rank correlation coefficient is shown in the yellow box. (b) Percentage (%) of temperature extremes (daily average $|T'| > 90^{th}$ percentile) in each E-bin, where each E-bin is represented on the abscissa by its median. The red shading shows the statistical uncertainty $\Delta P_{\mathrm{ex}}(E)$ of each value. (c), (d) Same as (a) and (b), except that the horizontal axis now refers to the normalized Fourier amplitude instead of RWP amplitude (see text for explanation).*

is significantly larger on days with a strong RWP amplitude, compared to other days with weaker RWP amplitudes. To quantify this connection, we plot in Figure 3.3b the percentage $P_{\mathrm{ex}}(E)$ of days with extreme temperatures for each E-bin. $P_{\mathrm{ex}}(E)$ can be interpreted as the probability of a temperature extreme for a given value of the RWP amplitude. The red shading indicates the statistical uncertainty (ΔP_{ex}), which we estimated as

$$\Delta P_{\mathrm{ex}}(E) = \Delta \left(\frac{n_{\mathrm{ex}}(E)}{n(E)} \right) = \frac{\Delta n_{\mathrm{ex}}(E)}{n(E)} = \frac{\sqrt{n_{\mathrm{ex}}(E)}}{n(E)} \,, \tag{3.3}$$

where $n(E)$ is the total number of points in the E-bin and $n_{\mathrm{ex}}(E)$ is the corresponding number of extreme temperatures in this bin. Given this sampling, there is a near-exponential increase of $P_{\mathrm{ex}}(E)$ with RWP amplitude for the considered region in Europe. On a day with a very large RWP amplitude (above the 90^{th} percentile of the RWP amplitude distribution), the probability for a warm/cold temperature extreme is approximately 40%. Furthermore, since each bin is one tenth of the sample size and temperature extremes also constitute 10% of it, this result can be interpreted in an equivalent way by saying that approximately 40% of all the temperature extremes occur in the highest E-bin (corresponding to the 90^{th} percentile).

As mentioned in the introduction, there has been a number of earlier investigations on the connection between temperature extremes and atmospheric dynamics, and some of these studies used Fourier amplitudes to quantify the waviness of the upper-tropospheric flow in this regard. Therefore, we will now address the question of how appropriate Fourier amplitudes are in quantifying the connection between an individual temperature extreme and upper-tropospheric waviness. For this purpose we repeated the above analysis except that we replaced the RWP amplitude over the region in Europe by the normalized root mean square of the Fourier transform zonal wavenumber 1–15 amplitudes of the 300 hPa v', meridionally averaged over 36–56°N . Figures 3.3c and 3.3d show the corresponding scatter plot and quantile analysis in a similar format as in Figure 3.3a and 3.3b, respectively. Apparently, the correlation in Figure 3.3c is much less pronounced than in Figure 3.3a, with a much lower value $\rho = 0.19$ (instead of 0.44) of the Spearman's correlation coefficient (again, the value of ρ is statistically significant against the null hypothesis of no correlation). As a result, the increase of P_{ex} with Fourier amplitude in Figure 3.3d is much weaker than the corresponding behaviour in Figure 3.3b. This is due to cases where a temperature extreme is associated with high waviness confined over Europe and relatively weak Fourier amplitudes.

In the null-case of no statistical connection between upper-tropospheric waviness and temperature extremes, each point in Figures 3.3b and 3.3d would be associated with roughly the same fraction of temperature extremes, i.e. 10% plus/minus statistical fluctuations, and the function P_{ex} would be more or less flat. To the extent that there is a non-trivial statistical connection, one expects the function values on the ordinate to increase with increasing values on the abscissa. Motivated by this, we quantify the strength of the statistical connection between upper-tropospheric waviness and 850 hPa temperature extremes by computing the fraction F between the value in the highest and the lowest bin in Figure 3.3b and 3.3d, respectively. We obtain $F = 39.5/1.8 \approx 21.9$ for the analysis with RWP amplitudes, but only $F = 17.5/6.2 \approx 2.8$ for the analysis with

Fourier amplitudes. Both results are statistically significant (the former even highly significant), as can be gleaned from the size of the uncertainty band (red) in relation to the difference between the respective values in the top and bottom bin. These results indicate that the RWP amplitudes are *much* more appropriate to quantify the connection between individual temperature extremes and upper-tropospheric waviness than Fourier amplitudes.

3.3.2 Extension to the entire Northern Hemisphere extratropics

It is not clear at this point to what extent the results of the analysis in Figure 3.3 carry over to other regions and seasons of the Northern Hemisphere. For reference, Appendix B provides Northern Hemisphere summer and winter regional climatologies for the 90^{th} percentile of $|T'|$ at 850 hPa, $|T'|$ at 2 metres, RWP amplitude (E), and the root mean square of the Fourier transform zonal wavenumber 1–15 amplitudes of the 300 hPa v' (Figure 3.13). The inter-regional and seasonal variability of the aforementioned fields facilitate the interpretation of the hemispheric analyses that follow.

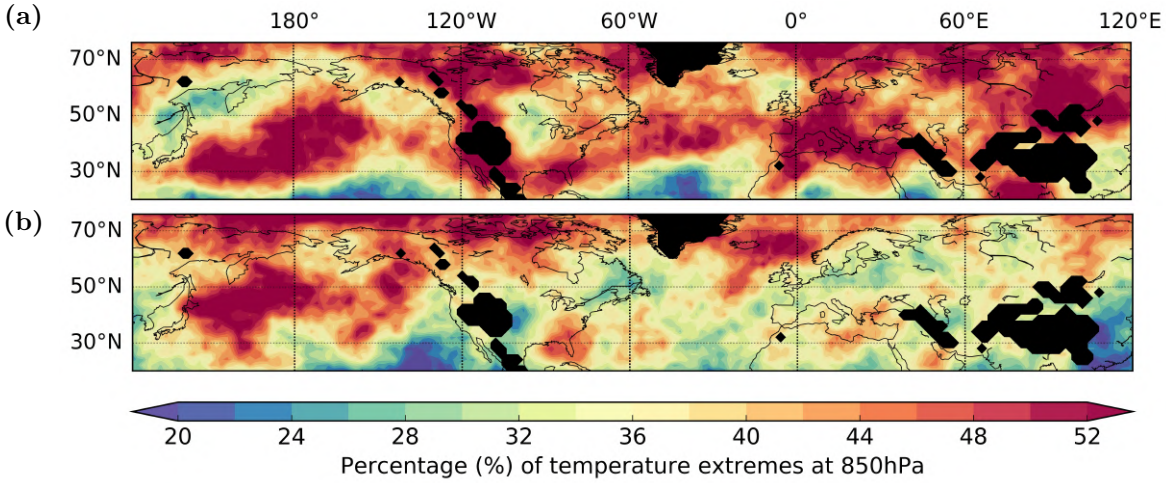

Fig. 3.4: *Percentage $\mathcal{P}$ of temperature extremes at 850 hPa for (a) JJA and (b) DJF days with strong upper-tropospheric waviness, as measured by RWP amplitudes. The value for each grid point corresponds to the $20^\circ \times 20^\circ$ region that is centered on it. Grid points with a mean surface pressure below 850 hPa are indicated in black.*

We repeat the correlation analysis from the previous subsection for individual $20^\circ \times 20^\circ$ regions centered on every grid point in the Northern Hemisphere extratropics for both summer (JJA) and winter (DJF). In order to compress information, we keep for each grid point only the percentage P_{ex} of days with extreme temperature that occur in the top 20% of RWP or Fourier amplitudes, respectively. In other words, we use:

$$\mathcal{P} = P_{\text{ex}}(\text{top 20\% RWP or Fourier amplitudes}) \tag{3.4}$$

as a measure for the connection between 850 hPa temperature extremes and 300 hPa waviness. The result for the summer season is shown in Figure 3.4a. In many areas

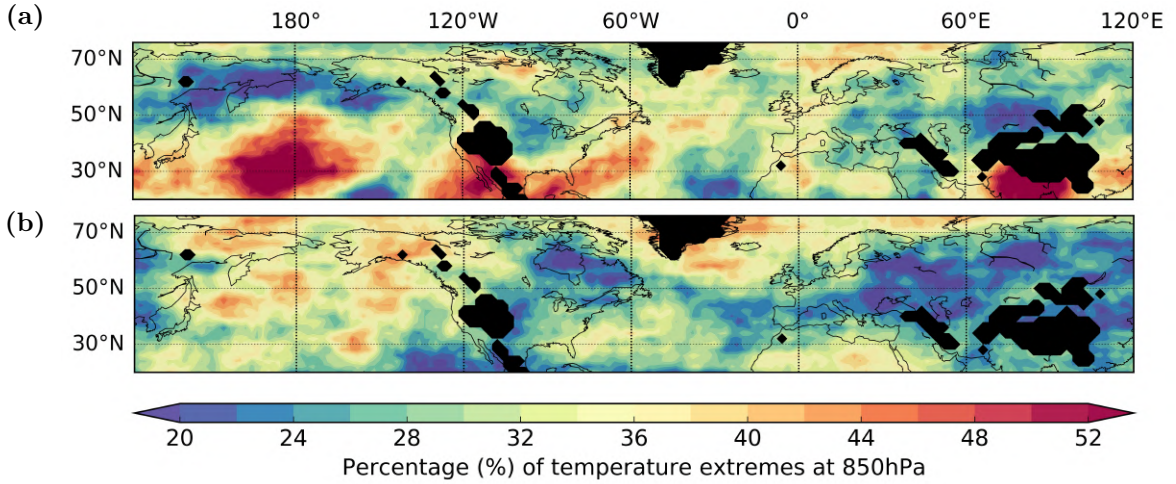

Fig. 3.5: *Percentage $\mathcal{P}$ of temperature extremes at 850 hPa for (a) JJA and (b) DJF days with strong upper-tropospheric waviness, as measured by Fourier amplitudes. For each grid point, $|T'|$ is averaged over the $20^\circ \times 20^\circ$ region that is centered on it and the corresponding Fourier amplitudes are calculated from the 300 hPa v' field, meridionally averaged over the 20° zonal band that covers the latitudinal extent of the respective region. Grid points with a mean surface pressure below 850 hPa are indicated in black.*

of the Northern Hemisphere, $\mathcal{P} > 50\%$, meaning that there is a greater than 50% probability of a temperature extreme occurrence on a day with a strong RWP amplitude (above the 80^{th} percentile). The areas of highest $\mathcal{P}$ include most of Europe, Central Asia, and parts of North America and the North Pacific. Notable minima occur north of the UK, in Central N. America, and in the Sea of Okhotsk. The corresponding plot for the winter season is shown in Figure 3.4b. In this case the connection between E and $|T'|$ is not as strong as in summer (compare with Figure 3.4a). Inherent differences in the dynamic and thermodynamic characteristics of the two seasons account for the different $\mathcal{P}$ distributions. Some discussion on the issue is given in section 3.4.

The connection with Fourier amplitude is, again, much weaker than the connection with RWP amplitude, and similarly the values of $\mathcal{P}$ in winter are lower than those in summer (Figures 3.5a, 3.5b). This result corroborates that throughout the Northern Hemisphere, Fourier amplitudes are less appropriate to quantify the link between upper-tropospheric waviness and individual temperature extremes than RWP amplitudes; and in most regions the difference between the two methods is substantial. The reason for this result is fairly straightforward: an individual temperature extreme of synoptic scale does not require a circumglobal Rossby wave; rather, a more localized wave packet is sufficient. Of course, even a localized RWP can be decomposed in a Fourier series, but the resulting Fourier amplitudes are smaller than for a circumglobal Rossby wave of similar amplitude. In this regard, a "sharper" diagnostic of upper-tropospheric waviness like the RWP amplitude provides essential inter-regional information when studying the climatological linkage to lower-tropospheric temperature extremes.

3.3.3 Near-surface temperature anomalies

So far a clear link between upper-tropospheric RWP amplitude and 850 hPa temperature extremes has been found. However, this does not necessarily imply a similar link with near-surface temperature extremes. Various boundary layer processes (associated with e.g. topography, low clouds, soil moisture) can have an impact on the strength of this link, and these processes may vary with location and time. Figure 3.6 shows the connection between RWP amplitude and 2-metre temperature extremes. As expected, during both summer and winter, the values of $\mathcal{P}$ are lower than for the corresponding analysis with 850 hPa temperature. However, during summer there are still several areas in the Northern Hemisphere with $\mathcal{P} > 40\%$ (e.g. most of Europe, Central Asia and West North America). Taking the 2-metre temperature extremes, we obtain $F = 26.3/4.4 \approx 6.0$ over the European region considered in section 3.3.1. This is still much larger than 1, but considerably lower than for the corresponding analysis with 850 hPa temperature extremes (see above).

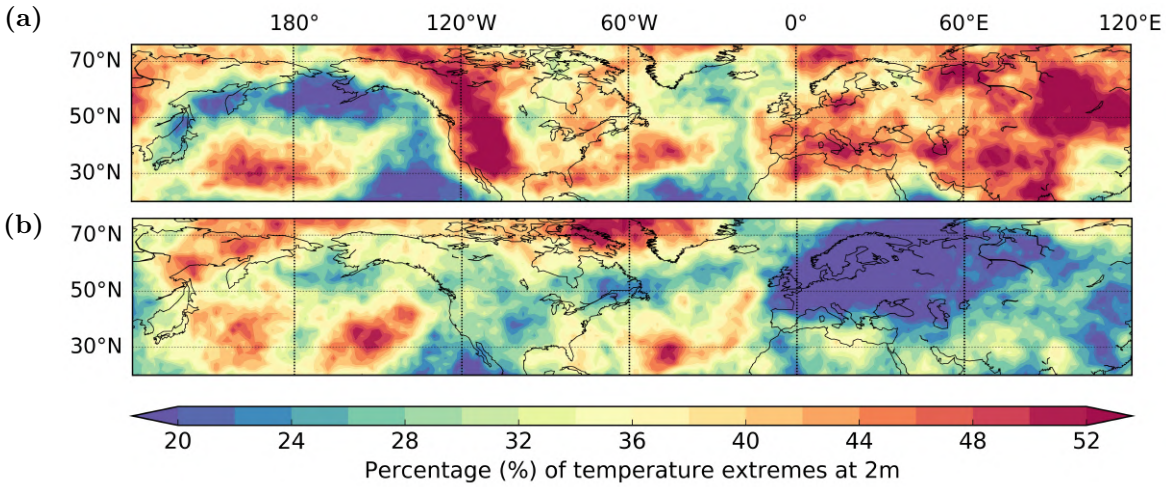

Fig. 3.6: *Percentage $\mathcal{P}$ of temperature extremes at 2 metres for days with strong RWP amplitude for (a) JJA and (b) DJF during 1979–2015. The value for each grid point corresponds to the 20°× 20° region centered on it.*

The above result implies that the correlation between 850 hPa and 2-metre temperature anomalies must be subject to substantial inter-regional and seasonal variability. For illustration we consider first two European sites, Madrid and London, during summer. For this analysis, the arithmetic mean of the 1200 and 1800 UTC temperature anomalies (in the $2° \times 2°$ grid points that correspond to these sites) is used instead of daily mean temperature anomaly. Figure 3.7 shows the scatter plot, in which each point is located such that 2-metre temperature is taken on the abscissa and the corresponding 850 hPa temperature is taken on the ordinate. The temperature values are expressed in percentiles of their distribution in order to facilitate the comparison between different locations.

The Madrid area shows a good correlation between the temperatures at both levels, with a rather pronounced symmetry about the diagonal ($x = y$ axis). The correlation is particularly good at the extreme ends of the distribution, i.e. for pronounced temperature anomalies. In contrast, the correlation for the London area is

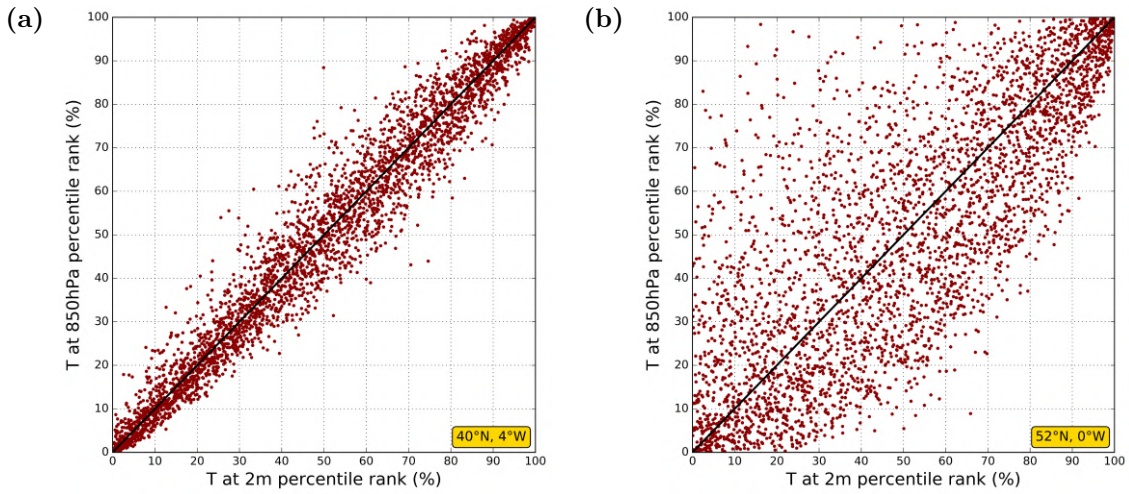

Fig. 3.7: *Comparison between temperature anomalies at 850 hPa and 2 metres using the 1200 and 1800 UTC average values at two European sites: (a) 40°N , 4°W (Madrid) and (b) 52°N , 0°E (London). The plot contains data for all Northern Hemisphere summer days between 1979 and 2015. The temperature values are expressed in percentiles of the corresponding distribution. The black diagonal depicts the $x = y$ axis.*

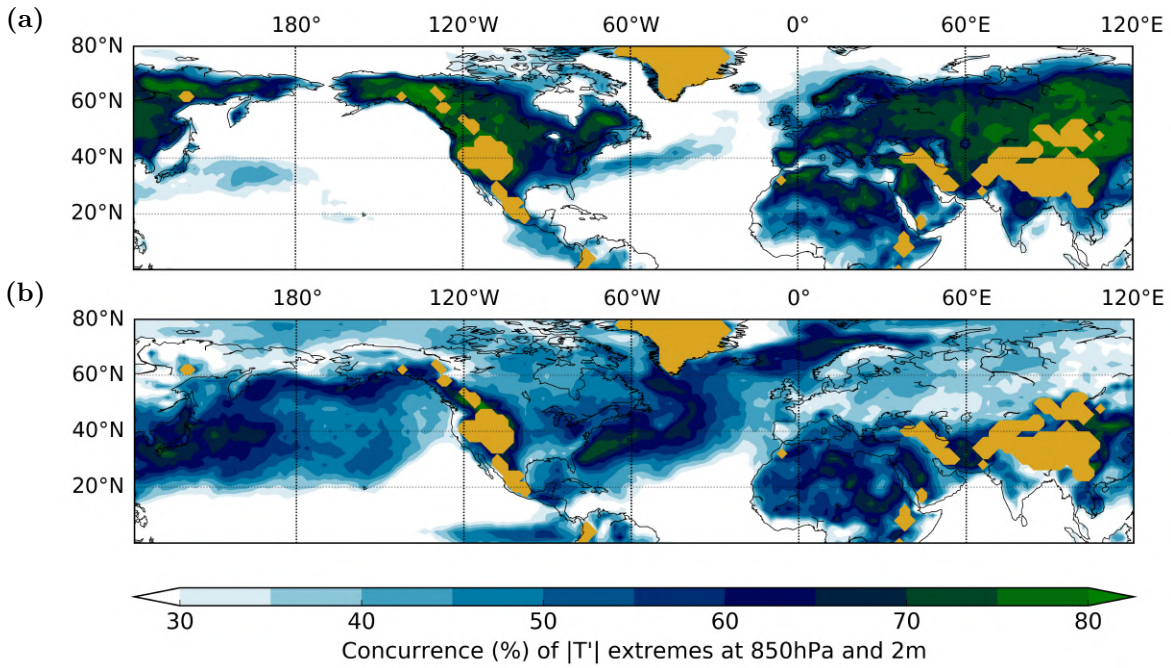

Fig. 3.8: *Concurrence C_2^{850} in percentage between 850 hPa and 2-metre temperature extremes for (a) JJA and (b) DJF during 1979–2015. Grid points with a mean surface pressure below 850 hPa are indicated in orange.*

much weaker, showing a strong scatter of the points at the extreme ends of the distribution and a pronounced asymmetry about the diagonal. For example, while strong warm anomalies at 2 metres in London almost always coincide with a strong warm anomaly at 850 hPa, the reverse is not true, i.e. strong warm anomalies at 850 hPa are not necessarily associated with strong warm anomalies at 2 metres. Distinct topography and boundary layer properties in these two sites account to some extent for these differences.

The link between 850 hPa and 2-metre temperature extremes is now systematically analyzed for the entire Northern Hemisphere. The question we want to address is what percentage of the 850 hPa temperature extremes ($|T'_{850}| > 90^{th}$ percentile) coincides with 2-metre temperature extremes ($|T'_{2\mathrm{m}}| > 90^{th}$ percentile). For this analysis we again use daily mean temperatures for each grid point at both levels in order to be consistent with the temporal resolution used in the previous subsections. We divide the number of simultaneous occurrences of temperature extremes at both levels by the number of 850 hPa temperature extremes. The resulting fraction C_2^{850} for JJA (Figure 3.8a) shows a large inter-regional variability, with the oceans generally featuring a much weaker linkage than the continents. This is presumably due to the fact that the 2-metre temperature field over the ocean surface is more strongly influenced by the sea surface temperature (SST) than by the atmospheric temperature at 850 hPa. On the other hand, the continents show values as high as $C_2^{850} \approx 60$–70%. Maxima occur in mountainous regions, which is likely due to the proximity of the 850 hPa and 2-metre levels (areas with a mean surface pressure below 850 hPa are masked out).

The corresponding analysis for the winter season is shown in Figure 3.8b. The inter-regional variability pattern is strikingly different compared to the summer season. For instance, in contrast to the summer season, winter is characterized by a non-negligible connection between the two levels over the oceans, especially in the storm track regions. Here, the strong lower-tropospheric winds and temperature gradients suppress the impact of the SST on the oceanic 2-metre temperatures. On the other hand, the connection between the two levels over the continents is generally lower compared to summer, presumably related to the occurrence of low-level inversions (see also discussion in section 3.5).

3.4 The heat waves of 2003 and 2010

We now proceed from a statistical to a case-based analysis and investigate two prominent synoptic-scale temperature extremes, viz. the 2003 western European heat wave and the 2010 Russian heat wave. These two events have been studied quite extensively from a subseasonal-to-seasonal and climate perspective (e.g. Meehl and Tebaldi 2004; Fischer *et al.* 2007b; Otto *et al.* 2012; Hauser *et al.* 2016; Petoukhov *et al.* 2013a), whereas fewer studies have focused on the daily evolution of synoptic weather systems (Black *et al.* 2004; Fink *et al.* 2004; Schneidereit *et al.* 2012). Since both of the affected regions are associated with high values of $\mathcal{P}$ (Figure 3.4a), it appears constructive to inspect the day-to-day linkage between upper-tropospheric waviness and lower-troposphere temperature anomalies over these regions during the two heat waves. In this regard, focusing on the role of upper-tropospheric RWPs will provoke

novel considerations about the two events and will also contribute to our objective by emphasizing the advantages of diagnosing waviness locally.

To set the stage, we show in Figure 3.9 the HWMId (section 3.2.4) for a representative 11-day period during each of these events. In both episodes, the index shows strong deviations from climatology in an extended area. As an indication, areas with an HWMId value of 20 experienced a positive daily maximum 2-metre temperature (T_{dm}) deviation from the 25^{th} percentile (T_{25p}) that was on average 2 times the climatological interquartile range ($T_{75p} - T_{25p}$) for 11 days. In the 2003 case, the largest 11-day HWMId accumulations are found over France, but many more parts of western Europe were also severely affected. (Since the index is based on 2-metre temperature, the maximum over the North Atlantic carries an imprint of anomalously warm SSTs.) During the 2010 event mainly western Russia and parts of Ukraine and Belarus were the affected regions.

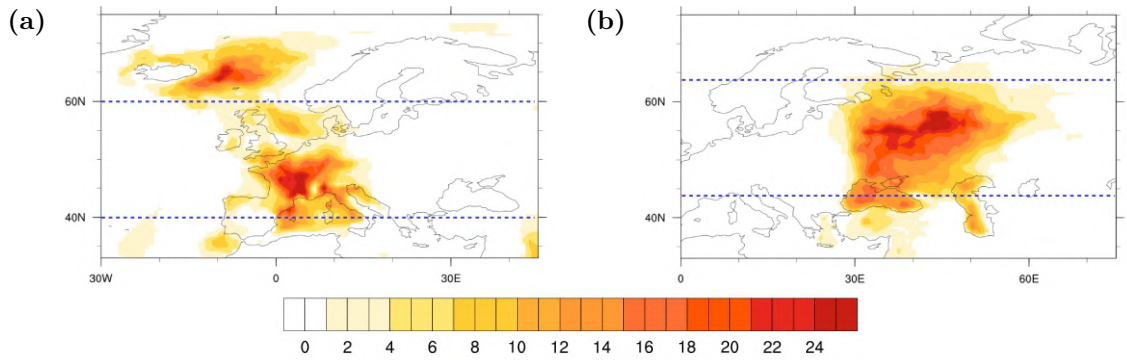

Fig. 3.9: *HWMId (dimensionless) for (a) 4–14 August 2003 and (b) 2–12 August 2010. The blue dashed lines indicate the latitude band of 850 hPa temperature anomaly averaging in Figure 3.10.*

Hovmöller diagrams have traditionally been used in reducing the complexity of the 4-dimensional evolution of RWPs by representing aspects of their propagation in longitude-time coordinates (Glatt *et al.* 2011). In Figure 3.10, 850 hPa temperature anomaly and RWP amplitude during the two heat waves are superimposed on Hovmöller diagrams that span the same period of the two summers. The temperature anomalies have been averaged over a 20° latitude band that roughly covers the affected areas during the respective heat wave (Figure 3.9). For the latitudinal averaging of RWP amplitude E it proved beneficial to use a more sophisticated algorithm, since not all RWPs propagate on the same latitude bands and each of them does not necessarily follow a purely zonal track (see e.g. Figure 3.11). First, the latitudinal interval used for the temperature anomalies was extended both northwards and southwards by 10°, resulting in an averaging interval of 40°. Within this interval we only averaged over those 20° where the highest values of E occur in a given day. This implies effectively an average over 20 degrees in latitude as in the case of temperature anomaly, but the averaging latitude range self-adjusts, such that it automatically follows the RWP location as quantified through E. Applying this algorithm will also be advantageous in cases of a split RWP (high waviness in distinct latitude bands of the same longitude). Finally, a weak bivariate interpolation (using cubic Hermite splines) is applied to slightly smoothen the resulting RWP contours.

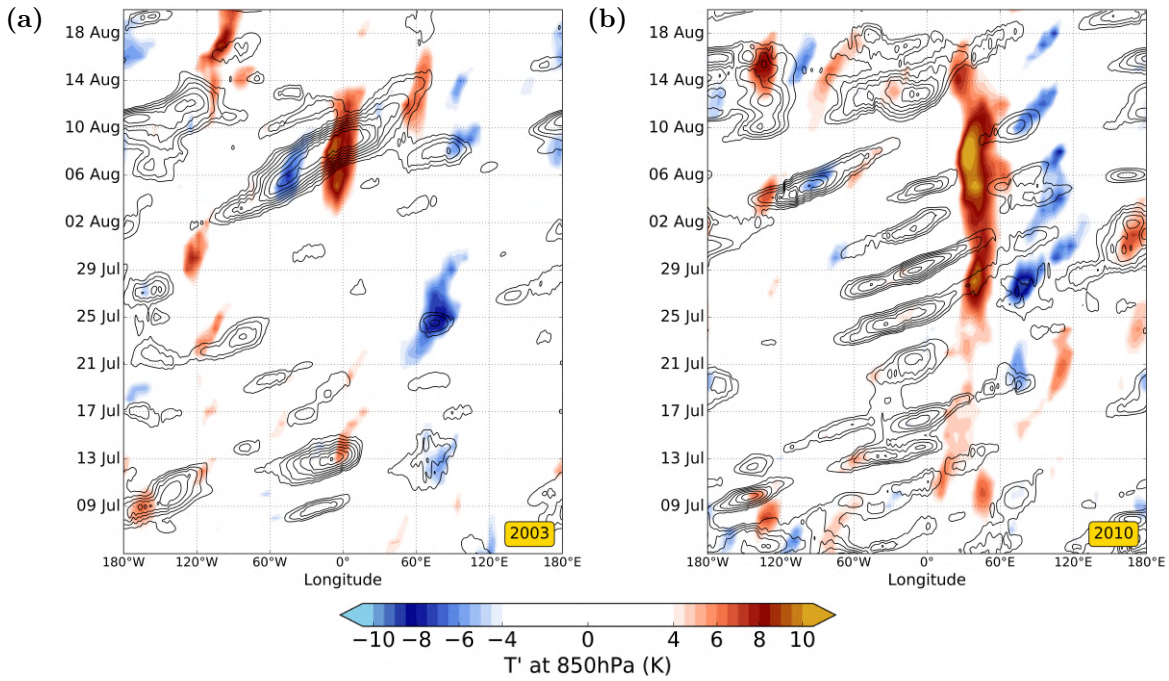

Fig. 3.10: *Hovmöller diagrams of temperature anomalies and RWP amplitudes for (a) the 2003 heat wave, and (b) the 2010 heat wave. The colour fill depicts 850 hPa T' (in K), averaged over 40–60°N in (a) and over 44–64°N in (b). The black contours depict the latitudinal average of 300 hPa E (every 2 ms^{-1}, starting from 20 ms^{-1}). The latitudinal averaging for E is explained in the text.*

The first aspect to note in Figure 3.10 is that for both events the upper-tropospheric waviness was restricted to a part of the hemisphere. This nicely illustrates our point, that RWPs are more relevant in connection with temperature extremes than circumglobal Rossby waves. The situation is quite similar to the longitudinally confined RWP during the 1988 heat wave (Figure 3.1). In addition, although the heat waves of 2003 and 2010 were of similar intensity, Figure 3.10 shows that the 2003 event was much shorter-lived ($\sim$ 2 weeks) than the 2010 event ($\sim$ 5 weeks).

After an anomalously hot June (not shown here), July 2003 was characterized by slightly above normal temperatures over Europe (Fink *et al.* 2004). This was coincident with a relatively minor RWP activity over the North Atlantic and Europe, except during a short episode on 11–15 July (Figure 3.10a). In contrast, the first half of August was characterized by an anomalously strong and long-lasting RWP that formed at around 110°W and vanished in mid-August at around 70°E . This RWP acquired its maximum amplitude over the North Atlantic and Europe on 7–9 August, coincident with the hottest days over western Europe. Figure 3.11 illustrates in more detail the progression of this RWP, as represented by areas of very strong (35 ms^{-1}) RWP amplitude. During this period, it slowly propagated eastward from Newfoundland (August 5^{th}) and reached its highest intensity and extent over Northern Europe on August 9^{th} . Thereafter it started to weaken gradually.

The key question now is how did the RWP shown in Figures 3.10a and 3.11 contribute to the heat wave. A partial answer can be obtained through analysis of

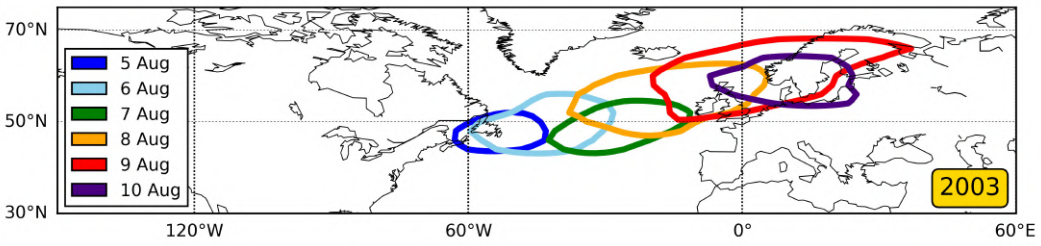

Fig. 3.11: *Location of the RWP highest amplitudes ($E = 35\ ms^{-1}$) on consecutive days between the 5^{th} and 10^{th} of August during the 2003 heat wave. Each colour contour represents a different day (see legend).*

the upper-tropospheric meridional wind anomaly v' in Figure 3.12a. For consistency, in each time-longitude point of the Hovmöller diagram, v' (colour fill) is averaged over the same latitudes as E. Apparently, the succession of northerly and southerly anomalies in the meridional component of the wind field, that constitute the RWP, propagate only very slowly in the zonal direction (approximately 3° longitude per day). This contrasts with the propagation velocity of the entire RWP, which corresponds to a group velocity of about 15° longitude per day (green arrow in Figure 3.12a). The underlying phenomenon has long been known as "downstream development" (Simmons and Hoskins 1979), and indicates the transfer of wave energy toward a developing disturbance downstream (Chang 1993).

The observed quasi-stationarity of strong southerlies to the west of Europe was associated with a strong ridge-building downstream over the affected areas. This ridge presumably played a major role in an initial northward advection of the background isotherms and later in favouring and sustaining clear skies and in situ warming by adiabatic compression in subsiding air masses (Black *et al.* 2004; Bieli *et al.* 2015b). The persistent anticyclonic conditions and precipitation deficit of the preceding months led to reduced soil moisture and anomalously warm SSTs, thus creating a susceptible environment and contributing to the rapid warming during the early stages of the event (3–5 August) and its eventual peak magnitude (Fischer *et al.* 2007a; Hirschi *et al.* 2011; Feudale and Shukla 2011). The spatially-varying impact of the aforementioned processes within the large-scale ridge and the sensitivity to the thermodynamic properties of the air masses prior to the arrival of the RWP suggest that severely affected areas should not necessarily be exactly collocated with areas of peak RWP amplitude (Figures 3.9a, 3.11).

Unlike the 2003 case, the 2010 heat wave is characterized by a continuous succession of strong RWPs over the North Atlantic and Europe (Figure 3.10b). At the same time there is a gradual build-up of anomalously warm temperatures in Western Russia. Figure 3.12b reveals that at the longitudes where the RWPs started decaying (i.e. around 0–30°E), they were always associated with a strong southerly wind component. The consecutive passages of RWPs and the variable strength of the embedded southerlies is associated with the western flank of an intermittent atmospheric block over Russia, as investigated in previous studies (Matsueda 2011; Schneidereit *et al.* 2012). In the latest phase of the event, the RWPs started to weaken (around the 6^{th} of August), but southerlies — not clearly embedded in a larger-scale RWP — were main-

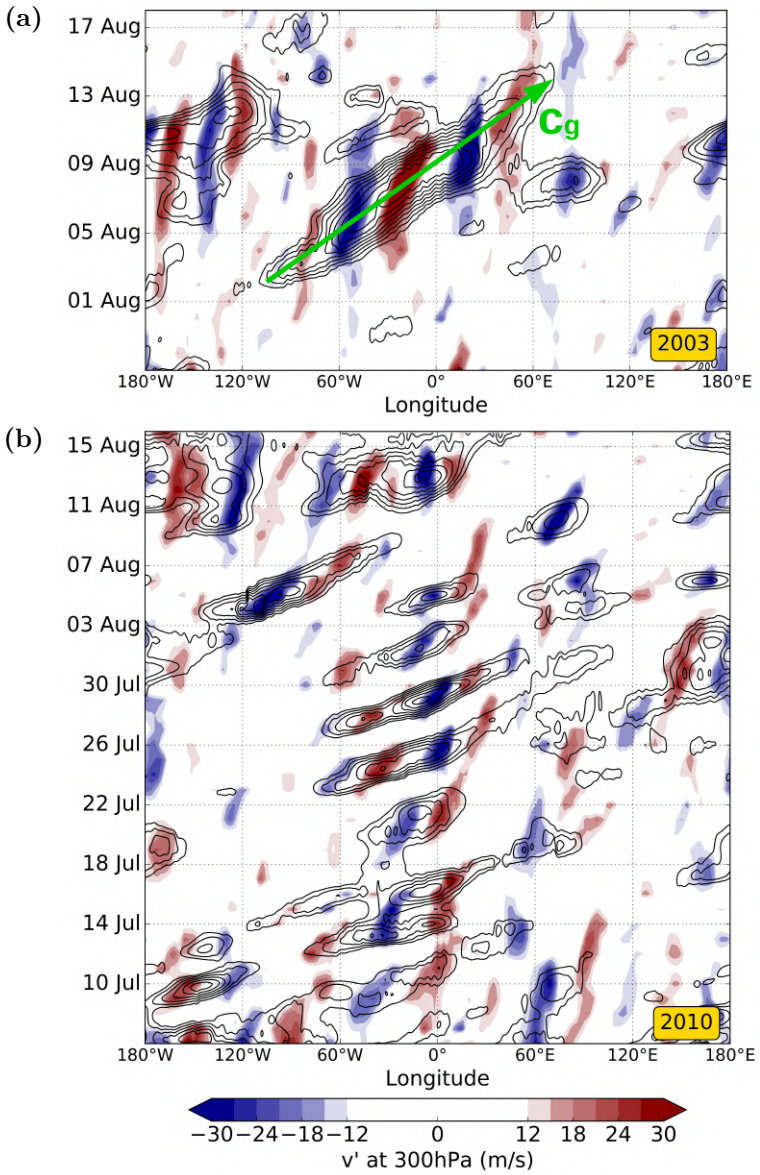

Fig. 3.12: *Hovmöller diagrams illustrating the upper-tropospheric flow for (a) the 2003 heat wave, and (b) the 2010 heat wave. The black contours depict the latitudinal average of 300 hPa E (every 2 ms^{-1}, starting from 20 ms^{-1}). The colour fill depicts 300 hPa v′. Finally, the green arrow in (a) indicates the group velocity ($\boldsymbol{c_g}$) of the RWP.*

tained for a few more days. At this stage land–atmosphere feedbacks and the formation of deep and warm nocturnal residual layers effectively contributed in the intensification of the event (Lau and Kim 2012; Miralles *et al.* 2014). It was during this period (4–10^{th} of August), that the heat wave reached its maximum intensity (Figure 3.10b). Interestingly, this late period was also characterized by poor predictability, with several weather forecasting centres underestimating the severity of the event (Matsueda 2011; Quandt *et al.* 2017).

This analysis transpires that although both heat waves were associated with strong RWPs, there were also some striking differences. For instance, in 2003, one strong RWP was coincident with the most extreme part of the heat wave. In contrast, in 2010, consecutive RWPs seemed to contribute in establishing the heat wave, while its phase of peak intensity was accompanied by rather weak RWP activity. This suggests that, depending on their characteristics (amplitude, structure, group velocity, phase velocity of embedded eddies, etc.) and the interplay with other physical processes, there may be various direct or indirect mechanisms through which a RWP contributes to a heat wave or temperature extreme in general.

3.5 Summary and discussion

This study focused on the linkage between Rossby wave packets and temperature extremes in the Northern Hemisphere. We found that in many regions of the mid-latitudes the presence of large-amplitude RWPs in the upper troposphere is associated with a considerably increased probability of lower-tropospheric temperature extremes. A significant inter-regional and seasonal variability in this correspondence was observed. Furthermore, it was found that in most regions the non-circumglobal RWP amplitudes are much better linked to temperature extremes than Fourier amplitudes quantifying circumglobal waviness. The advantage of identifying and following the evolution of RWPs was also revealed in two specific cases of recent extreme heat waves. Although the connection between RWP amplitude and temperature anomaly was not straightforward at every instance during the two episodes (suggesting more mechanisms at work), both heat waves were associated with conspicuous non-circumglobal RWP activity.

In the past, several studies used a Fourier analysis of the upper-tropospheric meridional wind or geopotential height in order to link temperature extremes to amplified planetary waves in daily to monthly mean datasets (Petoukhov *et al.* 2013a; Screen and Simmonds 2014; Coumou *et al.* 2014; Kornhuber *et al.* 2017c). As Hoskins and Woollings (2015) pointed out, even regionally confined RWPs inevitably possess power in a range of zonal wavenumbers when subjected to Fourier analysis. However, this does by no means imply the existence of circumglobal waves. Furthermore, temporal and zonal averaging in the aforementioned studies obscures essential information on the synoptic evolution and may lead to a misleading impression about the characteristics of the extremes and the role of the upper-tropospheric circulation. For example, time filtering (e.g. 15-day running mean or monthly mean) may give equal weight to a strong but short-lived anomaly and a weak but persistent anomaly. In addition, such a time filtering in the case of the 2010 heat wave, for example, would conceal the successive eastward propagation of longitudinally confined maxima in upper-tropospheric wave

amplitude (RWPs). Similarly, zonal averaging may give equal weight to strong but regionally restricted and weak but hemispherically extended anomalies. Peaks in the zonally averaged zonal wind (in particular), cannot be safely interpreted or attributed to specific flow regimes. We believe that these distinctions are essential in the context of weather extremes. Indeed, the two specific cases that we investigated showed that heat waves of similar strength can be associated with highly distinctive daily evolutions of the upper-tropospheric circulation. It appears necessary to account for such differences in order to unravel the relevant mechanisms and improve our understanding of weather extremes.

As a step forward, in the present study we used the concept of RWPs, the presence of which suggests that waviness in the upper troposphere is typically not stretched out circumglobally, but organized in eastward propagating patches of limited spatial extent. Investigation of these structures is important because they embody and possibly moderate the synoptic-scale systems (cyclones, blocks, etc.) that are associated with regional flow patterns and physical processes within those patterns that favour the occurrence of temperature extremes (Kyselý 2008; Pfahl and Wernli 2012; Bieli *et al.* 2015b; Chang *et al.* 2016). Consequently, using the RWP amplitude as an upper-tropospheric waviness metric gave us a more direct link to lower-tropospheric temperature extremes. In a similar vein, Röthlisberger *et al.* (2016) employed a regional-scale jet waviness diagnostic using the geometry of the 2 PVU contour on an upper-tropospheric isentrope and showed that it has a clearer link to weather extremes than a hemispheric jet waviness metric.

The observed variability in the connection between RWP amplitude and synoptic-scale temperature extremes revealed noticeable differences between the summer and winter seasons (Figures 3.4, 3.6). Apart from some regions to the north of UK and in the Gulf of Alaska, most parts of the Northern Hemisphere mid-latitudes had a reduced $\mathcal{P}$ during winter (fewer temperature extremes occurring in the top 20% E compared to summer). This decrease was more pronounced in areas of North America, North Atlantic, Europe and Central Asia. Given our analysis, this summer-winter difference can occur because during winter there are more mechanisms that lead to $|T'|$ extremes in days without a strong RWP amplitude (involving e.g. mesoscale vorticity features of wave-breaking, strong temperature advection from zonal winds or enhanced orographic effects) and/or because some winter synoptic systems are associated with enhanced upper-troposphere waviness but no equivalent anomalies in the lower-troposphere temperatures. Both of these cases will lead to reduced $\mathcal{P}$. An in-depth investigation of the inherent dynamic and thermodynamic characteristics of the two seasons would be required to fully explain the seasonal variability of $\mathcal{P}$. One thing to note is the extended variability in both E and 2-metre/850 hPa $|T'|$ during winter, as indicated by the respective 90^{th} percentile climatologies (Figure 3.13). In addition, persistent winter-time inversions in the lower-tropospheric temperature profile caused by compressional warming in subsiding air within high pressure systems or by surface radiative cooling (particularly effective in dry continental regions with long nights) lead to a stable lower troposphere and the gradual formation of compact air masses with characteristic temperature and relative humidity (acquired by the underlying surface properties). These air masses are then advected away by the strong synoptic systems of winter, temporarily maintaining their temperature (unperturbed by strong surface

fluxes and convection; a characteristic of summer) and potentially passing over a region with different characteristics, thus causing large temperature anomalies or instability followed by organized precipitation. Such situations may lead to one of the two cases reducing $\mathcal{P}$ as described before.

One limitation in our work arises when using the RWP amplitude as the only metric to quantify the linkage between upper-tropospheric waviness and lower-tropospheric temperature extremes. For instance, this linkage may become even stronger when taking into account the phase velocities of the embedded troughs and ridges and the initial thermodynamic properties of the air masses underneath. When the troughs and ridges propagate slowly in the zonal direction, they favour and maintain processes that can intensify the lower-tropospheric temperature anomalies and lead to temperature extremes. We showed that this was true for the two heat waves considered, but it is conceivable that this is not always satisfied. In fact, the intermittent heat wave over Europe in August–September 2016 may be such a case, where a large phase velocity prevented a long-lasting heat wave (Zschenderlein et al., 2018; personal communication). In addition, when a lower-tropospheric air mass is already warmer (colder) than average, an incoming RWP with only moderate amplitude may still be enough to favour a hot (cold) extreme. Another limitation, that is left for future work, comes from the fact that our two-dimensional RWP amplitude field detects all synoptic systems that are associated with a strong meridional wind component in the upper troposphere, without distinguishing between systems that favour explicitly hot or cold temperature extremes (see also: Appendix A). Regarding the two cases of the 2003 and 2010 heat waves, a complete investigation of these events would require an analysis of many factors acting across multiple scales. Since our analysis aimed at specific considerations regarding the role of RWPs, the important contribution of other physical mechanisms (related e.g. to radiative transfer, SST, subsidence, soil moisture, etc.) was only briefly mentioned.

Based on the results presented in this study, we conclude that RWPs are closely connected with the occurrence of lower-tropospheric temperature extremes. This calls for enhanced efforts to better understand the mechanisms that lead to the amplification of RWPs and determine their velocity and track, with potential benefits both in the context of weather forecasting and for climate change research. Dedicated studies are also required to tackle questions raised by the intriguing inter-regional and seasonal variability that was found in our analyses. Complementing such investigations with studies on the role of other relevant physical processes mentioned in the text, would then pave the way to a better understanding of the predictability of temperature extremes and their characteristics in a changing climate.

Acknowledgements

We thank the ECMWF for providing access to the data used in this study. We are grateful to the reviewers for their remarks, as well as to Gabriel Wolf and Federico Grazzini for insightful discussions. The research leading to these results has been done within the Transregional Collaborative Research Center SFB/TRR 165 “Waves to Weather” funded by the German Science Foundation (DFG).

Appendix A: Sensitivity of the results

In our envelope calculation methodology we imposed a filter limiting the wavelength to the range 2000 – 10000 km. The corresponding results and implications turned out to be insensitive to small variations in the limits of this range of wavelengths. In addition, the results in Figures 3.3–3.6 where we only used every third date of the 1979–2015 summers do not change substantially by the inclusion/exclusion of more dates. Finally, when repeating the analyses of Figures 3.4 and 3.6 for the top 5% hot or cold temperature extremes instead of the top 10% of $|T'|$, it is revealed that in many regions the linkage with RWP amplitude is particularly good for temperature extremes of one sign and less so for the opposite one. A dedicated study would be needed to explore this observation further.

Our analysis does not assume nor imply a strict collocation and coincidence of strong upper-tropospheric RWP amplitude and lower-tropospheric (850 hPa, 2 metres) temperature extremes. The imperfect correlation we found is in part caused by spatio-temporal offsets (lags) between these fields, that are expected to occur in a case-sensitive manner. In order to avoid fragile assumptions about typical magnitudes of these offsets, in the analyses of Figures 3.3, 3.4 and 3.6 we tried to minimize such effects by looking at daily mean fields, averaged over the same $20^\circ \times 20^\circ$ area. Regarding the Fourier analysis, we tested using zonal wavenumber ranges which were narrower than 1–15 and more restricted to the typical wavelengths of transient Rossby waves (e.g. wavenumbers 5–9), but the loss of information resulted in even lower correlations with the temperature extremes.

The values in Figures 3.4, 3.5 and 3.6 quantify the percentage of $|T'|$ extremes (defined as $|T'| > 90^{th}$ percentile) in the highest two E-bins. We repeated the analysis using other metrics for the connection between 300 hPa RWP amplitude and 850 hPa temperature extremes, such as

(i) the Spearman's rank correlation coefficient (see Figures 3.3a, 3.3c),

(ii) the difference between the highest and lowest two E-bin averages and

(iii) the linear fit slope of the data points in Figures 3.3b and 3.3d.

In all cases the results and main conclusions remained qualitatively and quantitatively similar.

Regarding the Hovmöller diagrams (Figure 3.10), we tested several latitude bands for the latitudinal averaging (continuous or intermittent) and found, again, no substantial changes in our main results. In addition, the 2-metre temperature gives similar results as the 850 hPa temperature, no matter whether we averaged over all grid points or over land grid points only.

Finally, we repeated our analysis with RWPs diagnosed from the meridional wind at 200 hPa and 500 hPa, instead of 300 hPa, which was chosen in this study as an indicative level for the study of Rossby waves. The magnitudes of meridional wind anomalies are changing, and the detected RWP amplitude fields are not perfectly collocated at these three levels. As expected, the correlations with $|T'|$ at 850 hPa are slightly increased (decreased) for RWP amplitude calculated at 500 hPa (200 hPa). For example, the equivalent analysis of Figure 3.3a gave Spearman's rank correlation coefficients of 0.52 and 0.39 for 500 hPa and 200 hPa respectively.

Appendix B: maps of the 90^{th} percentile of anomalies in temperature, RWP amplitude, and Fourier amplitude

As a complement to the analyses in section 3.3, Figure 3.13 shows maps of the Northern Hemisphere summer and winter 90^{th} percentile of daily mean temperature anomalies from climatology at 850 hPa and 2 metres for every $20^\circ \times 20^\circ$ region. These maps highlight the areas where temperature deviations tend to be large. Overall, daily mean temperature anomalies are higher in winter than in summer, and there is a poleward increase for both seasons. The values are generally lower over the oceans than over the continents, which is a well-known feature related to the difference between maritime and continental climates (Hartmann 2015).

Figure 3.13e and 3.13f show maps of the 90^{th} percentile of daily mean RWP amplitude anomalies. As with temperature, daily mean RWP amplitude anomalies are larger in winter than in summer, and generally they tend to be maximum over the storm track regions. As expected, the winter–summer difference is also evident in the corresponding maps of the root mean square of the Fourier transform zonal wavenumber 1–15 amplitudes of the 300 hPa v' (Figures 3.13g, 3.13h). By construction, the latter show no variation in longitude.

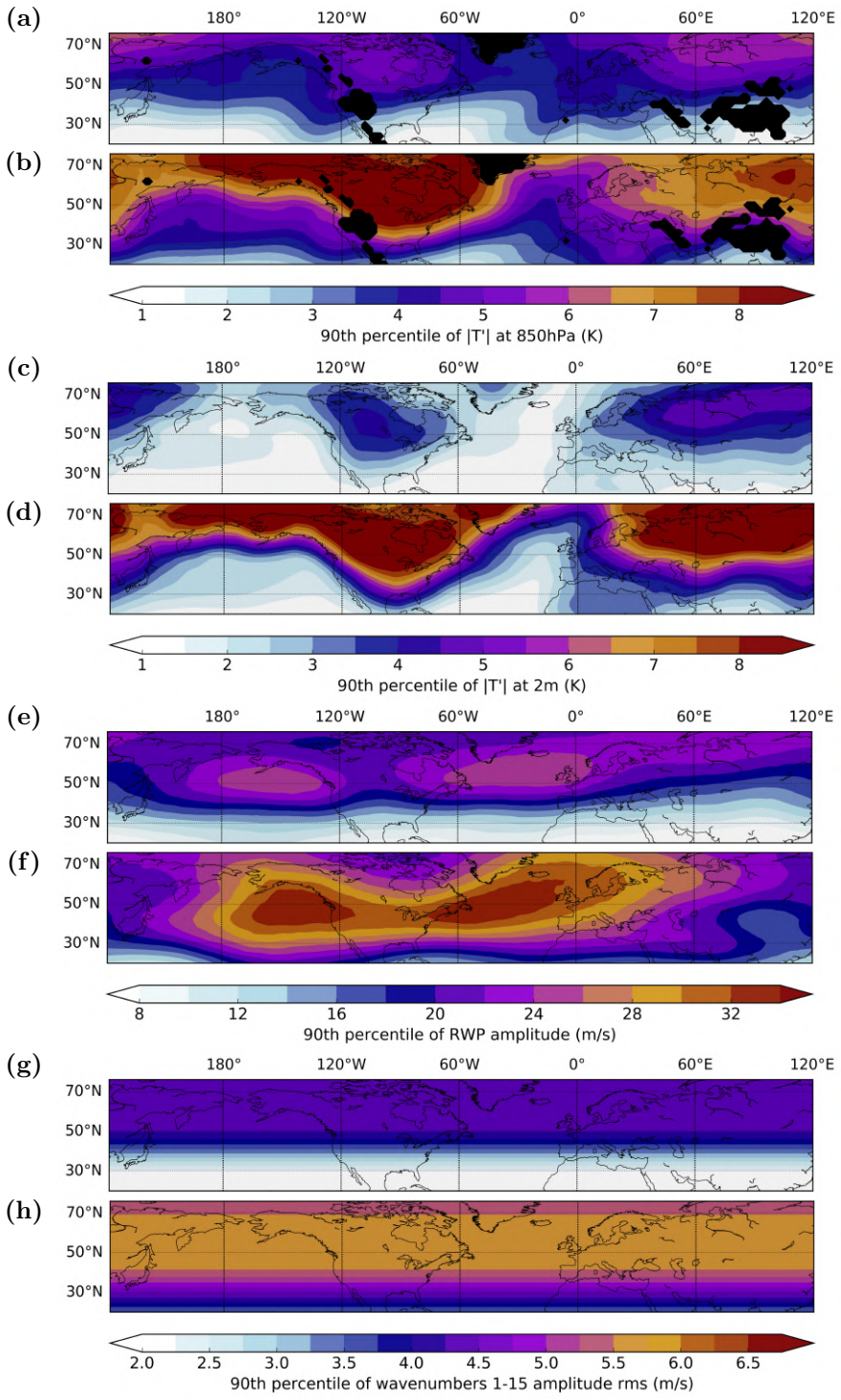

Fig. 3.13: *Summer (JJA) 90^{th} percentile of daily mean (a) $|T'|$ at 850 hPa (K), (c) $|T'|$ at 2 metres (K) (e) RWP amplitude (ms^{-1}) and (g) root mean square of the Fourier transform zonal wavenumber 1–15 amplitudes of the 300 hPa v'. (b), (d), (f), (h) Winter (DJF) 90^{th} percentile maps for the respective quantities. The percentiles in (a)–(f) are calculated for the spatial averages of the $20^\circ \times 20^\circ$ regions centered on every grid point. In (g) and (h), the values correspond to v', meridionally averaged in the 20° zonal band centered over every grid point. In (a) and (b) grid points with a mean surface pressure below 850 hPa are indicated in black.*

Chapter 4

Synoptic circulation patterns during temperature extremes in southeastern Europe

G. Fragkoulidis[a*] and V. Wirth[a]

[a] *Institute for Atmospheric Physics, Johannes Gutenberg University, Mainz, Germany*
[*] *corresponding author e-mail: gfragkou@uni-mainz.de*

This chapter is equivalent to the peer-reviewed article of homonymous title by the authors listed above that was published in the Proceedings of the 14th International Conference on Meteorology, Climatology and Atmospheric Physics in Alexandroupoli, Greece (Fragkoulidis and Wirth 2018). The manuscript is integrated as is into the dissertation and the section and figure numbers are adjusted accordingly. The references are listed in the unified bibliography at the end of the dissertation.

Abstract

This study investigates the synoptic circulation patterns associated with temperature extremes in southeastern (SE) Europe. Using ERA-Interim reanalysis data we report on the typical patterns that characterize the middle and upper tropospheric flow a few days before and during hot and cold extremes. The analysis is done separately for each season, while a further distinction between short-lived and persistent extremes reveals differences and similarities in the associated circulation, as inferred by the spatiotemporal evolution of Rossby wave packets (RWPs). Finally, the performance of ECMWF deterministic forecasts is evaluated for persistent cold and hot extremes during winter and summer respectively. Overall, this work suggests that a correct representation of the RWP evolution is crucial in determining the magnitude and persistence of temperature extremes in SE Europe.

4.1 Introduction

A better understanding of the physical processes that lead to weather extremes is essential for various reasons. From a weather forecast perspective, it proves beneficial in the challenges of identifying the predictability limits and interpreting forecast biases or "busts" associated with these events (Rodwell *et al.* 2013). From a climate perspective, investigating further the relevant processes will help in formulating hypotheses and evaluating model projections on the weather extremes characteristics of futures decades (Shepherd 2014). In this regard, recent studies have examined the possibility of far-upstream precursors to weather extremes by tracking transient Rossby Wave Packets (RWPs) in the upper-tropospheric flow (Martius *et al.* 2008; Fragkoulidis *et al.* 2018; Wirth *et al.* 2018).

This study focuses on the role of the middle and upper tropospheric circulation during abnormally hot and cold spells in southeastern (SE) Europe. This region is particularly interesting in terms of large-scale dynamics as it lies to the southeast of the climatological North Atlantic jet exit (where Rossby waves are typically in their mature nonlinear phase and frequently wave breaking is observed) and slightly northward of the subtropical jet (Sprenger *et al.* 2017). Using anomaly composites of reanalysis and forecast data we report on typical circulation patterns and forecast errors in the daily evolution of short-lived and persistent temperature extremes of both signs.

4.2 Data and methods

4.2.1 Data

Reanalysis data for meridional wind v at 300 hPa, geopotential height Z at 500 hPa, and temperature T at 850 hPa spanning a 38-year period (1979–2016) are retrieved on a $2^\circ \times 2^\circ$ horizontal grid with 6-hourly temporal resolution from the ERA-Interim reanalysis project (Dee *et al.* 2011). In addition, we use deterministic forecasts that were produced from the same ECMWF model (Integrated Forecasting System (IFS) model cycle 31r2) with the ERA-Interim analyses as initial conditions (Berrisford *et al.* 2009). Namely, 10-day forecasts at 12-hourly steps of v at 300 hPa and T at 850 hPa, issued daily at 1200 UTC, are retrieved on a $2^\circ \times 2^\circ$ horizontal grid.

4.2.2 Methodology

For all the retrieved data we calculate the daily mean anomalies (v', Z', T') from a climatological annual cycle as in Fragkoulidis *et al.* (2018). Since we are primarily interested in temperature extremes of large spatial extent in SE Europe, the following methodology to define hot and cold extreme events is used. We first detrend the field of 850 hPa T' by subtracting the 1979–2016 linear trend at each grid point (the detrended field is only used for the selection of the temperature extreme events in this study). The detrended 850 hPa T' is averaged over the region [34–44°N , 18–28°E] (Fig. 4.1) with a cosine latitude weighting. Days with an area-averaged T' greater (lower) than the 95^{th} (5^{th}) percentile of the respective season (DJF, MAM, JJA, SON) are regarded hot (cold) extremes. Episodes of 1–2 extreme days constitute a *short-lived* temperature

extreme event. Episodes of 3 or more consecutive extreme days constitute a *persistent* temperature extreme event. In few cases where the onset of two subsequent extreme events occurred within 4 days or less, we did not regard the second one to be distinct and independent from the first one and we discard it from the event list.

Due to the limited size of the event samples, composite fields in the following analyses are computed using the mean of the interquartile range of the sample, which restricts the effect of outliers and renders the statistics more robust. In addition, the statistical significance of the v', Z' and T' composites is assessed with a Monte Carlo technique (e.g. Martius *et al.* 2008). Namely, the values at each grid point are deemed significant at the α=0.10 level, if they belong to either 5% tail of a distribution created by reconstructing the composites 300 times using random selections of dates.

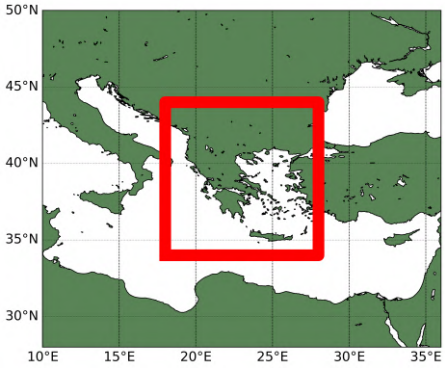

Fig. 4.1: *Region of T' averaging in the extremes selection.*

4.3 Results

The resulting number and mean duration of distinct hot and cold extremes in all four seasons is shown in Table 1. The winter season is characterized by the shortest duration in extremes (1.8 days for hot and 2.0 for cold). The percentage of persistent extremes maximizes in summer for hot extremes (26/69, with 4.5 days mean duration) and spring for cold extremes (30/62, with 4.4 days mean duration). Finally, with the exception of spring, hot extremes in all seasons tend to last longer than cold extremes.

Table 4.1: *Number and mean duration (in days) of hot and cold extremes. Values in the parenthesis correspond to persistent temperature extremes.*

	Hot extremes		Cold extremes	
Season	Events	Duration	Events	Duration
DJF	95 (16)	1.8 (4.1)	86 (21)	2.0 (3.7)
MAM	82 (26)	2.1 (3.8)	62 (30)	2.8 (4.4)
JJA	69 (26)	2.5 (4.5)	76 (25)	2.3 (4.0)
SON	70 (24)	2.5 (4.4)	80 (26)	2.2 (3.6)

Composites of 850 hPa T', 500 hPa Z' and 300 hPa v' during JJA hot extremes (69 distinct events) are shown in Fig. 2a,c. In the T' composite over the onset days (Fig. 2a), a dipole structure is evident with warm anomalies maximized over SE Europe and cold anomalies over Western Europe, both having a SW–NE orientation. In Fig. 2c, v' and Z' composites are shown for selected days before and after the onset of the events, revealing a distinct pattern of RWP propagation. More specifically, a trough–ridge sequence moves eastward at slow phase velocities, while the encompassing RWP as a whole propagates faster indicating the transfer of energy and generation

of new disturbances downstream. Eventually, the upper-tropospheric flow over SE Europe is deflected northward forming a ridge with anticyclonic vorticity. As a consequence, we get a favorable environment for extreme temperatures since warm and dry air is advected from N. Africa. Previous studies (e.g. Founda and Giannakopoulos 2009) have shown that this works in conjuction with adiabatic compressional heating due to enhanced subsidence (which during summer months is anyway present as a climatic feature of the region) and anomalous radiative forcing to result in extreme temperatures.

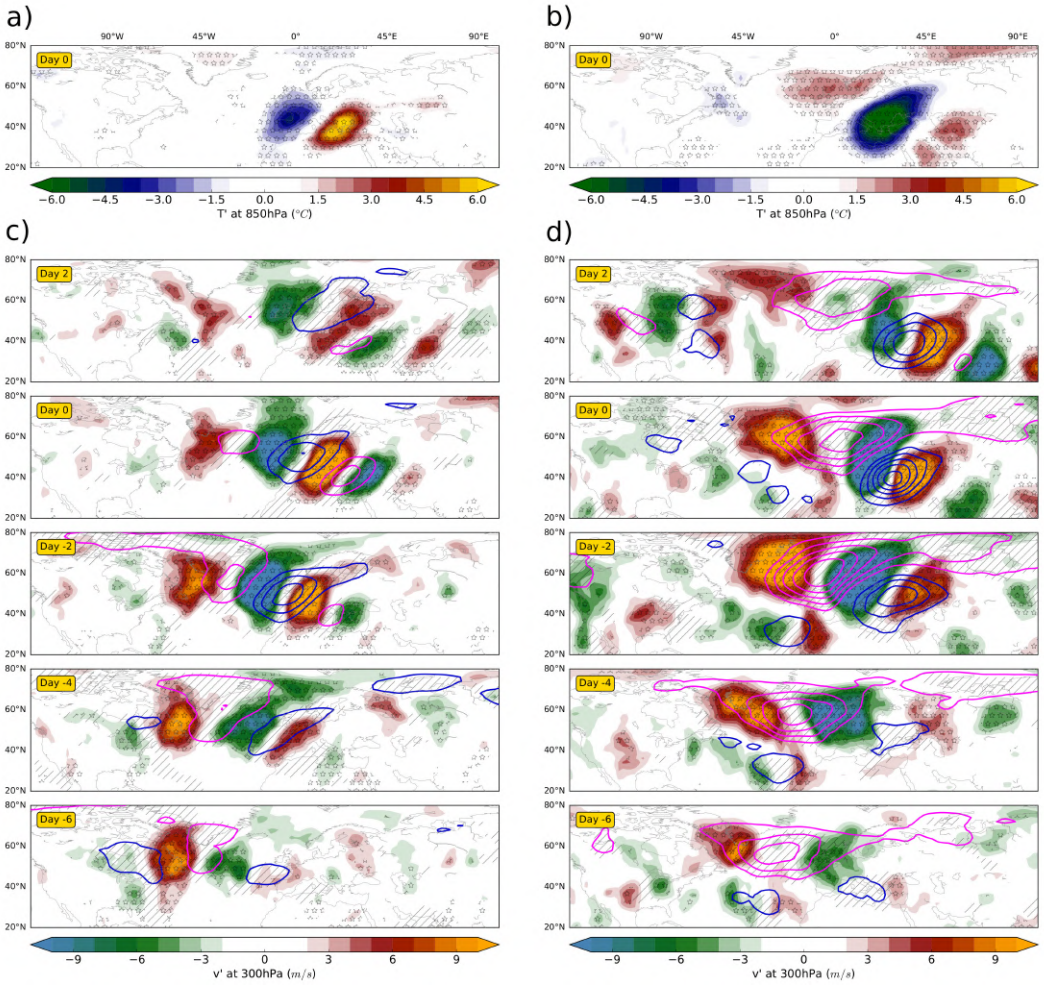

Fig. 4.2: *a) Composite of 850 hPa T' (color shading) at the onset of JJA hot extremes. Stars denote statistically significant values of T' at α=0.10. b) Same as a) but for DJF cold extremes. c) Evolution of 300 hPa v' (color shading) and 500 hPa Z' (blue/magenta contours indicate negative/positive anomalies at ±3, ±6, ±9, ... gpdam) composites from Day –6 to Day 2 of JJA hot extremes. Stars (hatching) denote statistically significant values of v' (Z') at α=0.10. d) Same as c) but for DJF cold extremes.*

Apart from the opposite sign in the anomaly composites during DJF cold extremes (86 distinct events), we get a rather different circulation pattern evolution (Fig. 2b,d). The areas affected by cold temperatures have a higher spatial extent and

are surrounded by smaller centres of positive T' (Fig. 2b). A distinct blocking anticyclone is a prevalent feature of the North Atlantic circulation several days before the onset of the events; a typical flow regime for cold extremes in Europe (Sillmann and Croci-Maspoli 2009). At Day –2, an elongated trough has formed at the eastern flank of the block, transporting continental cold air masses from the northeast towards SE Europe. This pattern persists and two days later we have the onset of the cold extreme. Afterwards, the North Atlantic block starts to weaken and the RWP propagates into Asia arching toward the Tropics.

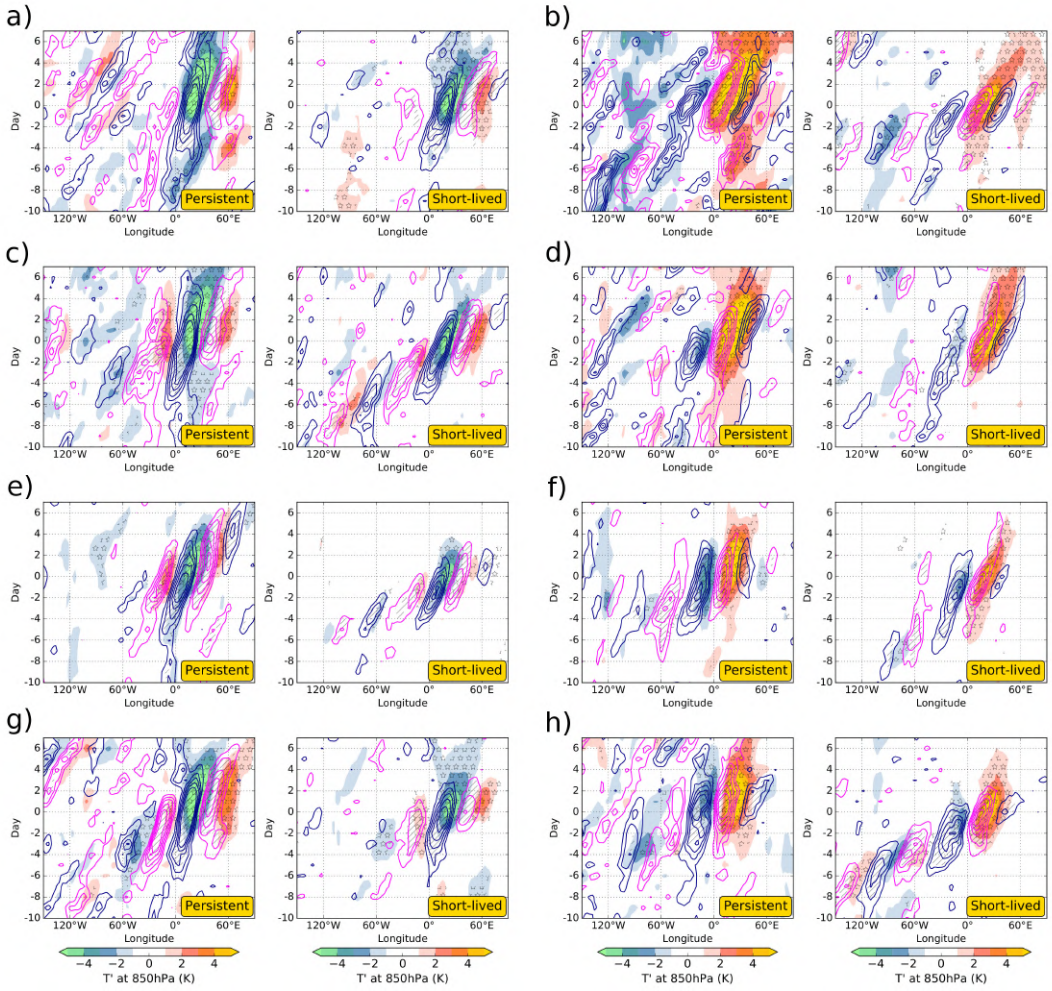

Fig. 4.3: *a) Hovmöller composites of 850 hPa T' (color shading) and 300 hPa v' (blue/magenta contours indicate negative/positive anomalies at ±3, ±5, ±7, ... m/s) during DJF persistent (left) and short-term (right) cold extremes. Stars (hatching) denote statistically significant values of T' (v') at α=0.10. b) Same as a) but for hot extremes. c), d) Same for MAM. e), f) Same for JJA. g), h) Same for SON.*

We now consider short-lived and persistent temperature extremes separately, in order to explore differences in the typical circulation associated with them. To this end, we show composites of 850 hPa T' and 300 hPa v' compressed in Hovmöller diagrams for all seasons and both types of extremes (Fig. 4.3). T' has been averaged over the 34–44°N latitudinal band, while v' has been averaged over the wider 34–64°N latitudinal

band, in order to capture the main features of the large-scale midlatitude flow. In composites of persistent extremes our sample size decreases considerably (Table 1) at the expense of statistical significance, but indications of qualitative differences from short-lived extremes can still arise. Some key observations on the various extreme types include:

(i) Patterns of T' for the persistent extremes appear more elongated (in the time direction, as expected), wider (spanning more longitudes) and more stagnant (forming an almost right angle with the longitudes axis) than the ones for short-lived extremes.

(ii) In many cases (e.g. MAM short-lived cold extremes, DJF persistent hot extremes, SON short-lived hot extremes), the succession of positive (southerly) and negative (northerly) v' values indicates a far-upstream RWP signal several days before the extreme onset. In the cases where an RWP is not traceable several days in advance, either an organized group of Rossby wave activity was not present (e.g. block cases in DJF cold extremes) or the RWPs evolve in varying pathways leading to partial destructive interference and a reduced wave signal from the sample.

(iii) As is well known, the Hovmöller diagram can provide an estimation of the phase and the group velocity associated with an RWP (Fragkoulidis *et al.* 2018). In all cases, the group velocity is greater than the phase velocity of individual troughs–ridges. This so-called downstream development phenomenon is particularly pronounced for e.g. DJF short-lived hot extremes and JJA short-lived cold extremes and less so for e.g. JJA short-lived hot extremes and MAM short-lived extremes.

(iv) Persistent extremes are associated with quasi-stationary v' patterns, whereas higher phase velocities are observed in short-lived extremes. This manifests the decisive role of upper-tropospheric circulation in the duration of temperature extremes (Kyselý 2008).

(v) The zonal gradient of v' above SE Europe is greater for cold than hot extremes (also evident in Fig. 4.2). Associated with that, hot extremes tend to occur close to the centre of the overlying ridge, while cold extremes occur closer to the area of negative v' values (northerlies) of the trough aloft.

Finally, it's worth verifying the performance of deterministic forecasts of these temperature extremes. The availability of a 38-year dataset with forecasts produced with the same model (section 4.2) allows us to have a consistent comparison with the corresponding reanalysis of selected events. Our verification involves forecasts issued 3 and 5 days prior to DJF cold and JJA hot persistent extremes (21 and 26 events respectively). Fig. 4.4 shows Hovmöller composites of T' and v' (as in Fig. 4.3) for these forecasts. These are complemented by the forecast-minus-reanalysis Hovmöller composites, that serve to reveal systematic errors in the prediction of persistent extremes.

Forecasts issued 3 and 5 days prior to JJA persistent hot extremes show an underestimation of T' above our region of interest (18–28°E) and an overestimation

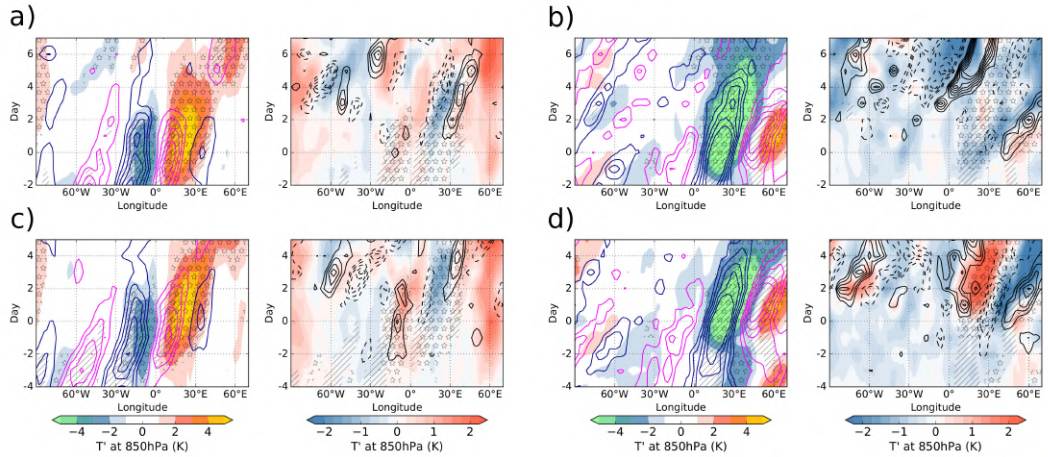

Fig. 4.4: *a) Left: Hovmöller composites of 850 hPa T' (color shading) and 300 hPa v' forecasts (blue/magenta contours indicate negative/positive anomalies at ±3, ±5, ±7, ... m/s), issued 3 days prior to JJA persistent hot extremes. Stars (hatching) denote statistically significant values of T' (v') at α=0.10. Right: Deviation of the forecasted 850 hPa T' (color shading) and 300 hPa v' (solid/dashed contours indicate positive/negative anomalies at ±2, ±3, ±4, ... m/s) from the respective reanalysis fields (Fig. 3f left). Statistically significant deviations are assumed where both the forecast and reanalysis fields are significant at α=0.10. b) Same as a) but for DJF persistent cold extremes. c),d) Same as a),b) but for forecasts issued 5 days prior to the extremes.*

to the east and west of that. This pattern can arise due to positional (some extremes are predicted to occur to the east and others to the west of the eventually affected region) and/or magnitude errors. Forecasts issued 3 days prior to DJF persistent cold extremes reveal an overestimation in both magnitude and duration. In 5-day forecasts, an eastward shift of the cold anomalies is predicted. In contrast to hot extremes, now an error is also evident in the v' field with an eastward shift of the trough that can in principle explain the T' error pattern.

4.4 Conclusions

In this study, we investigated the synoptic circulation associated with the most pronounced temperature extremes that affected SE Europe in the last 38 years. Although the amount of such high-impact events is limited and robust results are not feasible, qualitative differences and similarities between the synoptic circulation imprints of hot and cold extremes across all seasons were inferred. In addition, distinguishing between short-lived and persistent extremes revealed differences in the spatiotemporal evolution of the upper-tropospheric flow. Far-upstream precursors were evident for several types of temperature extremes, indicating a recurrent in-phase RWP propagation, while in other cases the less clear signal in the days preceding the extremes suggests a larger variability with no preferential RWP pathway.

Future studies on medium-range forecasts of temperature extremes should investigate further the role of upper-tropospheric dynamical features and how model

limitations lead to systematic errors in the Rossby wave structure (Gray *et al.* 2014). Moreover, an improved understanding on the interplay between synoptic circulation patterns, radiative transfer and boundary layer processes will help in interpreting the observed increase in frequency and severity of persistent temperature extremes (Kyselý 2008).

Acknowledgements

We thank the ECMWF for providing access to the data used in this study. The research leading to these results has been done within the Transregional Collaborative Research Center SFB/TRR 165 "Waves to Weather" funded by the German Research Foundation (DFG).

Chapter 5

Local Rossby wave amplitude, phase velocity, and group velocity: Seasonal variability and their role in temperature extremes

G. Fragkoulidis[a*] and V. Wirth[a]

[a] *Institute for Atmospheric Physics, Johannes Gutenberg University, Mainz, Germany*
[*] *corresponding author e-mail: gfragkou@uni-mainz.de*

This chapter is equivalent to the article of homonymous title by the authors listed above that has been submitted to the Journal of Climate and is currently under review (Manuscript No.: JCLI-D-19-0377). Copyright in this work may be transferred without further notice. The manuscript is integrated with minor changes into the dissertation and the section and figure numbers are adjusted accordingly. The references are listed in the unified bibliography at the end of the dissertation.

Abstract

Transient Rossby wave packets (RWPs) are a prominent feature of the large-scale upper-tropospheric flow at the mid-latitudes. Their demonstrated role in the occurrence of weather extremes prompts the investigation of their spatiotemporal evolution and characteristic properties. The present work proposes a novel method for the diagnosis of horizontal Rossby wave phase and group velocity, locally in space and time, by employing the analytic signal of upper-tropospheric meridional wind velocity and RWP amplitude respectively. The new diagnostics are first applied in illustrative examples from a barotropic model simulation and real data. Using ERA5 reanalysis data for the time period 1979–2018, we then report on the main seasonal and inter-regional variability aspects of RWP amplitude, zonal phase velocity as well as zonal and meridional group velocity. Apparent differences and similarities in these respects between

the Northern and Southern Hemispheres are discussed. Furthermore, the role of RWP amplitude and zonal phase velocity in the occurrence and duration of Central European temperature extremes is investigated in a quantitative fashion for the entire length of the reanalysis dataset. It is found that an enhanced RWP amplitude is a prerequisite for the occurrence of both hot and cold extremes, but for the events to persist longer a below-normal phase velocity in the trough–ridge pattern aloft is essential. Overall, the proposed diagnostics offer insight into local properties of the RWP evolution and allow the systematic evaluation of their implications at low computational demands.

5.1 Introduction

Rossby waves are a dominant feature of the mid-latitude upper-tropospheric circulation at synoptic to planetary scales (Rossby 1940; Haurwitz 1940). Owing their existence to the rotation and the spherical shape of the Earth, they take the form of large-scale meanders in the westerly winds (Rhines 2015). On the weather time scale, Rossby wave activity is typically not circumglobal, but instead modulated in longitude and organized in the so-called Rossby wave packets (RWPs; e.g., Lee and Held 1993; Chang 1993). Although theoretical arguments for the evolution of Rossby waves in idealized setups had already been put forward in the middle of the twentieth century (Dickinson 1978 and references therein), their actual behavior and role in the atmosphere started being investigated in recent decades, facilitated by the increasing data availability and advances in computer performance (see Wirth *et al.* 2018 for a review of recent developments). In this regard, recent studies have examined the role of the RWPs evolution in: storm track activity (Hakim 2003; Chang *et al.* 2002; Ahmadi-Givi *et al.* 2014), the occurrence of weather extremes (Feldstein and Dayan 2008; Wirth and Eichhorn 2014; O'Brien and Reeder 2017; Fragkoulidis *et al.* 2018), and predictability (Grazzini and Vitart 2015; Quinting and Vitart 2019; Baumgart *et al.* 2019).

In parallel, ongoing efforts in improving the diagnostic methods of RWPs aim to shed more light on the above considerations. Hovmöller diagrams have been used for the investigation of RWP progression in longitude and time (Hovmöller 1949; Glatt *et al.* 2011; Röthlisberger *et al.* 2019). Computing the envelope of the meridional wind has allowed the development of RWP tracking algorithms and climatological assessments of their preferred regions of formation and decay (Souders *et al.* 2014b; Glatt and Wirth 2014). Furthermore, the concepts of wave energy flux and wave activity flux have provided insight into the horizontal propagation of RWPs (Chang and Orlanski 1994; Takaya and Nakamura 2001; Wolf and Wirth 2017). As a final example, the potential vorticity framework has been employed for the analysis of downstream development, baroclinic amplification and other dynamical processes that affect the lifetime of RWPs (Teubler and Riemer 2016).

Two important aspects for the Rossby wave evolution, which so far lack a local diagnosis in space and time, are the phase and group velocity. The phase velocity reflects the propagation speed of individual troughs and ridges within a RWP and can thus be critical for the persistence of extreme weather (Röthlisberger *et al.* 2019). When it comes to small wavenumbers (1 to 3), the zonal component of the phase velocity can also affect wave propagation into the stratosphere and the evolution of

sudden stratospheric warming events (Domeisen *et al.* 2018). Group velocity, on the other hand, indicates how fast the wave packet propagates as a whole and reflects the rate at which energy is transferred by the Rossby waves (e.g., Pedlosky 2003; Cai and Huang 2013).

Previous diagnostic methods regarding these two aspects have been non-local in space or time and are thus not suited to follow the evolution of a RWP at high spatial and temporal resolution. For example, Blackmon *et al.* (1984) proposed a method to calculate phase velocity based on lag-correlation maps, which was later also used for the diagnosis of group velocity (Berbery *et al.* 1996; Chang and Yu 1999). This method gives a measure of phase and group velocity that is local in space, but not local in time; the computation for a given grid point involves the evolution of the meridional wind (or envelope) field over multiple days, so that the lag-correlation maxima can be traced at the neighboring grid points. In other studies, Fourier analysis has been used for the diagnosis of phase velocity for given wavenumbers (e.g., Coumou *et al.* 2014). In this case, the resulting field can be instantaneous, but there is no longitudinal information. Obviously, estimates of the zonal phase and group velocity can also be extracted from Hovmöller diagrams (Joung and Hitchman 1982; Lee and Held 1993), but they are sensitive to the way the diagram is constructed and limited to a single value per eddy and RWP at each time step.

In this study, we employ a method that was originally developed by Gabor (1946) in view of analyzing the instantaneous frequency in time-varying signals. The method involves the *analytic signal*, a complex-valued representation of a real signal that can uniquely define its instantaneous amplitude and phase (Huang *et al.* 2009). Computing the analytic signal of meridional wind along latitude circles will allow us to identify the local phase within RWPs, which can then be used to diagnose the zonal component of the local phase velocity. In a similar way, we will propose an object-based approach for the diagnosis of the zonal and meridional group velocity using the RWP amplitude field. These local diagnostics will allow us to investigate the seasonal patterns and variability of important RWP properties, as well as their role in temperature extremes of a specific region.

In light of these research questions and objectives, this study is organized as follows. After a brief description on the data used (section 5.2), we present the methodology for the diagnosis of the local and instantaneous phase and group velocity in section 5.3. Exemplary applications to barotropic model and reanalysis data provide insight into these novel diagnostics. In section 5.4 we report on the seasonal and inter-regional variability of the diagnosed variables, while in section 5.5 we investigate the role of RWP phase velocity and amplitude in Central European temperature extremes. Finally, our results are summarized in section 5.6, along with a discussion of their implications and limitations. Computational details and additional analyses that support the interpretation of the presented methods and results are included in the Supplemental Material.

5.2 Data

In this study we use ERA5 reanalysis data [Copernicus Climate Change Service (C3S) 2017] for the period from January 1979 to December 2018. In particular, zonal and meridional wind (u and v) at 300 hPa, geopotential height (Z) at 500 hPa and temperature (T) at 850 hPa have been retrieved at a 6-hourly temporal resolution (daily at 0000, 0600, 1200 and 1800 UTC) on a grid of 2° ×2° horizontal resolution. Furthermore, in section 5.3 the methodology steps of the presented diagnostics are illustrated using output from a barotropic model simulation with 2° ×2° horizontal resolution and a 6-hourly temporal resolution (Ghinassi *et al.* 2018).

In view of the diagnosis of local RWP properties and their relation to temperature extremes, the retrieved reanalysis fields are pre-processed as follows:

(i) The anomalous components of v, Z and T, denoted by v', Z' and T' respectively, are computed by removing at each grid point (λ: longitude, ϕ: latitude) and time instance t the corresponding value of a smooth annual cycle:

$$\psi'(\lambda, \phi, t) = \psi(\lambda, \phi, t) - \overline{\psi}(\lambda, \phi, t_d) \tag{5.1}$$

where ψ represents the variable (v, Z or T), $\overline{\psi}$ represents the annual cycle, and t_d denotes a particular time step in the year (e.g., 1200 UTC 15 February). The annual cycle is obtained by first averaging the variable for each t_d over the 40 years available (1979–2018), followed by a Fourier series decomposition and restriction to frequencies 0–4 year^{-1}.

(ii) The meridional wind anomaly, v', is zonally filtered as described in Fragkoulidis *et al.* (2018). Essentially, from the v' full field spectrum we keep wavelengths 2,000–10,000 km, which roughly corresponds to zonal wavenumbers 3–15 at 40°N . Discontinuities that may arise from this zonal filtering are then minimized by convolving a Hann window (Harris 1978) of 7° length at half maximum in the meridional direction. For consistency, this spatial filtering is also applied to the barotropic model data.

(iii) Finally, the v' field is temporally smoothed with a 24-hour moving average. Achieving a less jumpy transition from one time step to the next ensures slightly smoother patterns of phase and group velocity (see also discussion in sections 5.3 and 5.6).

The ensuing smoothing of the meridional wind field in the last two steps is weak enough to leave the local RWP characteristics and their transient evolution unaffected, but at the same time strong enough to avoid spurious values from fine-scale features.

5.3 Diagnosis of local phase and group velocity

5.3.1 Analytic signal and local phase

Given a real signal, its corresponding analytic signal is given by suppressing the negative half of its frequency spectrum and multiplying the amplitudes of the positive

frequencies by two (Gabor 1946). As mentioned in the introduction, our goal here is to compute the analytic signal of the upper-tropospheric (300 hPa) meridional wind anomaly along latitude circles in order to detect the Rossby wave amplitude and phase at each longitude. The evolution of troughs and ridges is clearly reflected on this field, which makes it well-suited for the investigation of RWP properties and evolution (e.g., Chang 1993).

In the following, the meridional wind anomaly along a latitude circle of even length L is written as the sequence v'_ℓ, where $\ell = 0, 1, ..., L-1$ denotes the grid point that is located at longitude $\lambda = 2\pi\ell/L$ (with $0 < \lambda \leq 2\pi$). Following (Marple 1999), we have that the analytic signal of v'_ℓ is given by:

$$A_{v'_\ell} = \frac{1}{L} \sum_{m=0}^{L-1} \tilde{A}_m e^{2im\pi\ell/L} \ , \tag{5.2}$$

with:

$$\tilde{A}_m = \begin{cases} \tilde{v'}_m & \text{for} \quad m = 0, \ L/2 \ , \\ 2\tilde{v'}_m & \text{for} \quad 1 \leq m \leq L/2 - 1 \ , \\ 0 & \text{for} \quad L/2 + 1 \leq m \leq L - 1 \ , \end{cases} \tag{5.3}$$

where m is the spatial frequency (wavenumber) and $\tilde{v'}_m$ is the discrete Fourier transform of v'_ℓ:

$$\tilde{v'}_m = \frac{1}{L} \sum_{\ell=0}^{L-1} v'_\ell e^{-2im\pi\ell/L} \tag{5.4}$$

By suppressing the negative half of the v'_m frequency spectrum (which is redundant for a real signal, since its spectrum is conjugate symmetric: $\tilde{v'}_{+m} = \tilde{v'}^*_{-m}$), $A_{v'_\ell}$ becomes a complex function. Its real part, $Re[A_{v'_\ell}]$, corresponds to v'_ℓ, while its imaginary part, $Im[A_{v'_\ell}]$, corresponds to the Hilbert transform of v'_ℓ (Gabor 1946; Cohen 1995) *.

Given the complex representation of v'_ℓ ($A_{v'_\ell}$) it is now possible to obtain the local amplitude and phase of wave-like fluctuations in longitude. Namely, when $A_{v'_\ell}$ is expressed in polar form,

$$A_{v'_\ell} = |A_{v'_\ell}| e^{iArg\{A_{v'_\ell}\}} = E_\ell e^{i\Phi_{v'_\ell}} \ , \tag{5.5}$$

it can be seen that $E_\ell = |A_{v'_\ell}|$ is the envelope function (local amplitude) and:

$$\Phi_{v'_\ell} = tan^{-1}\Big(\frac{Im[A_{v'_\ell}]}{Re[A_{v'_\ell}]}\Big) \tag{5.6}$$

is the local phase (e.g. Cohen 1995) †. This formulation for the local phase was recently used for the extraction of the local wavenumber in gravity waves (Schoon and Zülicke 2018). A similar expression for the local RWP phase appeared in the past (eq. 32

*Instead of using (5.2), another way to get the analytic signal is by forming $A_{v'_\ell} = v'_\ell + i\ \mathcal{H}[v'_\ell]$ where the Hilbert transform $\mathcal{H}$ is computed as: $\mathcal{H}[v'_\ell] = \mathcal{F}^{-1}\{-i\ sgn(m)\tilde{v}'_m\}$ (e.g., Chaudhury and Unser 2009). Here $\mathcal{F}^{-1}$ denotes the inverse discrete Fourier transform and sgn the sign function.

†The function $atan2$ (two-argument variant of $arctangent$) is used to calculate the principal value of the argument ($Arg\{A_{v'_\ell}\}$), because it accounts for angles in all four quadrants.

in Hayashi 1982), but to the best of our knowledge it has not been exploited further since then. Several studies have focused on the envelope (E) as a measure of the local RWP amplitude (e.g., Zimin *et al.* 2003; Glatt and Wirth 2014; Souders *et al.* 2014a; Wolf and Wirth 2015; Fragkoulidis *et al.* 2018). In this study, the local phase (Φ) will constitute the key element for the diagnosis of Rossby wave phase and group velocity locally.

5.3.2 Local Rossby wave phase velocity

The phase at time t and location x for a wave of angular frequency ω and zonal angular wavenumber k that propagates at a certain altitude along a certain latitude is given by:

$$\Phi = kx - \omega t + \Phi_0 \ , \tag{5.7}$$

where $x = acos\phi\lambda$ and Φ_0 is a constant offset (a denotes the Earth radius). The units of ω and k are $rad \cdot s^{-1}$ and $rad \cdot m^{-1}$, respectively. Phase velocity corresponds to the propagation velocity of a point of constant phase and can be defined as the ratio of angular frequency (ω) to angular wavenumber (k). In the following, phase velocity will always refer to a velocity relative to the surface of the Earth. Therefore, after computing the local phase, $\Phi_{v'_\ell}$, by applying (5.6) at each latitude circle, the local phase velocity, c_p, is given by:

$$c_p = \frac{\omega_{v'_\ell}}{k_{v'_\ell}} \tag{5.8}$$

$$\text{where:} \quad \omega_{v'_\ell} = -\frac{\partial \Phi_{v'_\ell}}{\partial t}, \tag{5.9}$$

$$\text{and:} \quad k_{v'_\ell} = \frac{1}{acos\phi}\frac{\partial \Phi_{v'_\ell}}{\partial \lambda} \tag{5.10}$$

The derivatives in longitude and time are calculated using centered differences (see also section 5.7.2 in the Supplemental Material) and positive (negative) c_p values correspond to eastward (westward) propagation relative to the ground. The above calculations are repeated for every latitude, so that we get the two-dimensional c_p field. Since troughs and ridges move predominantly in the zonal direction, we focus attention on zonal phase velocity only.

The calculation of c_p is omitted when the RWP amplitude does not exceed a certain threshold, E_0. In particular, if δt and $\delta\lambda$ are the time step and longitudinal interval of the data respectively, c_p at (λ, ϕ, t) is only computed when $E \geq E_0$ at (λ, ϕ, t), $(\lambda, \phi, t + \delta t)$, $(\lambda, \phi, t - \delta t)$, $(\lambda + \delta\lambda, \phi, t)$, and $(\lambda - \delta\lambda, \phi, t)$. This is done, because areas of weak E values associated with the incoherent evolution of small-scale features or the often diffusive edges of RWPs may result in spurious c_p values. The notion of phase propagation is anyway ambiguous when there is no well-defined wave in the flow. For the barotropic model simulation, where the two RWPs have a weaker amplitude than a typical real case scenario, we set this threshold to 3 ms^{-1}, as it outlines the main body of the two RWPs (Fig. 5.1). For the reanalysis data we choose a threshold of 15 ms^{-1}, which is similar to the RWP object identification threshold of 14 ms^{-1} in the study of Souders *et al.* (2014a). This threshold remains fixed for all

seasons. Since one of our main goals is to investigate the seasonal variability of the local RWP properties, we do not want seasonality in the threshold to have an effect. Nevertheless, the results in sections 5.4 and 5.5 are not sensitive to the exact value of E_0 (see also discussion in section 5.6).

An implicit assumption of our methodology is that "locally" the underlying wave signal corresponds to an almost plane wave of a certain wavenumber [‡], since otherwise the notions of local wavenumber and phase velocity lose their physical meaning. More specifically, we assume that the wave signal is symmetric with respect to the "locally" zero mean and it has the same number of zero-crossings and local extrema (Huang *et al.* 1998). These conditions are illustrated and discussed in sections 5.7.1 and 5.7.3 of the Supplemental Material. In the areas of RWPs where we restrict our calculations to, the "local" succession of southerlies and northerlies most of the times satisfies these criteria. The pre-processing steps of the meridional wind field (section 5.2) were also intended to work in this direction, without affecting the local RWP characteristics.

5.3.3 Local Rossby wave group velocity

The propagation of the wave packet as a whole is less confined in the zonal direction and can attain discernible meridional components. This calls for a diagnosis of both the zonal and meridional components of the group velocity (vector) field: $\boldsymbol{c_g} = (c_{gx}, c_{gy})$. The two components can be inferred from the evolution of the envelope field, E, associated with the RWP that embodies the troughs and ridges. In this regard, our proposed methodology for the local group velocity diagnosis shares the basic principle with the one of the local phase velocity, using the E function instead of v. Again, group velocity will always refer to a velocity relative to the surface of the Earth.

As discussed before, certain conditions have to be met in order to get physically meaningful information of the local phase, angular wavenumber, and angular frequency of a wave signal. The main difficulty with group velocity arises from the fact that E is an always positive quantity, unlike v and v' that naturally fluctuate between northerlies and southerlies. Simply removing the global zonal mean of E would potentially lead to erroneous phase diagnosis in cases when two RWPs of different amplitude and/or length evolve at the same latitude circle (see Fig. 5.11 in the Supplemental Material for such an example).

Our way forward is an object-based diagnosis of the local E phase, where each individual RWP is treated separately. At first, E is zonally filtered as v' (section 5.2), but at double wavelength limits: 4,000–20,000 km. This smoothing minimizes the effect of possible wiggles in the envelope function of a single RWP, that may locally lead to an undesirable increase in the wavenumber of the E function and, as a result, a decrease in the zonal group velocity (see the fifth step in the procedure below). Given the smooth E field, the procedure for the diagnosis of local group velocity in the zonal direction, c_{gx}, at time t_0 along a latitude circle involves the following steps:

(i) Grid points that exceed E_0 are regarded as part of a RWP. If the length, $\mathcal{L}$, of a detected RWP object exceeds $\mathcal{L}_0 = 20°$ in longitude, we compute its "envelope

[‡]In section 5.7.3 of the Supplemental Material, an example of wavelet transform along a latitude circle reveals how v'_ℓ is generally composed by a spectrum of wavenumbers at each longitude.

anomaly" signal, E'_ℓ. This is done, by subtracting at each grid point ℓ that it spans the mean envelope over these grid points:

$$E'_\ell = E_\ell - \frac{\delta\lambda}{\mathcal{L}} \sum_{\ell=\ell_1}^{\ell_2} E_\ell \quad \text{for} \quad \ell_1 \leq \ell \leq \ell_2 \,, \tag{5.11}$$

where ℓ_1 and ℓ_2 are the first and final grid points that the object spans. At these grid points, E'_ℓ now corresponds to a signal that is symmetric around zero with two zero-crossings and two local extrema [§] (i.e., a wavenumber 1 signal with a local maximum at the middle and a local minimum at the boundary; see also Figs. 5.1 and 5.12 for a visualization). The same is done for all other detected RWPs along this latitude circle. The reason why we restrict to lengths above $\mathcal{L}_0$ is to avoid dealing with structures that are too small and perhaps noisy to be regarded RWPs.

(ii) For each detected RWP of length $\mathcal{L}$ we seek the location of the corresponding E_ℓ segments at the preceding and succeeding time steps $(t_0 - \delta t,\, t_0 + \delta t)$, that will be used for the angular frequency calculation. These segments need to be of length $\mathcal{L}$ as well, and are chosen to span the longitudinal ranges that maximize the sum of E_ℓ, within a search area of $\mathcal{L} + 2\mathcal{L}_0$ degrees longitude. This search area covers the original RWP object (at t_0) plus $\mathcal{L}_0$ degrees to its left and right. E'_ℓ at this segment is then computed at $t_0 - \delta t$ and $t_0 + \delta t$ by subtracting the respective object zonal mean. The requirement to have equal-length segments of E'_ℓ in the three consecutive instances of the RWP object is discussed in section 5.7.1 of the Supplemental Material. The periodicity of the domain is properly accounted for in these first two steps, so that RWPs around the prime meridian (which in our case constitutes the grid boundary) are not treated as two distinct objects.

(iii) For each detected RWP object we compute the analytic signal, $A_{E'_\ell}$, and local phase, $\Phi_{E'_\ell}$, at the three consecutive $t_0 - \delta t$, t, and $t_0 + \delta t$, by applying (5.2) and (5.6) respectively on the E'_ℓ segment of the three time steps. Given the way these E'_ℓ segments were located, one can assume that they are close to periodic and edge effects are avoided in the discrete Fourier transform of (5.2).

(iv) The zonal angular frequency, $\omega_{E'_\ell}$, and angular wavenumber, $k_{E'_\ell}$, are calculated as in (5.9) and (5.10) respectively, at longitudes where $\Phi_{E'_\ell}$ is defined for the two points that are involved in the centered differences. That is, $k_{E'_\ell}$ is not computed at the two edges of the detected RWP object and $\omega_{E'_\ell}$ is not computed at longitudes that the RWP object does not occupy at either of the $t_0 - \delta t$ and $t_0 + \delta t$ time steps. The latter implies that the temporal resolution of the dataset has to be high enough, such that it allows some overlap of the RWP object at consecutive timesteps. The 6-hour resolution with a 24-hour moving average smoothing in our case ensure a large overlap for the typical group velocities.

(v) Finally, c_{gx} is computed as the ratio of $\omega_{E'_\ell}$ to $k_{E'_\ell}$ at longitudes where both of these have been computed.

[§]Despite the zonal filtering in E, such a behavior may be violated in real-case scenarios of RWPs with two local maxima. The group velocity calculation however will not necessarily fail in these cases.

These steps are then repeated for every latitude, so that we get the two-dimensional c_{gx} field. Positive (negative) c_{gx} values correspond to eastward (westward) group propagation relative to the ground.

When it comes to the meridional component of local group velocity, c_{gy}, the aforementioned steps are applied to the envelope function along meridians, E_n, in order to account for the evolution of RWPs in latitude. Here, the index n ($n = 0, 1, ..., N-1$) corresponds to the latitude, ϕ, across a meridian. The procedure is the same as for c_{gx}, except that we seek RWP objects in the meridional direction, the width $\mathcal{N}$ of which exceeds $\mathcal{N}_0$ =10° in latitude. The equivalent search area of step (ii) is then equal to $\mathcal{N} + 2\mathcal{N}_0$ degrees latitude (or less in case of a RWP close to the pole). The local phase, $\Phi_{E'_n}$, is computed for each detected RWP object, based on the envelope anomaly, E'_n, from the mean along the meridional segment it spans.

The meridional angular frequency, $\omega_{E'_n}$, is calculated as in (5.9) and the meridional angular wavenumber, $k_{E'_n}$, is calculated as: $a^{-1}\partial\Phi_{E'_n}/\partial\phi$, at latitudes where $\Phi_{E'_n}$ is defined for the two points that are involved in the centered differences. At latitudes where both are computed, c_{gy} is given by the ratio of $\omega_{E'_n}$ to $k_{E'_n}$. Positive (negative) c_{gy} values correspond to northward (southward) group propagation relative to the ground. Finally, the calculations are repeated for every longitude, so that we get the two-dimensional c_{gy} field.

Given that the evolution of RWPs is not always coherent, diagnosing their properties locally and instantaneously can at times lead to unphysical values. Even when restricting to grid points exceeding E_0, a noisy evolution of the v' and E fields can cause a jumpy behavior of $\Phi_{v'}$, $\Phi_{E'_\ell}$ and $\Phi_{E'_n}$ in space and/or time. In the extreme end of such cases, we mask the grid points where c_p, c_{gx} or c_{gy} exceed $|100|ms^{-1}$, in order to minimize the effect of such occurrences in the following analyses.

5.3.4 Exemplary cases

The aforementioned methodologies for the diagnosis of the c_p and $\boldsymbol{c_g}$ fields are first illustrated in the framework of a barotropic model simulation (Figs. 5.1 and 5.2), and then applied to a real case using reanalysis data (Fig. 5.3). In the barotropic simulation, we chose an idealized setup involving two RWPs of different carrier wavenumbers initialized upon a zonal background flow (more details in Ghinassi *et al.* 2018). The evolution of meridional wind (Figs. 5.1a-c) and the corresponding envelope (Figs. 5.1h–j) fields in a 12-hour segment of the idealized simulation depict the downstream propagation of the two wave packets.

On the left column of Fig. 5.1 we present the aforementioned steps for the diagnosis of the two-dimensional c_p field corresponding to the central time step t_0. In particular, Figs. 5.1d,e show v_ℓ and the corresponding Φ_{v_ℓ} (derived from eq. 5.6) along 40°N (as an example) at the three consecutive time steps. The phase function is "wrapped" since the *atan2* function gives values that are constrained to the $(-\pi, \pi]$ interval (eq. 5.6). Its value is positive (negative) when $Im[A_{v_\ell}]$ is positive (negative), which is the case in the areas of ridges (troughs) (see also Fig. 5.10). Due to this wrapping, caution is needed when computing the derivatives in longitude (angular wavenumber) and time (angular frequency). Our procedure in dealing with this issue is given in section 5.7.2 of the Supplemental Material. Based on (5.8), the c_p values that correspond to the

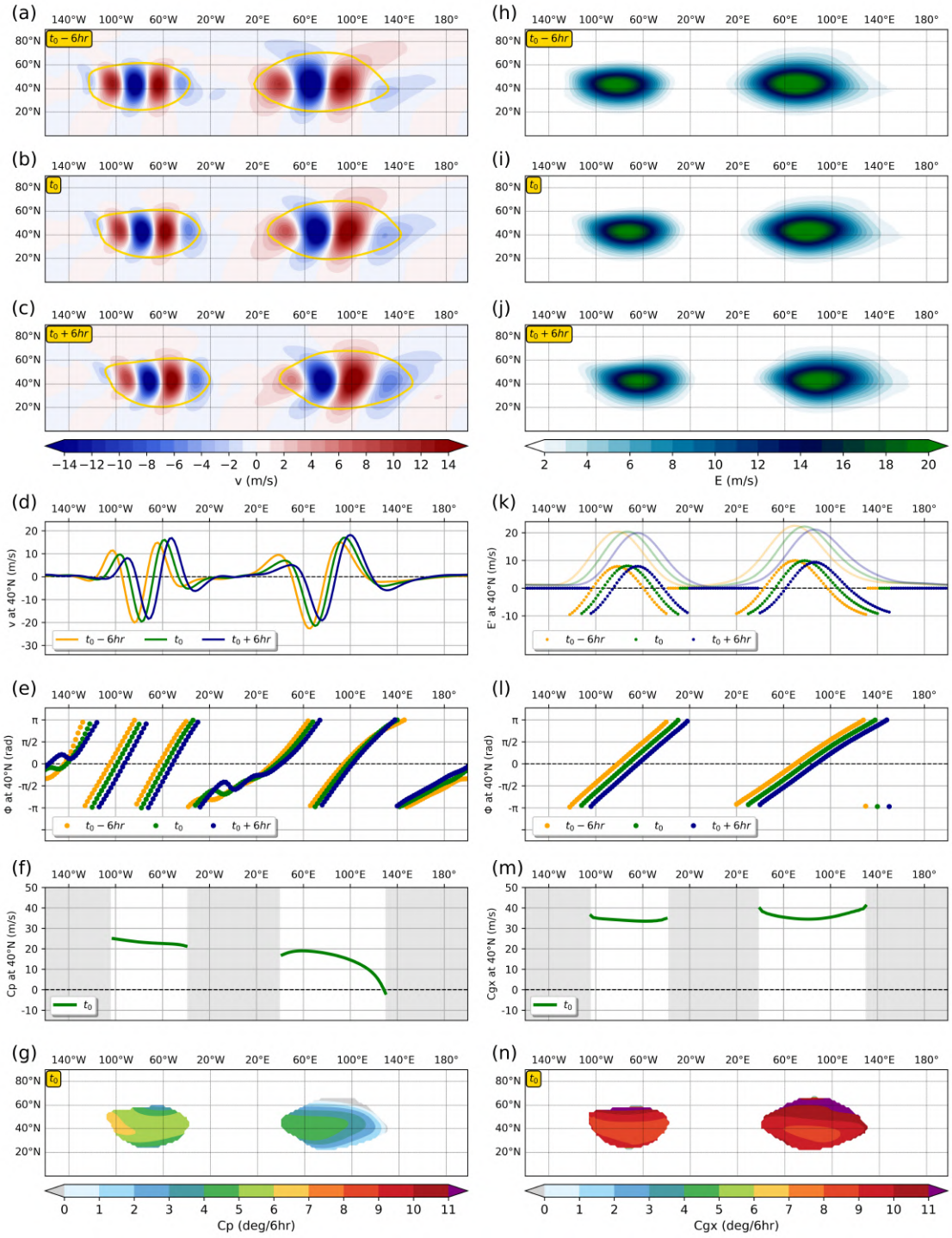

Fig. 5.1: *Illustration of the c_p and c_{gx} diagnosis in the barotropic model simulation. (a)–(c) υ at three consecutive 6-hourly time steps (color shading) and isoline of $E_0 = 3ms^{-1}$ (yellow contour). (d) υ_ℓ evolution at 40°N. (e) Φ_{υ_ℓ} evolution at 40°N. (f) c_p at 40°N. (g) Map of c_p at t_0. (h)–(j) E at three consecutive 6-hourly time steps. (k) E_ℓ (solid lines) and E'_ℓ (dotted lines) evolution at 40°N. (l) $\Phi_{E'_\ell}$ evolution at 40°N. (f) c_{gx} at 40°N. (g) Map of c_{gx} at t_0. Orange, green and blue colors in (d)–(f) and (k)–(m) correspond to the $t_0 - 6hr$, t_0 and $t_0 + 6hr$ time steps respectively (as indicated in the legends). Gray shading in (f) and (m) indicates longitudes where c_p and c_{gx} are not defined.*

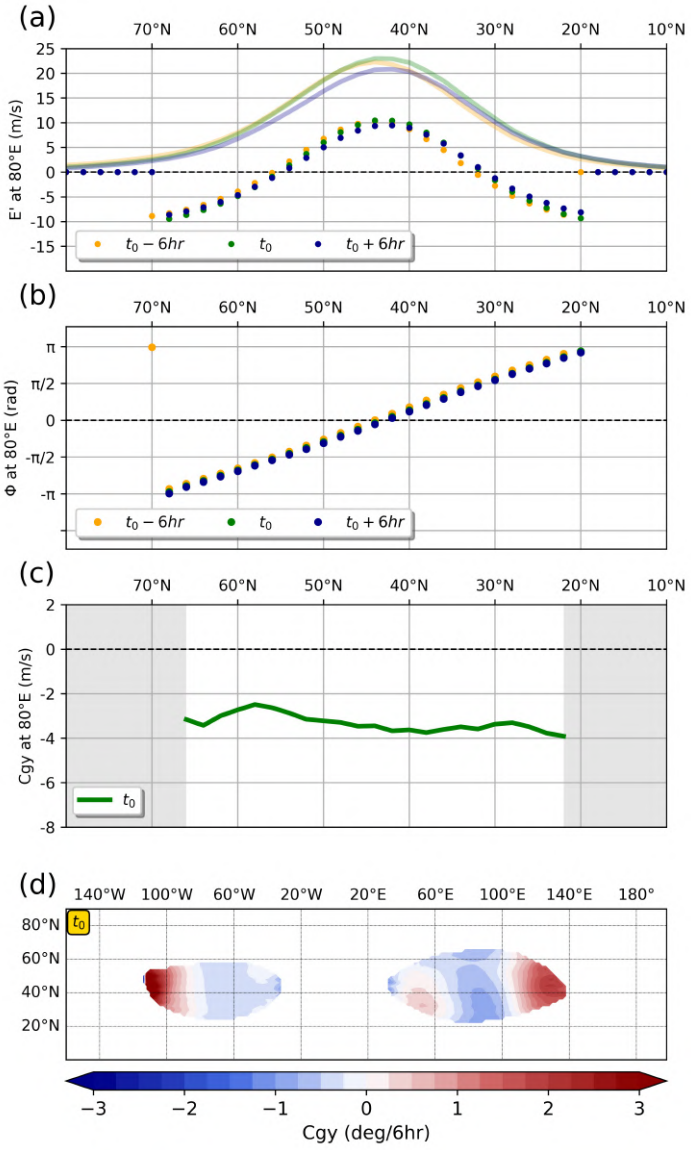

Fig. 5.2: *Illustration of the c_{gy} diagnosis in the barotropic model simulation. (a) E_n (solid lines) and E'_n (dotted lines) at 80°E for the three consecutive 6-hourly time steps. (b) $\Phi_{E'_n}$ evolution at 80°E. (c) c_{gy} at 80°E. (d) Map of c_{gy} at t_0. Orange, green and blue colors in (a)–(c) correspond to the $t_0 - 6hr$, t_0 and $t_0 + 6hr$ time steps respectively (as indicated in the legends). Gray shading in (c) indicates longitudes where c_{gy} is not defined.*

central time step are given in Fig. 5.1f. Grid points where $E < 3ms^{-1}$ in any of the neighboring in time or longitude grid points are masked and depicted by gray shading. Repeating the procedure for all latitudes leads to the two-dimensional c_p field (Fig. 5.1g).

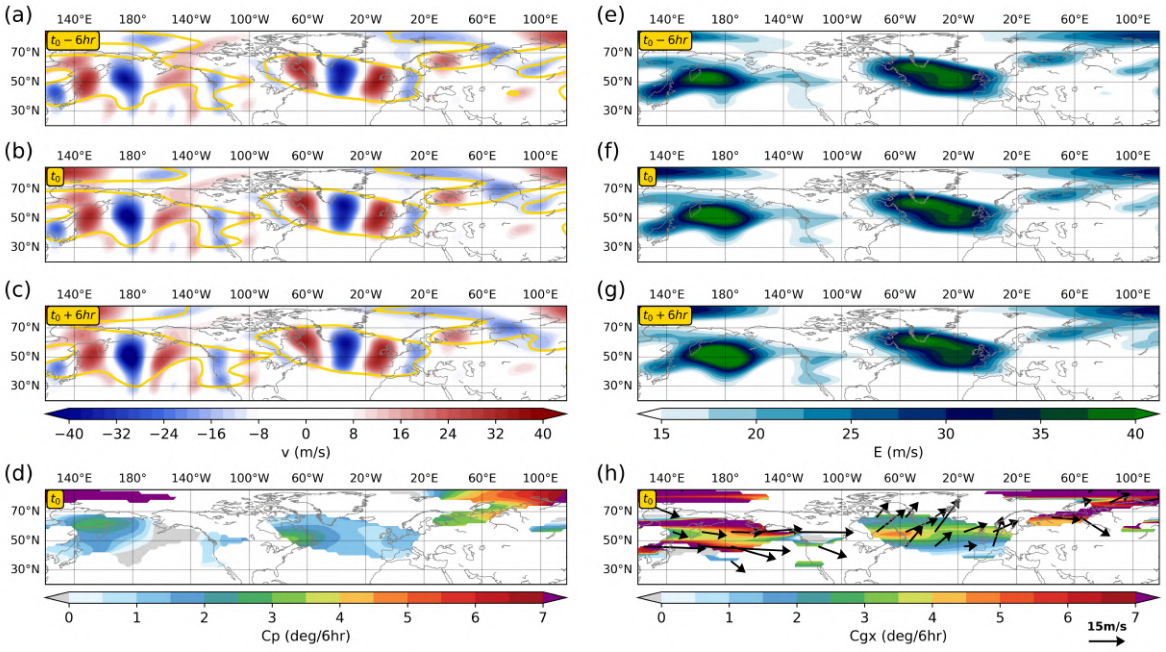

Fig. 5.3: *Illustration of the c_p and $\boldsymbol{c_g}$ diagnosis at t_0: 23 August 2016 - 1200 UTC. (a)–(c) v at three consecutive 6-hourly time steps (color shading) and isoline of $E_0 = 15ms^{-1}$ (yellow contour). (d) Map of c_p at t_0. (e)–(g) E at three consecutive 6-hourly time steps. (h) c_{gx} (color shading) in [deg/6hr] and arrows of $\boldsymbol{c_g}$ in [m/s] (scale is at the lower right) at t_0.*

Similarly, on the right column of Fig. 5.1 we present the steps for the diagnosis of the two-dimensional c_{gx} field corresponding to the central time step t_0. Fig. 5.1k shows in green the E_ℓ and E'_ℓ signals of the two detected RWP objects at time t_0 and latitude 40°N . Orange and blue lines denote the corresponding equal-length RWP objects at $t_0 - \delta t$ and $t_0 + \delta t$ respectively, detected as described in step (ii) of the previous subsection. Fig. 5.1l shows the local phase $\Phi_{E'_\ell}$ of the two RWP objects at the three consecutive time steps. The three solitary points around 140°E result from phase-wrapping. Fig. 5.1m shows c_{gx} computed along 40°N at longitudes where $\omega_{E'_\ell}$ and $k_{E'_\ell}$ are defined, while Fig. 5.1n shows the two-dimensional c_{gx} field.

Figure 5.2 presents the steps for the c_{gy} diagnosis in the same time step of the model simulation. The evolution of E_n, E'_n and $\Phi_{E'_n}$ for the detected RWP object along 80°E are shown in Figs. 5.2a,b. Figure 5.2c shows c_{gy} computed along 80°E at latitudes where $\omega_{E'_n}$ and $k_{E'_n}$ are defined, while the resulting two-dimensional c_{gy} field is shown in Fig. 5.2d.

Just for the purposes of presenting the diagnostics, c_p, c_{gx} and c_{gy} are given in degrees longitude/latitude per 6 hours, so that their values can be visually verified in Figs. 5.1a–c and 5.1h–j. Apparently, the fields within the two wave packets are smooth but not entirely homogeneous. Although such deviations from homogeneity

can be expected even in such idealized simulations (e.g., Pierrehumbert and Swanson 1995), some clear messages can nevertheless be inferred. For example, the zonal group velocity exceeds the phase velocity everywhere ($c_{gx} > c_p$), indicating the downstream development tendency of Rossby waves. This behavior reflects the well-known fact that the velocity with which energy is transported downstream is larger than the velocity of the individual troughs and ridges (Simmons and Hoskins 1979; Chang 1993). Furthermore, differences are apparent between the two wave packets, that have similar amplitude but distinct carrier wavenumber. The higher-wavenumber RWP in the Western Hemisphere is associated with generally larger phase velocity and lower group velocity than the lower-wavenumber RWP further downstream. Such behavior can also be anticipated from the theory of free Rossby waves in an inviscid barotropic fluid (e.g., Vallis 2017).

Figure 5.3 provides another example of the diagnostics, now in the real evolution of the upper-tropospheric meridional wind during 23 August 2016. Two main areas of enhanced waviness are found over the North Pacific and North Atlantic (Figs. 5.3a–c and 5.3e–g). The resulting c_p values of the ridge over Western Europe and the upstream trough centered at ∼20°W are approximately 1° longitude per 6 hours, which indicates a quasi-stationary wave (Fig. 5.3d). As will be shown in the climatological analysis of section 5.4, this was an unseasonably low phase velocity and plausibly critical for the emergence of a late-summer heat wave in Western Europe (Zschenderlein *et al.* 2018). Further investigation of the role of local RWP amplitude and phase velocity during temperature extremes will follow in section 5.5.

When it comes to group velocity, the c_{gx} field is generally noisier than c_p, reflecting the often incoherent and highly transient evolution of RWPs (Fig. 5.3h). The vector field of $\boldsymbol{c_g}$ is overlaid in Fig. 5.3h, hence also putting c_{gy} into consideration. Based on that, the North Pacific RWP moves predominantly in the zonal direction with an equatorward component at its southeastern leading edge. The North Atlantic RWP on the other hand, propagates slowly in the zonal direction with a general northeastward orientation. Amid the predominantly eastward propagation of RWPs, in the sense of c_{gx}, and individual troughs and ridges, in the sense of c_p, local and transient features of retrograde motion are not excluded and indeed sometimes observed. Such seems to be the case, e.g., in the weak westward phase propagation of the southerlies over the Gulf of Alaska as an upstream RWP approaches (Figs. 5.3a–d).

5.4 Seasonal climatologies

The climatological patterns of the aforementioned local RWP diagnostics are now investigated based on 40 years (1979–2018) of reanalysis data. In particular, maps of the median E, c_p, c_{gx} and c_{gy} at 300 hPa are presented for each season of the Northern and Southern Hemispheres, followed by a brief discussion in their most distinct features of seasonal and inter-regional variability. The median is used here as a more robust estimator (less affected by outliers). Time steps when c_p, c_{gx} and c_{gy} are not defined (see section 5.3), are not taken into account for the median calculation. In the case of the RWP amplitude climatologies, the values correspond to the median over time steps when $E \geq 15 ms^{-1}$ so that it roughly corresponds to the typical amplitude of the

RWPs that form the median of the other fields. The sample sizes for these conditional climatologies can be inferred from the RWP frequency maps in Fig. 5.15 of the Supplemental Material. In addition, Fig. 5.16 and 5.17 provide seasonal medians of u and v at 300 hPa to complement the RWP climatologies.

5.4.1 Northern Hemisphere

The two first panel rows in Figs. 5.4a–h quantify the seasonal variability of RWP amplitude (E) and phase velocity (c_p) respectively. For most regions in the extratropics a strong seasonality is apparent, associated with the maximization of wave activity during winter and its minimization during summer (see also Souders *et al.* 2014b), as well as changes in strength and location of the jet streams (Fig. 5.16). The bands of elevated E and c_p values over the two ocean basins signify the areas where RWPs tend to attain large amplitudes and phase velocities, respectively. The c_p values over the North Pacific and North Atlantic peak during winter at $\sim 9ms^{-1}$ and $\sim 8ms^{-1}$ respectively. Compared to winter, summer over the North Atlantic is characterized by a decrease of $\sim 2ms^{-1}$ in c_p magnitude and a poleward migration of $\sim 10°$ in the band of maximum values. The transition from winter to summer and vice versa for c_p values is more gradual in the North Atlantic, than in the North Pacific; the latter shows a weak decrease from DJF to MAM, a strong decrease from MAM to JJA and then a gradual increase from JJA to DJF through SON. Throughout the year, over the North Pacific, maximum values of RWP phase velocity are found to the west of the dateline, while RWP amplitudes maximize to the east of it (roughly 60° longitude downstream). Similarly, over the North Atlantic, c_p maximizes at the narrow band of the jet entrance (Fig. 5.16), while E maxima extend over a large area of the North Atlantic with increased values maintained all the way to Northern Europe (with an apparent poleward orientation during DJF). These results reflect the fact that low-amplitude waves grow in the areas of high baroclinicity (western ocean boundaries) and reach their (amplified) mature stage over the jet exit regions, where the phase velocity of their embedded troughs and ridges decreases.

The two lower panel rows (Figs. 5.4i–p) show c_{gx} and c_{gy}. Again, there is a distinct seasonality with values of group velocity maximizing during winter. It is apparent that c_{gx} exceeds c_p by up to three times in all seasons. This climatological tendency for downstream development is more pronounced in some regions (e.g., in the subtropical jet) than in others (e.g., the jet exit and cyclolysis region over Europe and the Norwegian Sea). Furthermore, by comparing the c_{gx} maps (Figs. 5.4i–l) to the respective ones of c_{gy} (Figs. 5.4m–p), it is apparent that RWP propagation is almost everywhere predominantly zonal ($c_{gx} > |c_{gy}|$).

In most regions the spatial pattern and seasonal variability of c_{gx} follows closely the ones of zonal wind velocity (Fig. 5.16). Focusing on the winter season, a distinct band of high c_{gx} values appears in the subtropical jet at a purely zonal orientation (at ~ 30°N) from Northwestern Africa to the North Pacific. Upon it, low-amplitude RWPs (Fig. 5.4a) propagate eastward at high zonal group velocities ($\sim 12 - 16ms^{-1}$; Fig. 5.4i) and near-zero meridional "leakage" as indicated by the low meridional group velocity values around it (Fig. 5.4m). Narrow and elongated as it is, the subtropical jet constitutes an efficient waveguide (e.g., Hoskins and Ambrizzi 1993); a "highway" for

transient RWPs that extends over a longitudinal sector of almost 180° . These RWPs can conceivably be excited when breaking waves over Europe (e.g., in the form of PV streamers, Wernli and Sprenger 2007) reach far south to the Mediterranean region and perturb the subtropical jet. Such a "bridge" between the eddy-driven and the subtropical jet can also be inferred from the enhanced equatorward propagation, in the sense of c_{gy}, over Europe (Fig. 5.4m). Furthermore, it is upon this jet where distinct low-frequency teleconnections are realized (Branstator 2002). Although less compact, a band of increased c_{gx} values on this waveguide is also observed in the other seasons (Figs. 5.4j–l).

During all seasons but summer, a secondary branch of relatively high c_{gx} values is evident to the north of the main waveguide (at ~ 50°N) within the 60°E to 120°E sector (see also Chang 2005). This branch follows a more northerly track over Siberia, presumably hosting RWPs that after exiting the poleward oriented North Atlantic jet, reach deep into Northern Asia (Figs. 5.4a–d and 5.15a–d). The study of Chang and Yu (1999) verifies the existence of this secondary Siberian waveguide, with disturbances that originate in Scandinavia and reach the North Pacific after 4 days.

Salient features in the seasonal patterns of c_{gy} do arise and are in good agreement with the ones in the lag-correlation analysis of Chang (1999). Focusing first on winter, positive values of c_{gy} are found to the north and negative values to the south of the North Pacific and North Atlantic jets (Fig. 5.4m), indicating RWPs that radiate away from the jets toward subpolar and subtropical regions respectively (Held and Hoskins 1985). Since the divergence of group velocity implies convergence of zonal momentum (e.g., Vallis 2017), the notion of eddy-driven jets is to some extend reflected in the climatological patterns of c_{gy}. From the viewpoint of baroclinic wave life cycles, poleward and equatorward propagation away from the jet latitude is often followed by cyclonic and anticyclonic wave-breaking respectively (Thorncroft *et al.* 1993; Esler and Haynes 1999b). The meridional propagation of RWPs in these studies is implied from the meridional component of wave activity flux (Plumb 1985), the DJF climatological spatial pattern of which (Fig. 6 in Gabriel and Peters 2008) closely resembles the one of c_{gy} (Fig. 5.4m).

Regarding the other seasons, the c_{gy} patterns do not vary considerably, but the magnitudes do. Minimum values are found in summer, while interesting asymmetries are evident between spring and autumn, with more pronounced negative c_{gy} values to the south of the jets in the latter. A firm feature throughout the year is the equatorward propagation over Southeastern Russia and Mongolia (Hsu 1987), even though the stationary southerly flow over the region (Fig. 5.17) is removed. This feature is associated with the aforementioned secondary c_{gx} branch over Siberia (Joung and Hitchman 1982; Chang and Yu 1999) and, as proposed by previous studies, constitutes an upstream source for cyclone development and Rossby wave initiation over the North Pacific (Hakim 2003; Chang 2005; Röthlisberger *et al.* 2018).

Worth highlighting in this analysis is also the Northwestern Pacific seasonality of the four fields in question. An interesting feature of this region is the combination of enhanced low-level baroclinicity (not shown), strong upper-level zonal winds (Fig. 5.16a) and relatively low E values during winter (compared to autumn and spring; Figs. 5.4a,b,d). This feature has been investigated in the past in the context of the Pacific midwinter suppression of eddy activity (Nakamura 1992; Schemm and Schneider

2018), a possibly important factor of which is the enhanced group velocity during the strong jet months (Chang 2001a). From the seasonal perspective presented here, it is shown in Fig. 5.4 that there are strong transitions in the c_{gx} and c_{gy} fields from autumn to winter and from winter to spring. The narrow band of enhanced c_{gx} as well as the elevated $|c_{gy}|$ values to the north and south of the jet during winter imply that RWPs have short residence times over the Northwestern Pacific. This implies that developing RWPs exit rapidly this strong part of the jet and only increase in amplitude further downstream, over the Northeastern Pacific.

5.4.2 Southern Hemisphere

Largely devoid of orographic forcing and land–sea differences, the Southern Hemisphere upper-tropospheric circulation is in many ways different from the Northern Hemisphere. This is also evident in the seasonal climatologies of E, c_p, c_{gx} and c_{gy} (Fig. 5.5). Primarily, the spatial patterns in all these fields are characterized by weaker seasonality and exhibit a lesser degree of zonal asymmetry compared to the Northern Hemisphere. In the following, we discuss some of the main aspects in the seasonal variability of the individual fields.

Regarding the E patterns, high RWP amplitudes in summer (DJF) are restricted to a narrow zonal band between 40 and 60°S (locally exceeding $24ms^{-1}$) associated with the mid-latitude jet. This band widens in the other seasons, especially over the South Pacific, and the highest amplitudes in many areas are found in autumn. This zonal asymmetry is associated with the enhanced baroclinicity over the Southern Atlantic and Indian oceans (Nakamura and Shimpo 2004).

Although c_p maximizes during winter and spring, in contrast to the Northern Hemisphere, the highest c_{gx} values occur in the fairly zonal and meridionally-confined summer mid-latitude jet. Generally higher values of u (Fig. 5.16), c_p and c_{gx} are found over the Southern Atlantic and Southern Indian mid-latitude jets compared to the Southern Pacific (Souders *et al.* 2014b). The high values over this sector are associated with enhanced storm track activity and intense SST gradients (Nakamura and Shimpo 2004). The slow phase velocity over the South Pacific is also associated with the frequently observed quasi-stationary cyclones over the Ross, Amundsen and Bellingshausen Seas, an important cause for the more frequent occurrence of Cold Air Outbreaks in that sector of the Southern Hemisphere (Papritz *et al.* 2015).

A prominent feature of all seasons except summer is the subtropical jet, that gives rise to a double jet circulation between 60°E and 120°W (Fig. 5.16) (e.g., Nakamura and Shimpo 2004). In its strongest phase during winter (tied to a strengthened Hadley cell), it is characterized by elevated values of c_{gx} over the Southern Indian ocean, Australia and the Southwestern Pacific ($13 - 16ms^{-1}$) and relatively enhanced values of E over the entire Southern Pacific ($21 - 24ms^{-1}$). Its emergence coincides with a weakening in c_{gx} values over the mid-latitude jet. Finally, a recurrent feature of the Northern Hemisphere that carries over to the Southern Hemisphere is the poleward (equatorward) c_{gy} values to the south (north) of the mid-latitude jet.

As a side note, although the patterns of c_p and c_{gx} in Figs. 5.4 and 5.5 match well with the lag-correlation analysis of Chang (1999), the peak magnitudes at the jet regions seem to be systematically lower in our case. Finding the cause of that is

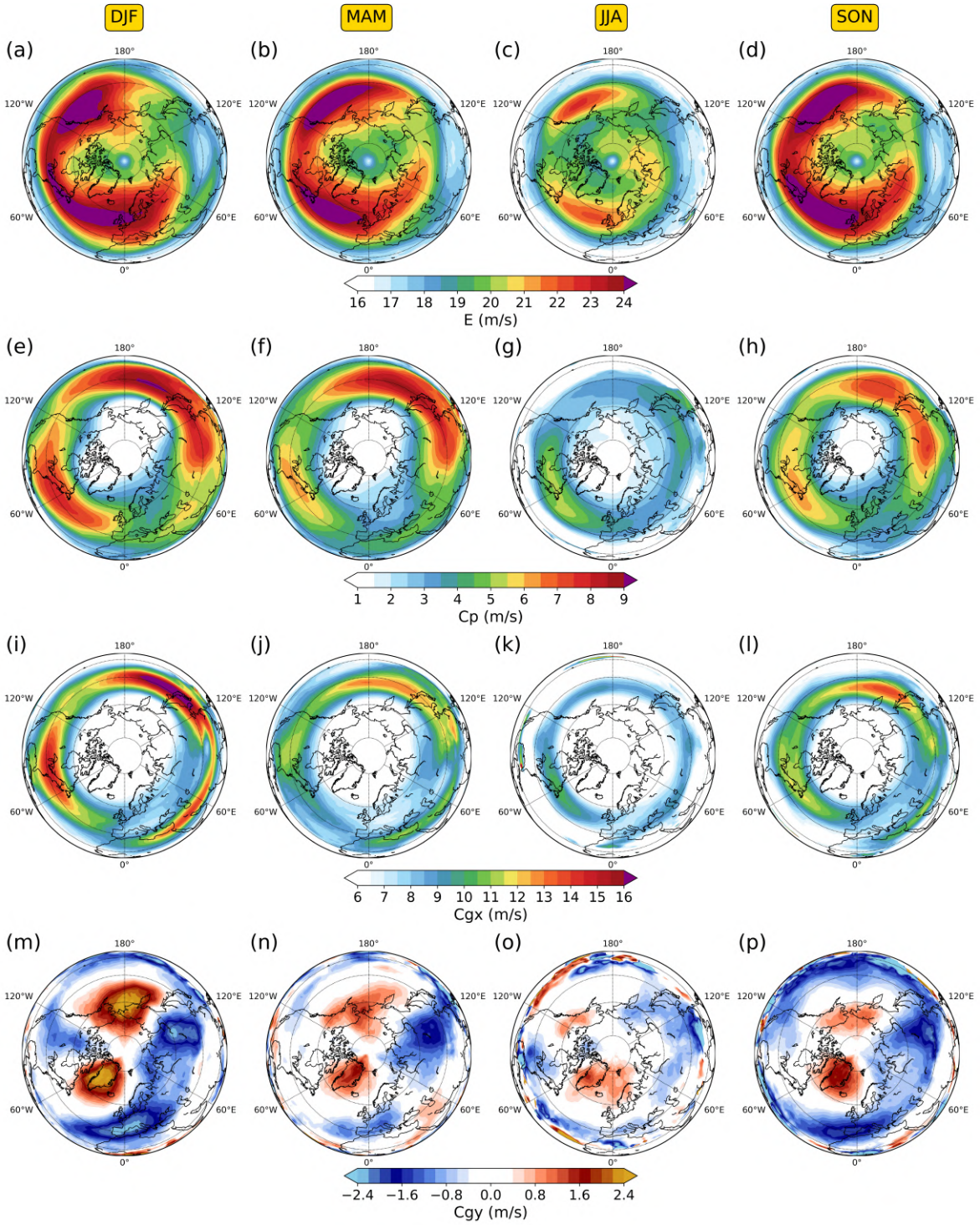

Fig. 5.4: *Northern Hemisphere climatology of RWP properties. Seasonal median of: (a)–(d) E, (e)–(h) c_p, (i)–(l) c_{gx} and (m)–(p) c_{gy} at 300 hPa in the 1979–2018 period. Each column of panels corresponds to the season indicated at the yellow label atop.*

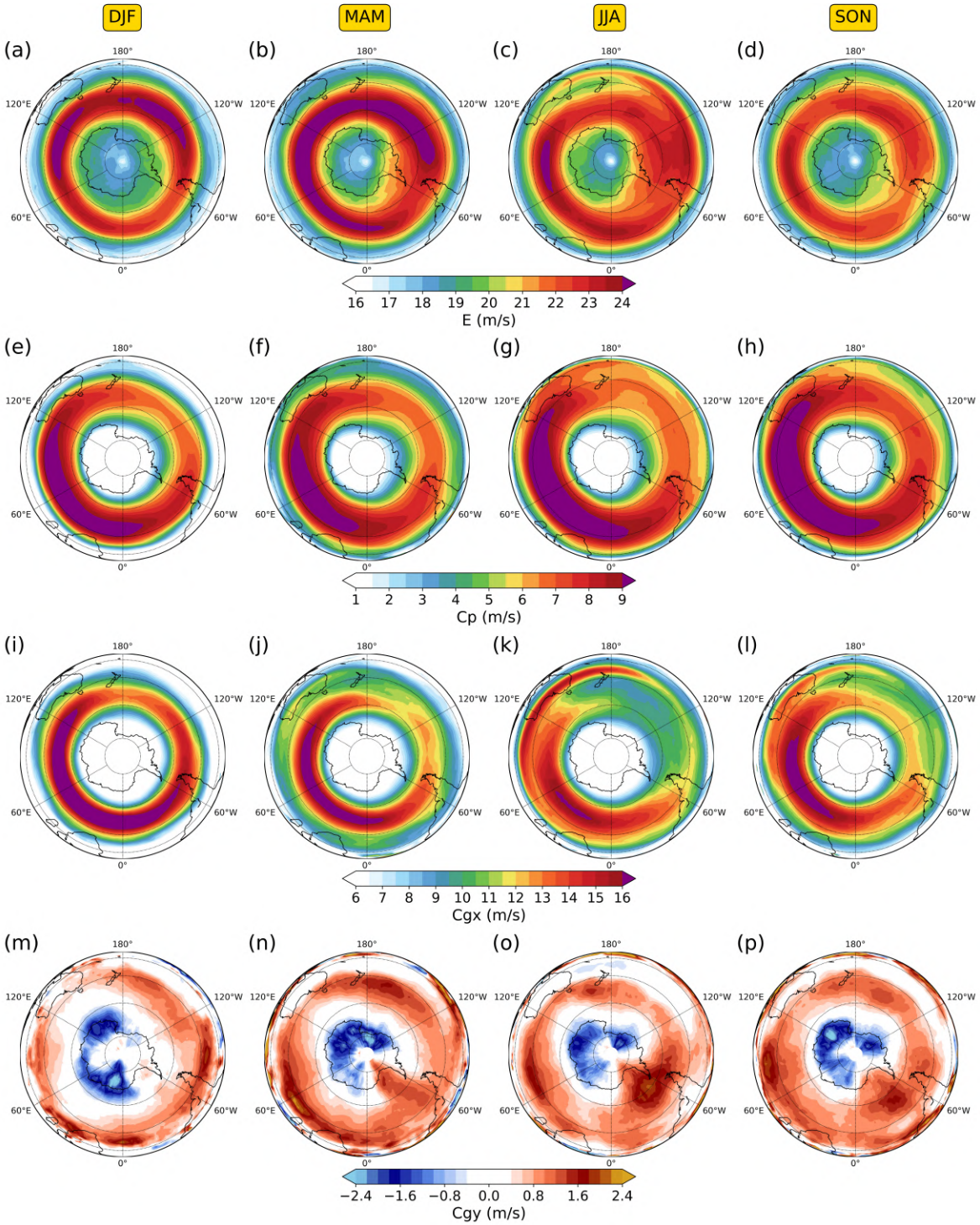

Fig. 5.5: *Same as Fig. 5.4, but for the Southern Hemisphere.*

not straightforward, given that the two methods are vastly different. An important distinction is, however, that our climatological distribution at a given grid point only contains time steps when c_p and c_{gx} are defined, which roughly occurs when $E \geq 15ms^{-1}$.

5.5 Role of RWP amplitude and phase velocity in temperature extremes

In this section, we investigate the role of RWP amplitude (E) and phase velocity (c_p) for the occurrence and duration of Central European hot and cold extremes. To do so, we construct time series of the area-averaged T', E and c_p fields and examine their climatological co-variability for hot/cold persistent and short-lived extremes. The hypothesis is that temperature extremes preferentially occur when an enhanced RWP amplitude characterizes the upper-tropospheric flow (see also Fragkoulidis *et al.* 2018), while their duration is largely determined by the RWP phase velocity.

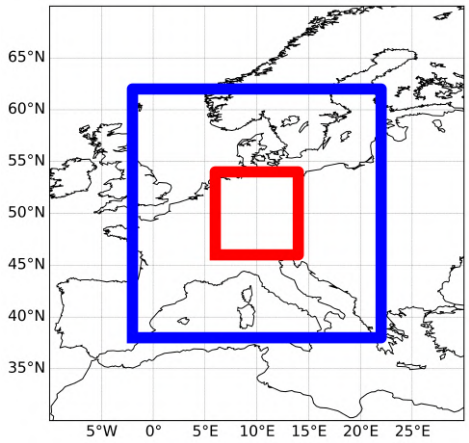

Fig. 5.6: *Areas used in averaging E and c_p at 300 hPa (blue rectangle) and T' at 850 hPa (red rectangle). The blue rectangle spans the area: 38°N –62°N , 2°W – 22°E and the red rectangle spans the area: 46°N –54°N , 6°E –14°E .*

First, we calculate the daily mean fields of temperature anomaly at 850 hPa, T', (as defined in section 5.2), E, and c_p for the whole period between January 1979 to December 2018. In the case of c_p, the mean takes into account only time instances when it is defined (section 5.3). If this condition is not met by any of the 4 time steps during a day, then the daily mean c_p value remains undefined (a "nan" value is given at these grid points). The daily mean T' is then averaged over the 8° x 8° (46°N –54°N , 6°E –14°E) area (red rectangle in Fig. 5.6) with a weighting by the cosine of latitude. The E and c_p daily means are instead averaged over the larger 24° x 24° (38°N –62°N , 2°W –22°E) area (blue rectangle in Fig. 5.6) in order to capture the entire synoptic situation around the affected region. The rationale behind this choice is that the temperature over an area is not only affected by the in situ flow. For E and c_p, the area-average only accounts for grid points where c_p is defined.

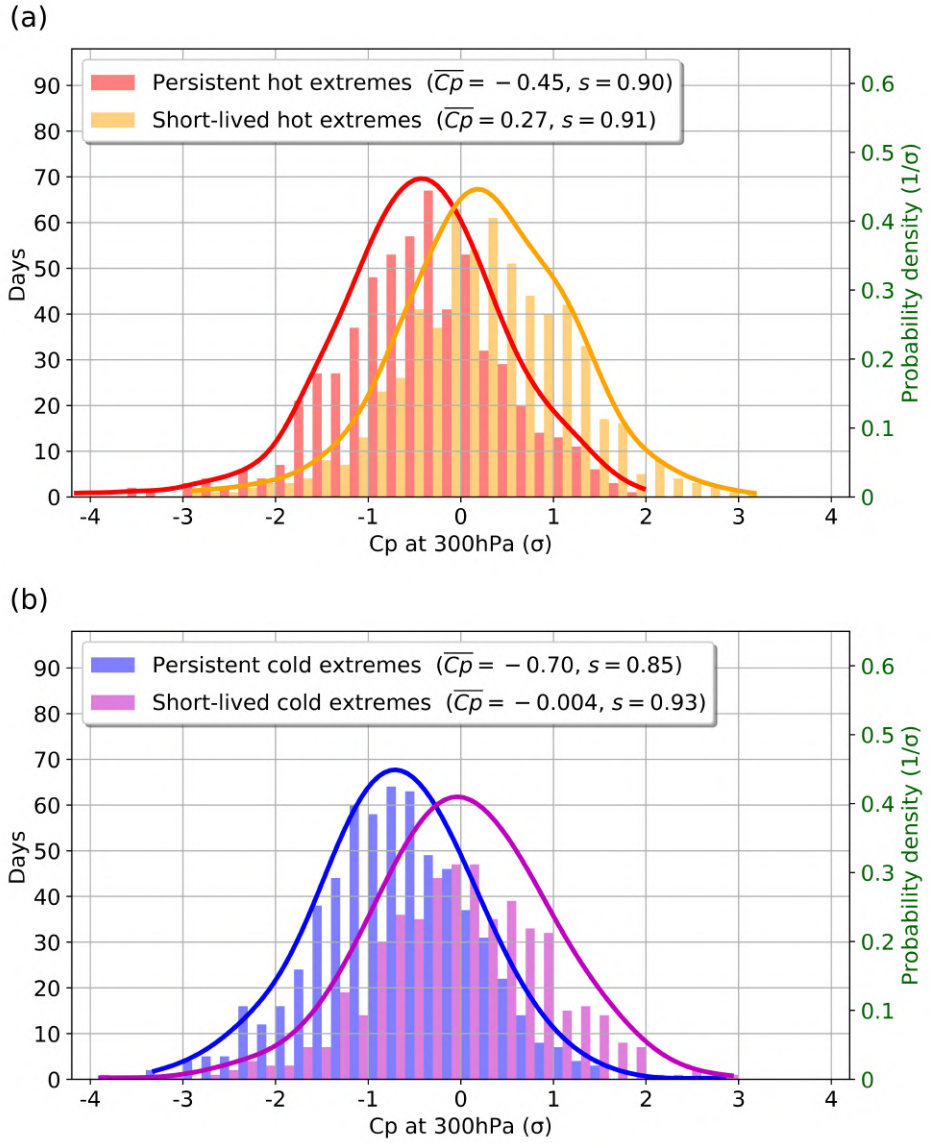

Fig. 5.7: *(a) Histogram (left axis) and the corresponding KDE (right axis) of the normalized (area-averaged) daily mean c_p at 300 hPa during hot extreme days over Central Europe. Red (orange) colors correspond to persistent (short-lived) hot extremes. Each bin accounts for 0.2 σ. (b) Same as (a) but for persistent (blue) and short-lived (purple) cold extremes. Shown in the legend is the mean ($\bar{c}_p$) and standard deviation (s) of c_p for each type of extreme. The KDE bandwidth parameter for persistent (short-lived) hot extremes is 0.27 (0.28) and for persistent (short-lived) cold extremes it is 0.36 (0.39).*

In view of more robust statistics we do not split the analysis in seasons, maintaining nevertheless information about the annual cycle (see below). Therefore, given the complete time series of the area-averaged T' at 850 hPa, cold and hot extreme events are detected as follows:

(i) First, the days when the area-averaged T' exceeds the 90^{th} percentile of their respective season constitute hot extreme days, whereas the days when it is smaller than the 10^{th} percentile of their respective season constitute cold extreme days. In this way, each season is equally represented in the analysis.

(ii) In order to examine the co-variability of the area-averaged T', E and c_p time series, we only keep days when the daily mean c_p is defined in at least 10% of the area (17 out of 169 grid points) so that we avoid cases where the area-averaged E and c_p account for just the edge of a RWP (which may not be representative of the synoptic situation; see section 5.3). This results in discarding 946 out of the total 14610 days, 32 (25) of which where hot (cold) extreme days (this corresponds to around 2% of all extreme days).

(iii) Episodes of 1 or 2 extreme days are regarded *short-lived* extremes, while episodes of 4 or more sequential extreme days are regarded *persistent* extremes. We leave out episodes that lasted exactly 3 days in order to have clear separation and similar distribution sizes of short-lived and persistent extreme days (Fig. 5.7).

Table 5.1 in the Supplemental Material, shows the resulting statistics for the temperature extremes of each season.

In order to test the effect of E and c_p in a pool of extreme days from all seasons, the area-averaged E and c_p distributions of each season are normalized by subtracting from each value the seasonal mean and dividing it by the seasonal standard deviation (σ). This way each E and c_p value now corresponds to an anomaly with units of standard deviations from its respective seasonal mean.

Figure 5.7 shows histograms of c_p during hot (a) and cold (b) short-lived and persistent extremes. The mean ($\bar{c_p}$) and standard deviation (s) of the 4 distributions are shown in the legends of the two panels. Evidently, in both hot and cold extremes there is a shift of approximately 0.7 standard deviations towards lower c_p values in persistent extremes compared to the short-lived ones. Using a Welch's t-test for the null hypothesis that the two independent samples have equal means (Ruxton 2006), it is found that the t statistic is 13.7 and 13.0 for hot and cold extremes respectively (unequal variances are assumed for the compared samples). The probability to get such values by chance (p-value) is well below 0.01, so in both cases the shift toward lower c_p values during persistent extremes is statistically significant at the 1% level. The shift becomes more clear when looking at the corresponding kernel density estimation (KDE) of the distributions (curved lines in Figs. 5.7a,b). This is calculated based on one-dimensional Gaussian kernels, the optimal bandwidth value of which (see caption of Fig. 5.7) was determined using a 20-fold cross-validation (Kohavi 1995; Pedregosa *et al.* 2011), (see also section 5.7.7 in the Supplemental Material).

For a more complete analysis of the role of RWP properties on temperature extremes, we calculated the c_p-E space distribution during the 4 types of temperature extremes (Fig. 5.8). The black contours in all panels of Fig. 5.8 depict the climatological

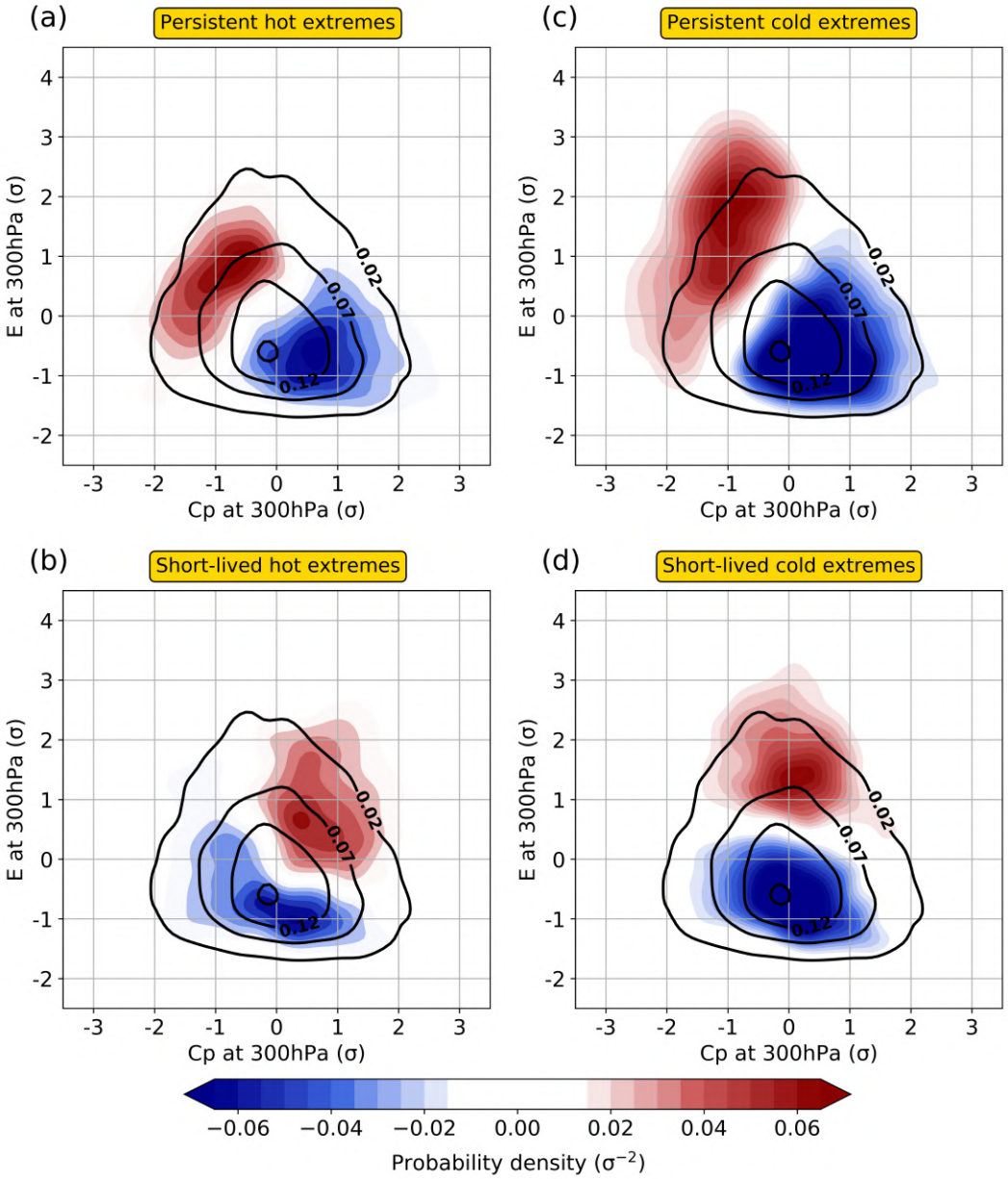

Fig. 5.8: *Two-dimensional KDE of the normalized (area-averaged) daily mean E against c_p at 300 hPa. Black contours correspond to the climatology (1979–2018), while the color shading depicts the anomaly during persistent (a) and short-lived (b) hot extremes, and persistent (c) and short-lived (d) cold extremes over Central Europe. The KDE bandwidth parameter for climatology is 0.19, for persistent (short-lived) hot extremes it is 0.34 (0.33) and for persistent (short-lived) cold extremes it is 0.39 (0.38).*

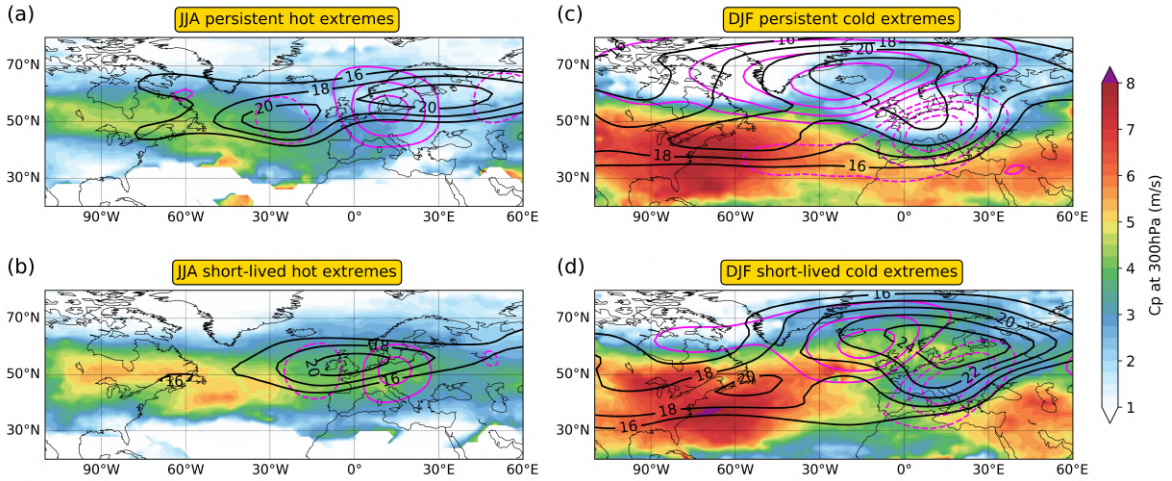

Fig. 5.9: *Inter-quartile mean of daily mean c_p (color shading), E (black contours at $18, 20, 22, 24\ ms^{-1}$) and Z' at 500 hPa (magenta contours at $\pm 4, \pm 8, \pm 12, \pm 16$ gpdam) during temperature extreme days over Central Europe. The panels correspond to: (a) JJA persistent hot, (b) JJA short-lived hot, (c) DJF persistent cold, and (d) DJF short-lived cold extreme days. For Z', solid (dashed) contours correspond to positive (negative) anomalies.*

distribution of the normalized c_p and E time series (a discussion on its triangular shape is included in section 5.7.5 of the Supplemental Material) and the color shading shows the anomaly of the distribution during the 4 types of temperature extremes. All distributions come from a two-dimensional Gaussian KDE where again a 20-fold cross-validation is employed for the bandwidth value optimization. During persistent hot and cold extremes there is a shift of the distributions toward higher E and lower c_p with respect to climatology (Figs. 5.8a,c). During short-lived extremes, a similar shift toward higher E is again evident, but c_p either remains unchanged (cold extremes; Fig. 5.8d) or even increases (hot extremes; Fig. 5.8b).

The synoptic to large-scale situation during the 4 types of temperature extremes is examined in composites of the (non-normalized) c_p, E and Z' fields. Since these fields have a pronounced annual cycle, we focus on JJA hot extremes and DJF cold extremes for this analysis. The composite fields are constructed by taking the mean over the daily values that rank within the inter-quartile range of the given extreme event type (e.g., JJA persistent hot extremes).

As implied from the previous results, c_p is lower over Central Europe and surrounding areas during the persistent hot and cold extremes than the short-lived ones (Fig. 5.9). Furthermore, in all cases, areas of enhanced RWP amplitude extend over parts of the North Atlantic and Europe, with a more pronounced signal for the DJF cases. During hot extremes, an area of increased geopotential height is located over Central Europe, at a relatively short distance to the northeast of the affected region. This high pressure system is more prominent in the composite of the persistent extremes and accompanied by weaker negative anomalies upstream and downstream of it. Finally, a pronounced dipole characterizes DJF persistent and — to a slightly lesser extent — short-lived cold extremes. In particular, the wide positive Z anomaly over

the North Atlantic indicates the presence of a blocking anticyclone, accompanied by a strong trough at its southeastern flank (see also Pfahl 2014).

For most areas around Europe, c_p is generally higher during the DJF extremes (Fig. 5.9). However, just over the affected region (Central Europe) c_p is lower during DJF persistent and short-lived cold extremes than during the JJA hot counterparts (also evident from the $\bar{c_p}$ values in Fig. 5.7). Despite that, the mean duration in each type of event is almost equal, as it can be inferred from Table 5.1 of the Supplemental Material: 5.6 (1.4) days for DJF persistent (short-lived) cold extremes and 5.5 (1.4) days for JJA persistent (short-lived) hot extremes. This implies that for a DJF cold extreme over Central Europe a more stationary trough-ridge pattern is needed than for a JJA hot extreme of the same duration. Presumably, this behavior stems from the fact that, during the high-pressure and clear-sky conditions of JJA hot extremes, reduced latent cooling due to the drying soils acts to enhance the temperature anomalies (Fischer *et al.* 2007b) and possibly extend the duration of the hot extreme as more time will be needed to fall below the 90^{th} percentile of T'. Reduced insolation and the presence of a low pressure system during DJF cold extremes (Fig. 5.9) imply that such a positive land–atmosphere feedback in these events does not occur.

Another interesting outcome to note here is that despite the climatologically lower c_p values of summer, more persistent hot and cold extremes are found during winter (57 in winter versus 49 in summer; see Table 5.1). The reason behind that lies in the characteristic weather evolution associated with these events. As shown before, the strong blocking anticyclone northwest of Central Europe provides almost stationary conditions during the DJF persistent cold extremes (Fig. 5.9). This observation suggests that a climatological mean should always be assessed in conjunction with the shape of the underlying distribution, which requires the consideration of the weather systems involved.

Overall, the results in this section verify in a quantitative fashion that temperature extremes in Central Europe require an enhanced RWP amplitude, but a prerequisite for the event to persist is a below-normal phase velocity in the trough-ridge pattern aloft.

5.6 Summary and further remarks

In this study, we proposed a novel method for the diagnosis of horizontal RWP phase and group velocity, locally in space and time. The methodology involves computing the analytic signal of upper-tropospheric meridional wind along a latitude circle for the detection of local phase velocity in the zonal direction. The zonal and meridional components of local group velocity were diagnosed by following the same principle in the envelope function of RWP objects. Using ERA5 reanalysis data for the time period 1979–2018, we produced global climatologies of RWP amplitude and the aforementioned fields. A distinct seasonal and inter-regional variability was observed in the respective RWP properties, while differences and similarities between the Northern and Southern Hemispheres were apparent. Finally, we were able to quantify the important role of RWP amplitude and zonal phase velocity in the occurrence and duration of Central European temperature extremes.

Limitations of the analytic signal approach to extract local properties of a signal are discussed in Huang *et al.* (2009). The methodology steps we followed for the diagnosis of local c_p and $\boldsymbol{c_g}$ were designed in a way that, for the areas of RWPs where we restrict the calculations to, the v'_ℓ, E'_ℓ and E'_n signals do not suffer from these limitations (see also discussion in section 5.3). Nevertheless, noisy patterns in the c_p and $\boldsymbol{c_g}$ fields are not unlikely. The local evolution of these fields is expected to be smooth in idealized simulations of plane waves and coherent RWP propagation, as in the barotropic model example of section 5.3, but not in every real case scenario. Of course, transient flow features within the individual troughs and ridges can affect the upper-tropospheric meridional wind field, resulting in a seemingly incoherent RWP evolution. In addition, spurious values of c_p and $\boldsymbol{c_g}$ can appear when RWPs reach a highly nonlinear stage and break. This problem does not arise very often though, since in such cases of wave breaking the RWP amplitude (E) is generally not acquiring large enough values, so c_p and $\boldsymbol{c_g}$ are not defined.

The presented results were tested for their sensitivity to variations in several parameters. Although the spatial patterns in Figs. 5.4 and 5.5 did not change with an increase of the E_0 threshold from $15ms^{-1}$ to $20ms^{-1}$, the c_p and c_{gx} magnitudes were slightly decreased and c_{gy} increased. The reason was presumably that now at each grid point our sample consisted of RWPs that were on average at a more mature stage of their lifetime. In addition, changes in the precise value of the minimum length and width thresholds ($\mathcal{L}_0$ and $\mathcal{N}_0$) in the group velocity diagnosis (section 5.3.3) had barely any effect on the results. Slight variations in the spatiotemporal smoothing of v' (section 5.2) prior to the diagnosis of E, c_p and $\boldsymbol{c_g}$ did not lead to a noticeable change in the climatological analyses of sections 5.4 and 5.5. Finally, it should be noted that the presented climatological patterns are expected to slightly vary in magnitude and position for different isobaric levels than the 300 hPa used here. One reason is that the typical height of the jets varies with the latitude and the season. The subtropical jets for example are located higher than the mid-latitude ones. Nevertheless, we believe that 300 hPa is a good compromise, capturing the annual cycle of the main upper-tropospheric circulation features of the two hemispheres.

Overall, the proposed diagnostics capture accurately and with low computational demands the local properties of the RWP spatiotemporal evolution. They can thus facilitate, among other things: a better understanding of the RWPs interplay with smaller scale processes, an objective partition into propagating and stationary waves as well as further investigations on the role of RWPs in weather extremes. In applications where the characteristic properties of individual RWPs need to be identified, the areal average of the two-dimensional c_p and $\boldsymbol{c_g}$ fields may be considered. Finally, future studies may further utilize these diagnostics for the investigation of processes that can alter the properties of the large-scale circulation at weather and climate time scales, while fully taking any zonal asymmetries into account.

Acknowledgements

The research leading to these results has been done within the Transregional Collaborative Research Center SFB / TRR 165 “Waves to Weather” (www.wavestoweather.de)

funded by the German Research Foundation (DFG). We are grateful to Paolo Ghinassi for providing the barotropic model data and the Copernicus Climate Change Service for providing access to the reanalysis data. We would also like to thank Lukas Papritz for insightful discussions regarding the Southern Hemisphere climatologies. Finally, we gratefully acknowledge the computing time granted on the supercomputer Mogon at the Johannes Gutenberg University Mainz (hpc.uni-mainz.de).

5.7 Supplemental Material

5.7.1 Local phase diagnosis

In this section we discuss the diagnosis of local phase (Φ) in meridional wind and the envelope function and as presented in section 5.3 of the paper. The notation here follows the one of the paper. Figure 5.10 illustrates the procedure for the case of the (artificial) function:

$$\upsilon(x) = e^{-(x-\pi/2)^2} cos(12x) + e^{-(x-3\pi/2)^2} cos(6x) \ , \tag{5.12}$$

where we may assume that: $x = acos\phi_0\lambda$. This function is shown in Fig. 5.10 as the blue solid line and can be thought of as depicting two idealized RWPs of equal amplitude along latitude ϕ_0; one of carrier wavenumber 12 centered at 90°E and one of carrier wavenumber 6 centered at 90°W . The blue dotted line in Fig. 5.10 corresponds to the imaginary part of the analytic signal A_υ (eq. 2 in the paper), which is equivalent to the Hilbert transform of the original function (phase-shift of $\pi/2$). The thick blue dotted line in panel (b) of Fig. 5.10 shows the corresponding local phase Φ_υ (eq. 6 in the paper). Φ_υ is zero at the local maxima of υ and "wraps around" at its local minima, where the phase value approaches π. Furthermore, Φ_υ is positive (negative) when the imaginary part of A_υ is positive (negative). The higher slope in Φ_υ of the RWP to the left reflects its higher wavenumber compared to the one on the right.

The gray line in panel (a) of Fig. 5.10 corresponds to the envelope, E, of υ. In order to compute the local phase of E (and eventually the group velocity) we discard its mean, so that it is a wave-like function that oscillates around zero (E', red solid line). Again based on the analytic signal, the thick red dotted line in (b) corresponds to the phase function of the envelope, $\Phi_{E'}$. Given that the two RWPs have the same amplitude and length, their $\Phi_{E'}$ function is also equivalent.

We now repeat the calculations on the function:

$$\upsilon(x) = e^{-(x-\pi/2)^2} cos(12x) + 0.4e^{-(x-3\pi/2)^2} cos(6x) \ , \tag{5.13}$$

which only differs from (5.12) in that the RWP on the right has a lower amplitude (Fig. 5.11). Although, Φ_υ remains unaffected as the amplitude changes (as it should), the same is not true for $\Phi_{E'}$. The global zonal mean E is now not representative of the two RWPs and, when subtracting it, E' for the RWP on the right is brought almost entirely below zero. As a result, in the area of the latter, $Im[A_{E'}]$ and E' are not consistent and $\Phi_{E'}$ fails. This is a clearly undesirable effect, as situations when two RWPs of different amplitude and/or length evolve at the same latitude circle are found more often than not.

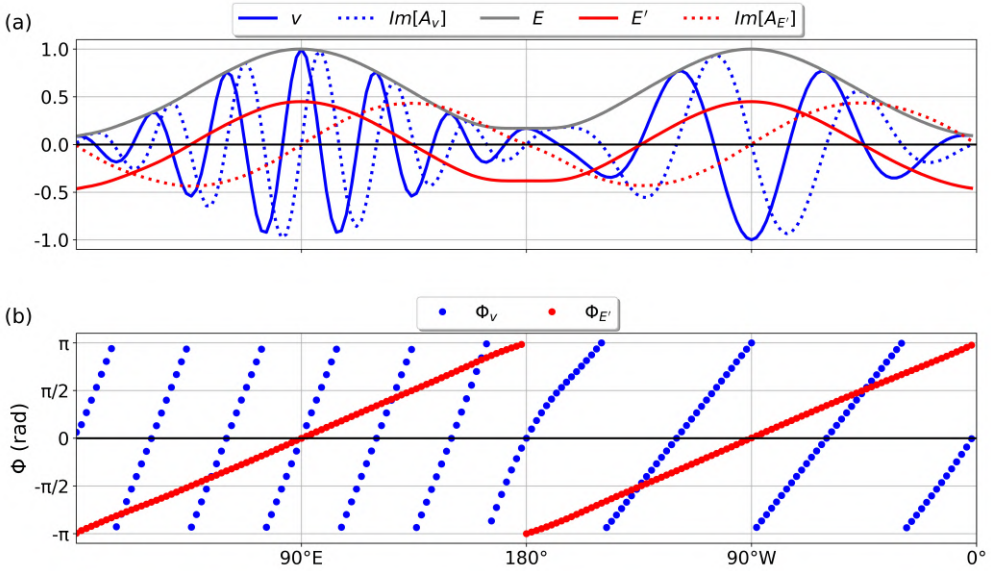

Fig. 5.10: *Local phase diagnosis in the case of two RWPs with equal amplitude and length. Panel (a) depicts the original function ($v(x)$, blue solid line), the imaginary part of its analytic signal ($Im[A_v]$, blue dotted line), the envelope (E, gray line), the envelope deviation from the mean (E', red solid line) and the imaginary part of its analytic signal ($Im[A_{E'}]$, red dotted line). Panel (b) shows the local phase of v (Φ_v, thick blue dotted line) and E' ($\Phi_{E'}$, thick red dotted line).*

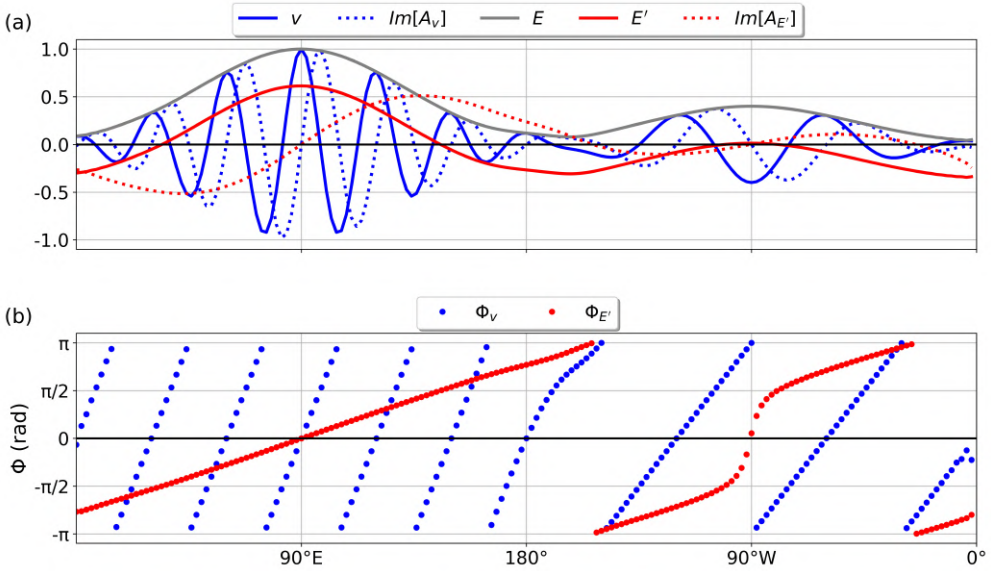

Fig. 5.11: *Same as Fig. 5.10, but for the case of two RWPs with equal length but unequal amplitude.*

Figure 5.12 shows how these issues are overcome by using the object-based envelope phase diagnosis. The gray line again shows the envelope function in question. Gray shading outlines the segments of the envelope function that are smaller than 0.15 (our object definition threshold for this artificial function). The thick red dotted line in panel (a) corresponds to the deviation of E from the object zonal mean of the respective RWP. Clearly, these two functions now oscillate around zero and are consistent with their respective $Im[A_{E'}]$ functions. The phase is now computed separately for the two RWP objects using eq. 6 of the paper on the longitudinal segments they cover (for the shaded area in between we will not get any phase information). The thick red dotted line in panel (b) corresponds to the local phase within the two RWPs, which no longer suffers from the discontinuity shown in Fig. 5.11. As a side note, in case the RWP object has an odd length, eq. 3 of the paper becomes:

$$\tilde{A}_m = \begin{cases} \tilde{v'}_m & \text{for} \quad m = 0, \ , \\ 2\tilde{v'}_m & \text{for} \quad 1 \leq m \leq (L-1)/2 \ , \\ 0 & \text{for} \quad (L-1)/2 + 1 \leq m \leq L-1 \ . \end{cases} \tag{5.14}$$

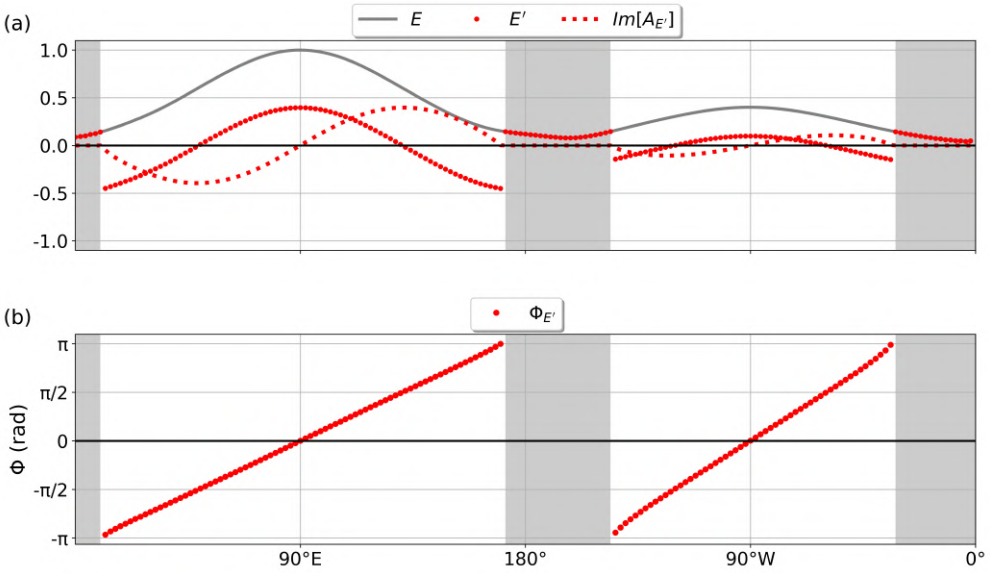

Fig. 5.12: *Object-based envelope phase diagnosis in the case of the two RWPs in Fig. 5.11. Panel (a) depicts the original envelope (E, gray line), the envelope deviation from the object zonal mean (E', thick red dotted line) and the imaginary part of the analytic signal of the two RWPs ($Im[A_{E'}]$, red dotted line). Panel (b) shows the local phase of E' ($\Phi_{E'}$, thick red dotted line).*

The slope of the phase function now depends on the length of each RWP, which in turn depends on the threshold value. If we, for example, increase the threshold to 0.25, the RWP length decreases and the slope of its phase function will increase. The local angular wavenumber of the RWP will increase accordingly, but so will the local angular frequency (if we assume a propagation of this artificial wave). Therefore, the local group velocity, that we eventually aim to diagnose in the paper, does not depend on the exact threshold value. The only requirement is that the RWP objects in the three successive

time steps that are involved in the c_{gx} or c_{gy} diagnosis ($t = t_0 - 6hr,\ t_0,\ t_0 + 6hr$) have the same length (section 5.3.3 in the paper).

Figure 5.13 further illustrates the need for this equal-length requirement. We reproduce Fig. 5.2 of the paper, without imposing equal lengths in the E_n segments of the three involved time steps. Focusing on 60°E where the trailing edge of the RWP to the right is located, it can be seen that the E_n function remains centered at around 44°N but its length decreases with time (Fig. 5.13a). The corresponding phase function in all three time steps intersects the zero line at around 44°N but its slope increases with time (Fig. 5.13b). As a result, c_{gy} is positive to the south of 44°N and negative to the north of it (Fig. 5.13c). The opposite effect occurs at the leading edges of the two RWPs (Fig. 5.13d). This is arguably a behavior we do not want when diagnosing the velocity vector field of RWPs. From a Lagrangian perspective, the RWP during the course of these 12 hours propagates with a fairly compact shape (Figs. 5.1h–j) and its trailing (leading) edge is not thinning (widening) as the c_{gy} values in Fig. 5.13c would suggest. The equivalent effect in the computation of c_{gx} would be, e.g., an RWP that shortens (spans less longitudes) with time but whose centroid remains stationary. This case could reflect a decaying stationary RWP and we do not want that stage to be manifested as eastward c_{gx} in the trailing edge and westward c_{gx} in the leading edge.

5.7.2 Derivatives in the "wrapped" phase function

Here we present how we compute the derivatives of the phase function, Φ, in space (latitude or longitude) and time given that it is constrained to the $(-\pi, \pi]$ interval. Simply "unwrapping" the function by adding $2\kappa\pi$ ($\kappa \in \mathbb{N}^*$) in the $\kappa - th$ segment of the wrapped Φ would work for the calculation of the local angular wavenumber ($\partial\Phi/\partial x$), but not for the local angular frequency ($-\partial\Phi/\partial t$). A problematic situation is when e.g. weak meridional wind values (that are susceptible to perturbations) upstream of a RWP form a wave-like oscillation around zero at $t = t_0 - 6hr$, but not at $t_0 + 6hr$. In this case, $2\kappa\pi$ will only be added in the first case and the two Φ functions involved in the calculation of $\partial\Phi/\partial t$ will diverge and result in an incorrect time derivative from that longitude onward. Therefore, our procedure here for the centered differences in time (t) is the following ($\delta t = 6$ hours):

$$-\frac{\partial \Phi_i}{\partial t} = \begin{cases} \frac{\Phi_i(t-\delta t)+2\pi-\Phi_i(t+\delta t)}{2\delta t} & \text{if} \quad \Phi_i(t+\delta t) - \Phi_i(t-\delta t) > \pi \ , \\ \frac{\Phi_i(t-\delta t)-2\pi-\Phi_i(t+\delta t)}{2\delta t} & \text{if} \quad \Phi_i(t+\delta t) - \Phi_i(t-\delta t) < -\pi \ , \\ \frac{\Phi_i(t-\delta t)-\Phi_i(t+\delta t)}{2\delta t} & \text{otherwise} \ , \end{cases} \tag{5.15}$$

where i denotes v', E'_ℓ or E'_n. This evaluation makes sure that even in a case of westward propagation the derivative is calculated correctly. For consistency, the centered differences in space are calculated as follows ($\delta x = 2$ degrees):

$$\frac{\partial \Phi_i}{\partial x} = \begin{cases} \frac{\Phi_i(x+\delta x)+2\pi-\Phi_i(x-\delta x)}{2\delta x} & \text{if} \quad \Phi_i(x-\delta x) - \Phi_i(x+\delta x) > \pi \ , \\ \frac{\Phi_i(x+\delta x)-2\pi-\Phi_i(x-\delta x)}{2\delta x} & \text{if} \quad \Phi_i(x-\delta x) - \Phi_i(x+\delta x) < -\pi \ , \\ \frac{\Phi_i(x+\delta x)-\Phi_i(x-\delta x)}{2\delta x} & \text{otherwise} \ , \end{cases} \tag{5.16}$$

where, depending on the application, x denotes longitude or latitude.

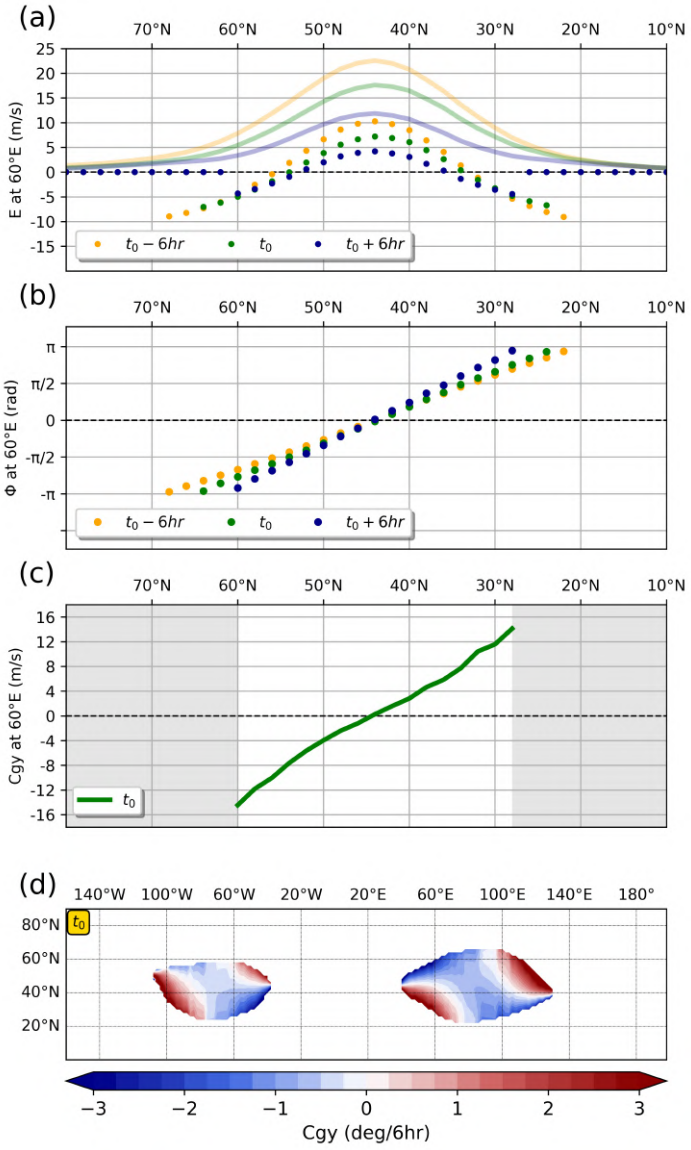

Fig. 5.13: *Illustration of the c_{gy} diagnosis as in Fig. 5.2 of the paper, but without the equal-length requirement. (a) E_n (solid lines) and E'_n (dotted lines) at 80°E for the three consecutive 6-hourly time steps. (b) $\Phi_{E'_n}$ evolution at 80°E. (c) c_{gy} at 80°E. (d) Map of c_{gy} at t_0. Orange, green and blue colors in (a)–(c) correspond to the $t_0 - 6hr$, t_0 and $t_0 + 6hr$ time steps respectively (as indicated in the legends). Gray shading in (c) indicates longitudes where c_{gy} is not defined.*

5.7.3 Wavelet analysis on meridional wind along a latitude circle

In this section we apply a wavelet transform analysis on meridional wind anomaly, v', along a latitude circle. We follow the methodology of Ghinassi *et al.* (2018)[¶], where a complex-valued Morlet wavelet is used as the basis function. Fig. 5.14 is intended to illustrate that at any given longitude, v'_ℓ has a power spectrum that may span more than one wavenumbers, which also depends on the basis function choice (Ghinassi *et al.* 2018). This indicates that, generally, v' along a latitude circle is not a "monocomponent" function (Huang *et al.* 1998). The black dashed line in Fig. 5.14 indicates the maximum in wavelet power at every longitude and denotes the local dominant wavenumber. The local wavenumber, $k_{v'_\ell}$, as computed in the paper (here given in cycles per 2π) for the local c_p is shown in the black line. At longitudes where E exceeds 15 ms^{-1}, the two diagnostics show good agreement. In case there are multiple local extrema between two zero-crossings of the function, as is the case in the 80–130°W and 50–110°E longitudinal ranges, $k_{v'_\ell}$ decreases and can even get negative. Although the notion of local angular wavenumber would not be physically meaningful in such situations (Huang *et al.* 2009), they mostly occur outside the well-defined RWPs that we consider in this study.

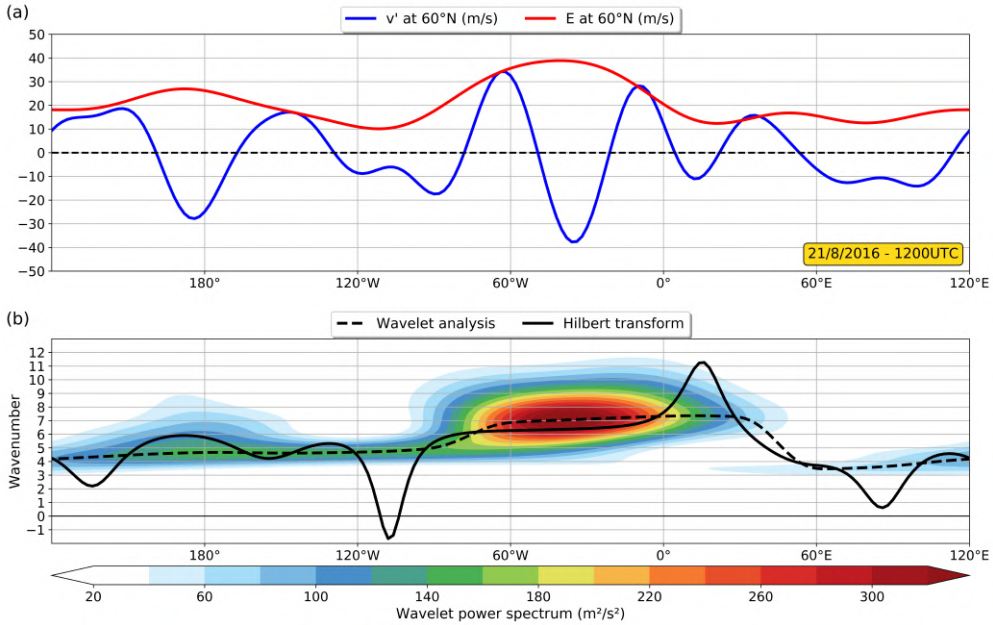

Fig. 5.14: *Wavelet analysis on meridional wind along a latitude circle at 21/8/2016 - 1200 UTC (Fig. 5.3 in the paper). (a) Meridional wind anomaly, v'_ℓ, and its envelope, E_ℓ, at 60°N. (b) Wavelet power spectrum (color shading) and its maximum at every longitude (black dashed line) which corresponds to the dominant wavenumber. The black line corresponds to the local wavenumber as computed by the Hilbert transform method (eq. 5.10 in the paper).*

[¶]See also Appendix A.

5.7.4 Additional climatologies

Additional climatologies are presented here as a reference, to complement the seasonal variability investigation of section 5.4 in the paper. All climatologies refer to the 1979–2018 period in ERA5 reanalysis data (section 5.2 in the paper).

The maps in 5.15 depict the percentage of time steps in the 1979–2018 period for which E exceeds the $15ms^{-1}$ threshold. Therefore they correspond to a climatology of RWP frequency. They also give an idea of how often c_p and $\boldsymbol{c_g}$ are computed at each grid point. Figures 5.16 and 5.17 correspond to the median zonal and meridional wind at 300hPa respectively.

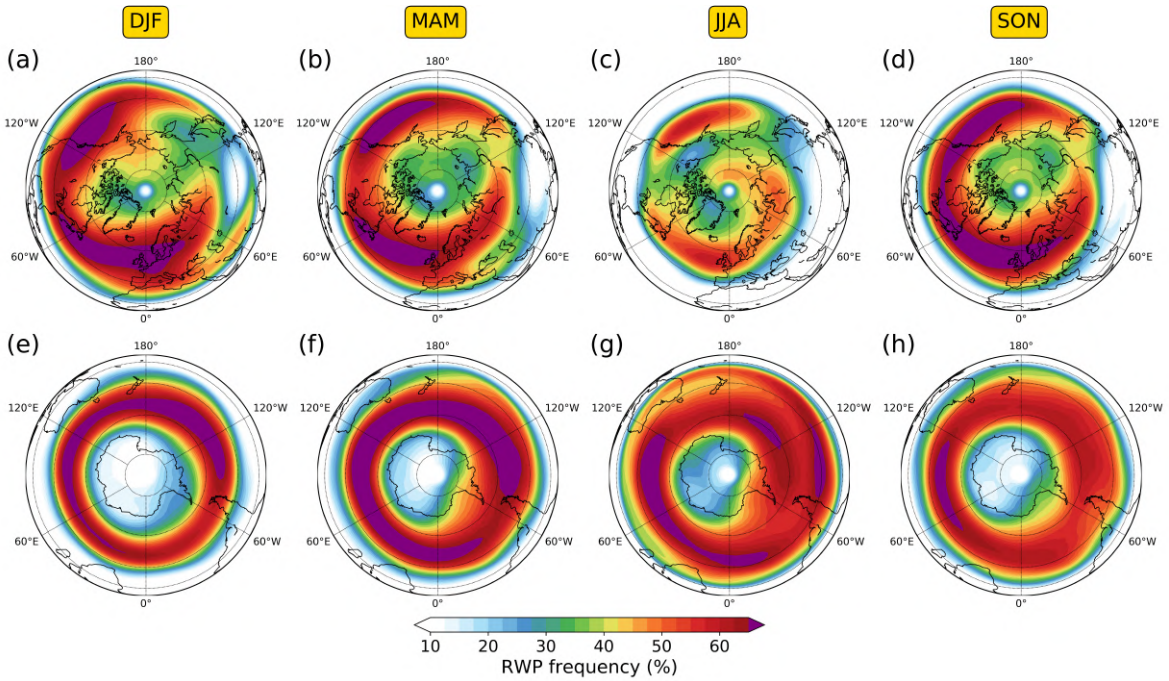

Fig. 5.15: *RWP frequency (%) at 300hPa in the Northern (a)–(d) and Southern (e)–(h) Hemispheres. Each column of panels corresponds to the season indicated at the yellow label atop.*

5.7.5 Phase velocity – RWP amplitude distribution

In this section we investigate the triangular shape of the normalized c_p–E climatological distribution over Europe (Fig. 5.8 in the paper). The area averaging for both c_p and E corresponds to the average over the grid points within the 38°N –62°N , 2°W –22°E area, at grid points where c_p is defined. In particular, we plot composites of the days that occupy the three vertices of this triangle (Figs. 5.18 and 5.19). Regime (a) corresponds to very high E and average c_p over Europe. Regime (b) corresponds to near-zero c_p and very small E over Europe, but enhanced E to the north and upstream. Finally, regime (c) corresponds to very high c_p and very small E over Europe, but enhanced E upstream. Essentially, regimes (a) and (c) reflect the fact that a RWP of higher amplitude is generally associated with lower phase velocity and vice versa (within weakly nonlinear limits, Esler 2004). Regime (b) deviates from this idealized behaviour.

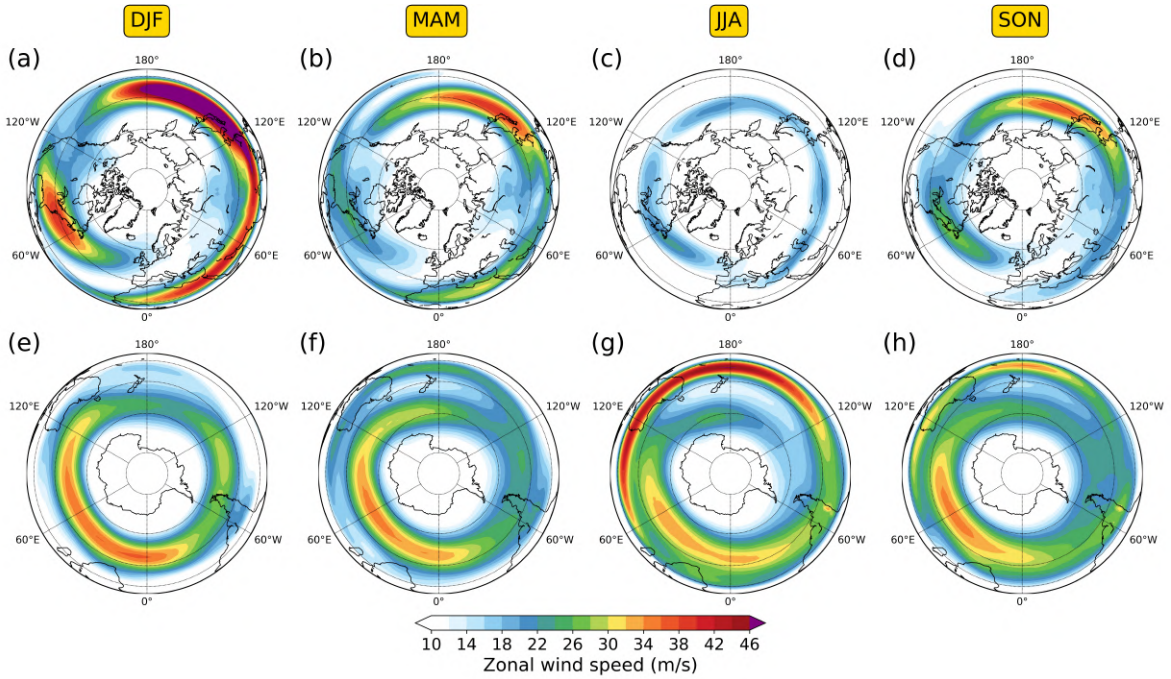

Fig. 5.16: *Median zonal wind speed at 300hPa in the Northern (a)–(d) and Southern (e)–(h) Hemispheres. Each column of panels corresponds to the season indicated at the yellow label atop.*

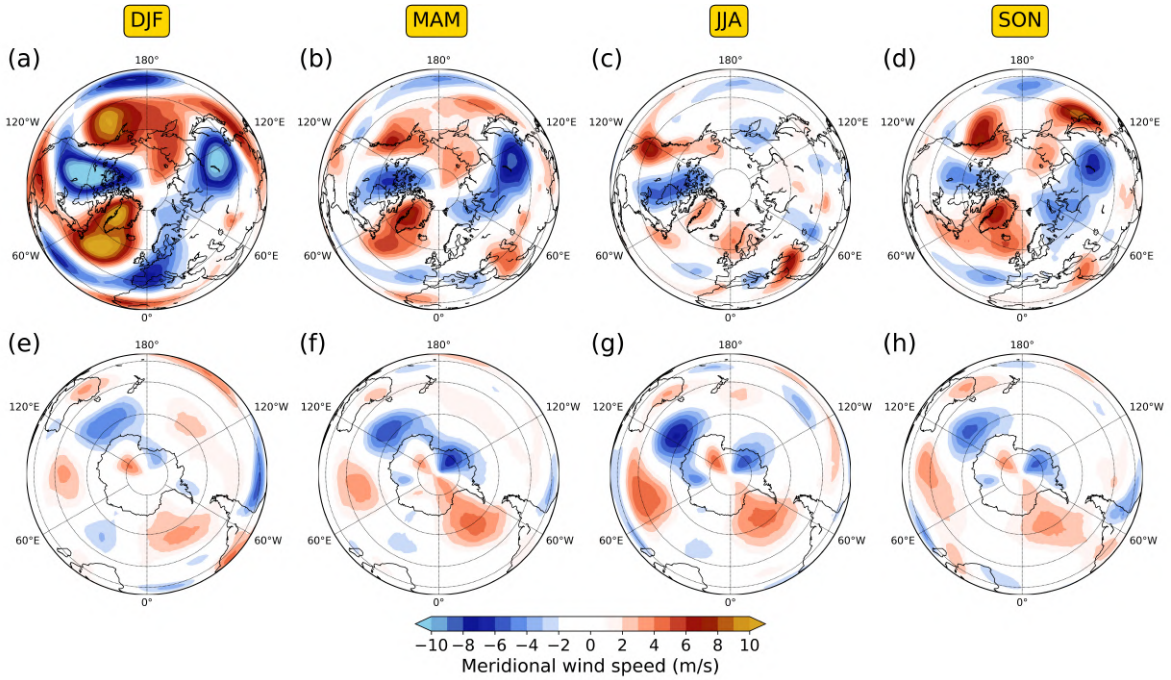

Fig. 5.17: *Median meridional wind speed at 300hPa in the Northern (a)–(d) and Southern (e)–(h) Hemispheres. Each column of panels corresponds to the season indicated at the yellow label atop.*

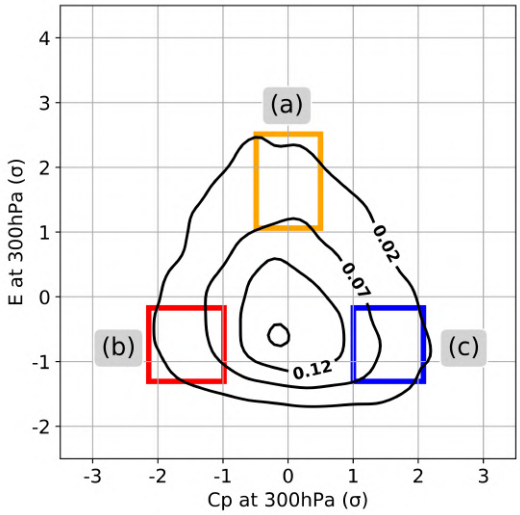

Fig. 5.18: *Two-dimensional kernel density estimation of the normalized (area-averaged) daily mean E against c_p at 300hPa. Black contours correspond to the climatology (1979–2018). The 3 rectangles indicate the regimes at the 3 vertices of the distribution. Their specific range in percentiles of E and c_p is: a) $E \in (85^{th}, 98^{th})$ and $c_p \in (30^{th}, 70^{th})$, b) $E \in (5^{th}, 50^{th})$ and $c_p \in (2^{th}, 15^{th})$, c) $E \in (5^{th}, 50^{th})$ and $c_p \in (85^{th}, 98^{th})$.*

It apparently accounts for cases when only a low-amplitude quasi-stationary edge of the RWP falls within the area of interest (Fig. 5.19b).

5.7.6 Central European temperature extreme statistics

Table 5.1 shows the number of Central European hot and cold extremes (at 850hPa) per season, providing a reference for section 5.5 of the paper. As described in the paper, a day is regarded as a hot (cold) extreme if the area-averaged T' ranks in the highest (lowest) 10% of the respective season and c_p is defined. Days that constitute 3-day extreme events have been discarded in order to achieve a clear separation between persistent and short-lived extremes. Extreme events that started toward the end of a season and continued to the next (e.g. 29 August – 2 September) are regarded as extreme events of the first season.

5.7.7 Computation methods

The computations in this study were conducted in Python 3.6.5. The Climate Data Operators (CDO) 1.7.2 (Schulzweida 2019) was used for some basic handling of the reanalysis data files. The netCDF4 1.4.0 library (Unidata 2018) was used for reading the data, while NumPy 1.14.3 (van der Walt *et al.* 2011) was used for routine array operations and data analysis. Matplotlib 2.2.2 (Hunter 2007) was used for plotting. Finally, Table 5.2 highlights some more specific Python modules/functions that were used in this study.

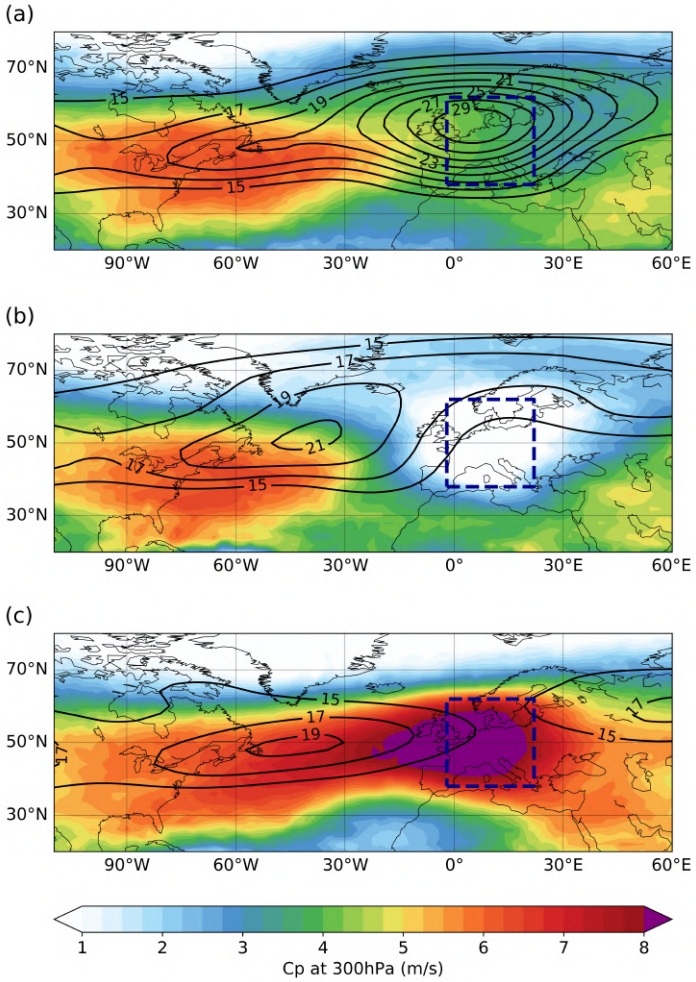

Fig. 5.19: *(a) Composites of c_p (color shading) and E (black contours) over the (a) 727 days that occupy the regime of high E values (orange rectangle in Fig. 5.16), (b) 719 days that occupy the regime of low E and low c_p values (red rectangle in Fig. 5.16) and (c) 837 days that occupy the regime of low E and high c_p values (blue rectangle in Fig. 5.16).*

Table 5.1: *Number of Central European temperature extremes for each type and season. The values correspond to the number of extreme events and the parentheses show the total number of extreme days.*

	DJF	MAM	JJA	SON	total
Days with c_p defined	3507	3529	3158	3470	13664
Short-lived hot extremes	130 (176)	97 (137)	109 (153)	113 (150)	449 (616)
Persistent hot extremes	26 (130)	35 (181)	21 (115)	31 (165)	113 (591)
Short-lived cold extremes	72 (103)	93 (140)	92 (139)	85 (123)	342 (505)
Persistent cold extremes	31 (173)	30 (159)	28 (130)	31 (172)	120 (634)

Table 5.2: *List of Python modules used in this study. In the Notes column we indicate their specific application.*

	Module (version)	Notes	More info
1	`scipy.fftpack` (1.1.0)	Fast Fourier transform (eq. 2 and 4)	`https://docs.scipy.org/`
2	`scipy.stats.ttest_ind` (1.1.0)	Welch's t-test for the means of two independent samples (Fig. 5.7)	`https://docs.scipy.org/`
3	`sklearn.model_selection.GridSearchCV` (0.19.1)	Exhaustive search over specified parameter values for an estimator using a k-fold cross-validation (section 5.5, Figs. 5.7 and 5.8)	`https://scikit-learn.org`
4	`sklearn.neighbors.KernelDensity` (0.19.1)	Kernel Density Estimation with Gaussian kernels of cross-validated bandwidth (section 5.5, Figs. 5.7 and 5.8)	`https://scikit-learn.org`

Chapter 6

Medium-range forecast biases in Rossby wave packet properties

6.1 Introduction

Given the findings presented in previous chapters, it becomes clear that properly representing the RWP properties in numerical weather prediction (NWP) models is crucial for the practical predictability of temperature extremes. Motivated by that, the performance of ECMWF medium-range forecasts regarding the RWP amplitude and phase velocity is evaluated in this chapter. The availability of local RWP diagnostics allows such an evaluation and the identification of inter-regional and seasonal variability in possible forecast biases.

Recent studies have investigated the performance of NWP models when it comes to the upper-tropospheric circulation and the Rossby waves structure. Gray *et al.* (2014) found that the extratropical tropopause sharpness decreases with forecast lead time due to a combination of diabatic processes underrepresentation, weak humidity gradients and numerical aspects (limited resolution, advection scheme) of the model (see also, Saffin *et al.* 2017). Along the same line, Martínez-Alvarado *et al.* (2016) reported that misrepresenting the PV modification within warm conveyor belts can also result in forecast errors in Rossby waves. Finally, using a single-layer quasi-geostrophic model Harvey *et al.* (2016) and Harvey *et al.* (2018) suggested mechanisms through which an underestimation of tropopause sharpness and the associated broadening of PV fronts and decrease in jet speed may result in decreased Rossby wave phase velocity and amplitude.

6.2 Data and methods

In this chapter, ECMWF operational forecasts from the THORPEX International Grand Global Ensemble (TIGGE) database (Bougeault *et al.* 2010) are used. In particular, the deterministic forecast of 300 hPa u and v have been retrieved on a grid of $2^\circ \times 2^\circ$ horizontal resolution, initialized every 12 hours in the period from January 2013 to December 2018. Each forecast run is validated every 6 hours from 0 to 240 hours. This 6-year dataset corresponds to 4382 forecast runs, thus providing a sufficiently

large sample for the evaluation of biases. During this period, ECMWF has used the Integrated Forecasting System (IFS) model cycles 38r1 to 45r1*.

The retrieved v forecast field is spatiotemporally smoothed as described in steps ii) and iii) of section 5.2 (the 24-hour moving average is applied to the temporal evolution of each individual forecast run). Given the smoothed v field, RWP amplitude (E), zonal angular frequency (ω), zonal angular wavenumber (k), and phase velocity (c_p) are diagnosed as described in section 5.3.

Given the fact that the observed and forecast RWPs at a given validation time are generally not overlapping (displacement errors are expected to grow with lead time), it is not straight forward to evaluate the forecast performance of the aforementioned field in individual time steps. Therefore, forecasts and reanalysis are compared in terms of their temporal mean fields. In this regard, the 12-hourly 2013–2018 climatological mean field of n-day forecasts, n being the lead time in days, is compared to the corresponding ERA5 reanalysis field, which I assume to be close to the real conditions at any given day. The reanalysis and n-day forecast climatologies for each grid point are computed as the time mean over the values that rank within the inter-quartile range of the time series. This way, the effect of outliers is diminished.

In section 6.3, the mean biases over the entire period (January 2013 to December 2018) in the Northern Hemisphere are presented. In section 6.4, the seasonal variability of the biases is briefly investigated and, finally, section 6.5 provides a summary of the main findings in this chapter.

6.3 Mean biases in RWP amplitude and phase velocity

Figure 6.1 shows the Northern Hemisphere inter-quartile mean of E and c_p in the 2013–2018 ERA5 reanalysis, as well as the deviation of the deterministic 3-, 5-, and 7-day forecast inter-quartile means from the reanalysis of the respective field. A decreasing amplitude (E) with lead time is evident in the subtropical latitudes (Figs. 6.1b–d). In most cases this underestimation occurs to the south of the maximum E bands and grows with lead time. An exception to this pattern occurs in the N. Atlantic jet entrance, where an overestimation of E builds up and becomes more evident in the 7-day forecast. When it comes to c_p, there is an overestimation (c_p is too high in the forecast) in the whole N. Pacific jet that grows with lead time and an underestimation (c_p is too low in the forecast) in the N. African – Asian subtropical jet that is evident from the 3-day forecast already (Figs. 6.1f–h). In addition, there is a weak underestimation of c_p in the N. Atlantic upstream of Europe. The sign in the c_{gx} bias patterns resemble those of c_p but the general pattern seems more noisy (not shown). Finally, there is no clear pattern in the c_{gy} forecast bias (not shown).

Figure 6.2 focuses on the observed bias in c_p. According to the definition of phase velocity (sections 1.1 and 5.3.2), it corresponds to the ratio of the angular frequency (ω) to the zonal wavenumber (k). It is then worth exploring whether the bias in c_p is associated with misrepresentations in ω and/or k. In this regard, Figs. 6.2b–d

*For detailed documentation: `https://www.ecmwf.int/en/forecasts/documentation-and-support/changes-ecmwf-model/ifs-documentation`

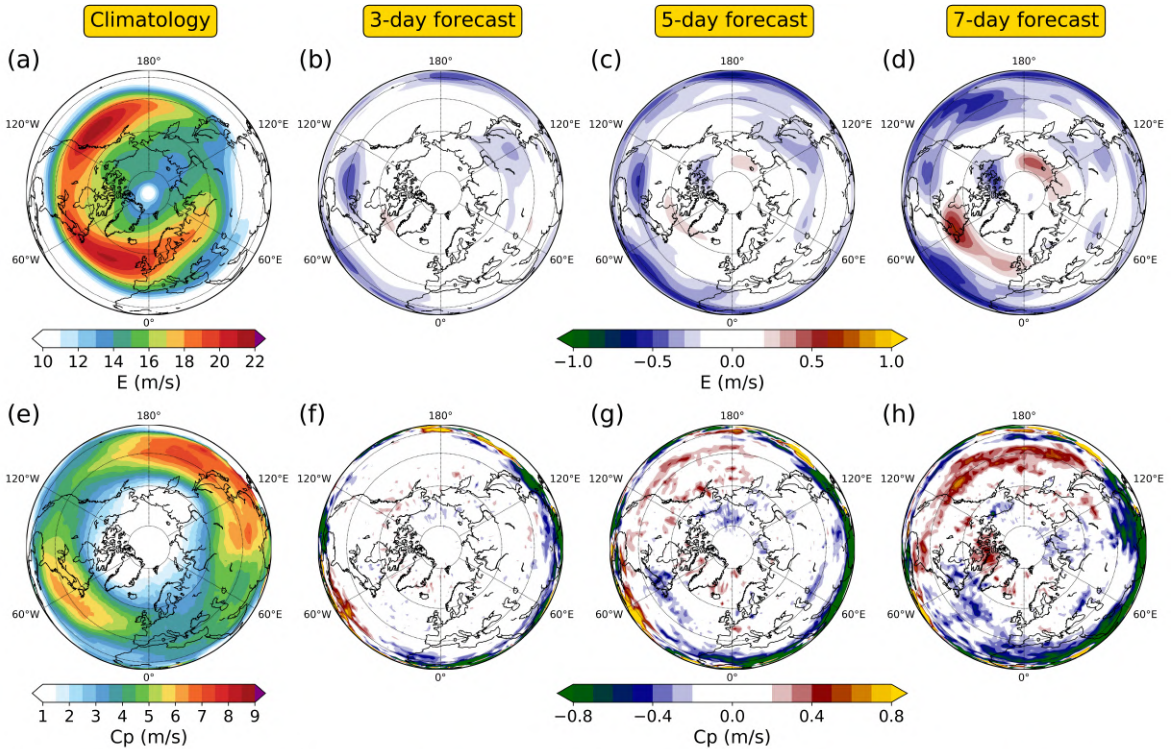

Fig. 6.1: *Medium-range forecast biases in Northern Hemisphere RWP properties. The first column of panels shows the inter-quartile mean of E (a) and c_p (e) in the 2013–2018 period based on the ERA5 reanalysis. The second column of panels (b,f) shows the deviation of the deterministic 3-day forecast inter-quartile mean from the reanalysis of the respective field. The third (c,g) and fourth columns (d,h) correspond to the 5-day and 7-day forecast inter-quartile means respectively.*

reveal that biases in ω grow with lead time forming a similar pattern to the ones of c_p. The biases in k show an overestimation at the high latitudes but are generally weak relative to the verifying reanalysis climatology (Figs. 6.2e–h). Therefore, the bias pattern in c_p is dominated by errors in the rate at which the troughs and ridges propagate downstream, rather than errors in their wavelength.

Furthermore, the phase velocity of Rossby waves in a single-layer barotropic flow is linearly dependent on the zonal background flow (eq. 1.12). Figures 6.2j–l show the biases in zonal wind speed (u), which serves here as a proxy for the jet speed. Evidently, there is a growing underestimation in both the subtropical jet and the N. Atlantic eddy-driven jets. Although RWPs are not advected by the time mean wind, this pattern is consistent with the underestimation of c_p in these areas. In contrast, in the Eastern N. Pacific region (120°E -180°), the wind speed is underestimated, but ω and c_p are overestimated. This behaviour implies that at this region the rate at which the troughs and ridges propagate relative to the background flow is overestimated. The modeling study of Harvey *et al.* (2016) provides further insight in these aspects.

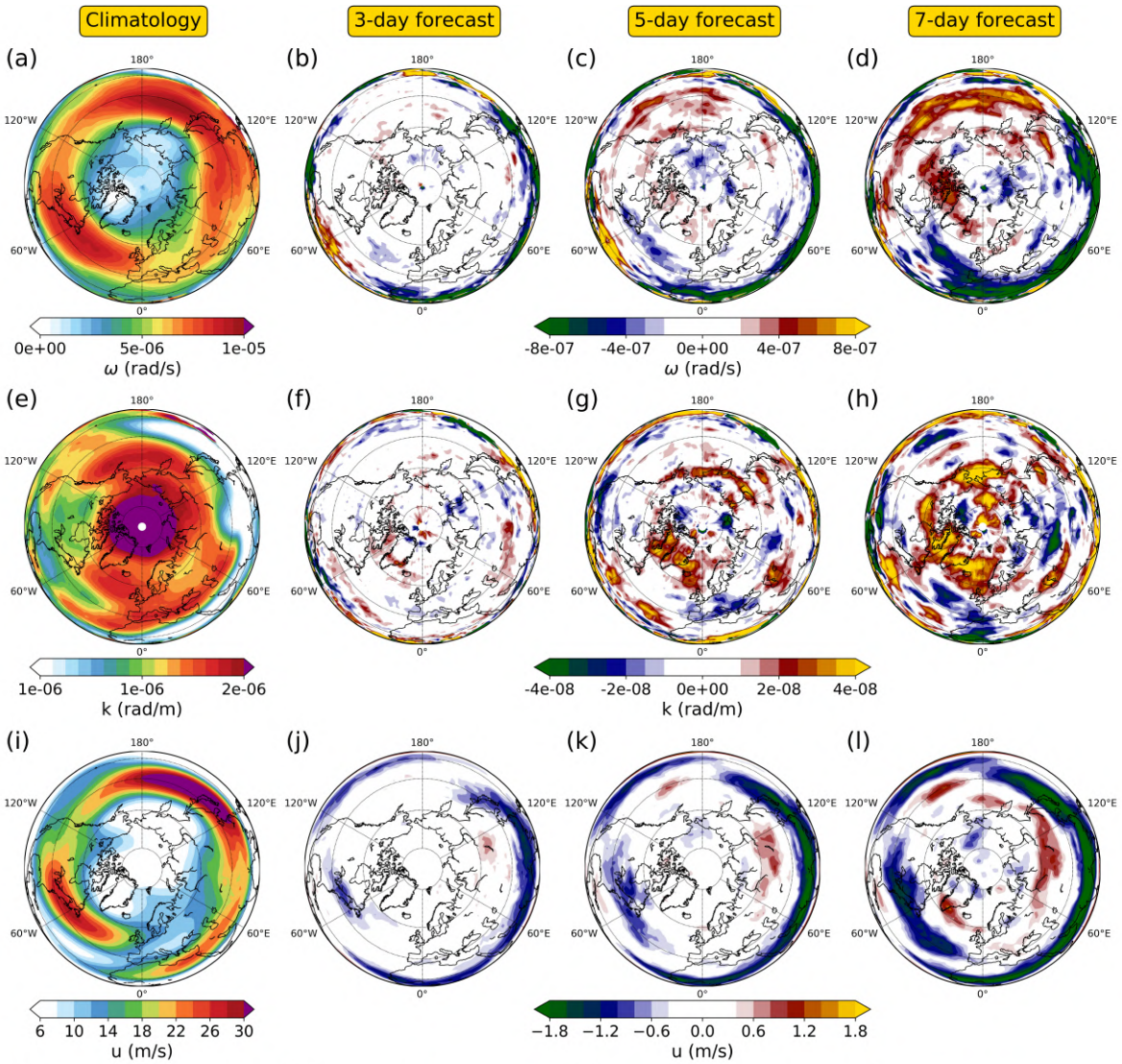

Fig. 6.2: *Medium-range forecast biases in Northern Hemisphere RWP properties and the jet stream. The first column of panels shows the inter-quartile mean of* ω *(a),* k *(e), and* u *(i) in the 2013–2018 period based on the ERA5 reanalysis. The second column of panels (b,f,j) shows the deviation of the deterministic 3-day forecast inter-quartile mean from the reanalysis of the respective field. The third (c,g,k) and fourth columns (d,h,l) correspond to the 5-day and 7-day forecast inter-quartile means respectively.*

6.4 Seasonal variability in the RWP amplitude and phase velocity biases

This section provides insight in the seasonal variability associated with the aforementioned biases. Figures 6.3 and 6.4 are equivalent to Fig. 6.1, but show the E and c_p biases for DJF and JJA respectively. Therefore, the sample in each case is now decreased and consists of the 6 seasons in the 2013–2018 period.

The decrease in E with lead time in JJA extends over most parts of the subtropics and midlatitudes (Figs. 6.4b–d), but this is not the case for DJF. During winter there is a band of rapidly increasing E overestimation that extends from Eastern N. America to Western Europe (Figs. 6.3b–d). Another band of E overestimation is found over the N. Pacific, while Western N. America, Scandinavia, Eastern Europe and parts of the subtropics are associated with a growing underestimation in E with lead time. Given the climatological pattern of E (Fig. 6.3a), these observations imply that the band of maximum RWP amplitudes at the N. Atlantic jet exit region gets narrower with lead time. This behavior may suggest that RWPs in their mature stage follow a more zonal track, rather than a poleward or equatorward one. When it comes to c_p, as in the mean biases of the entire period, there is an underestimation in the subtropical jet in both seasons, while areas of overestimation are found in the midlatitudes during summer and the N. Pacific during winter (Figs. 6.3f–h and 6.4f–h).

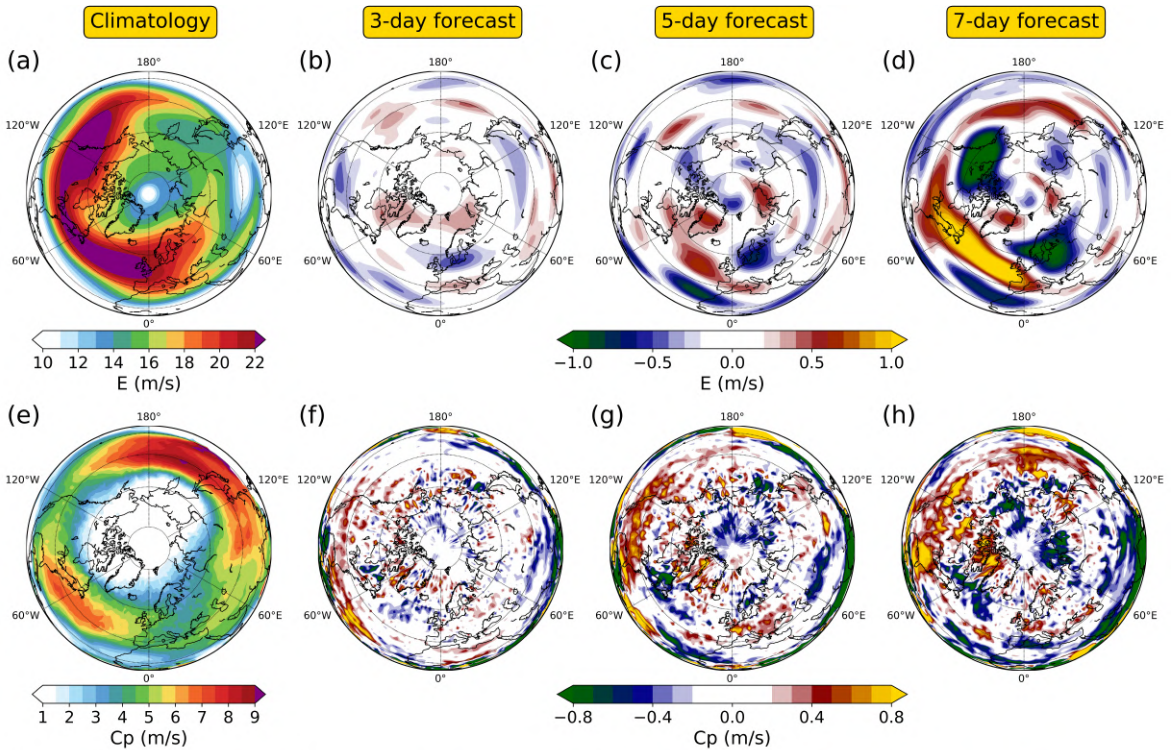

Fig. 6.3: *Same as Fig. 6.1 but for medium-range forecasts in DJF only.*

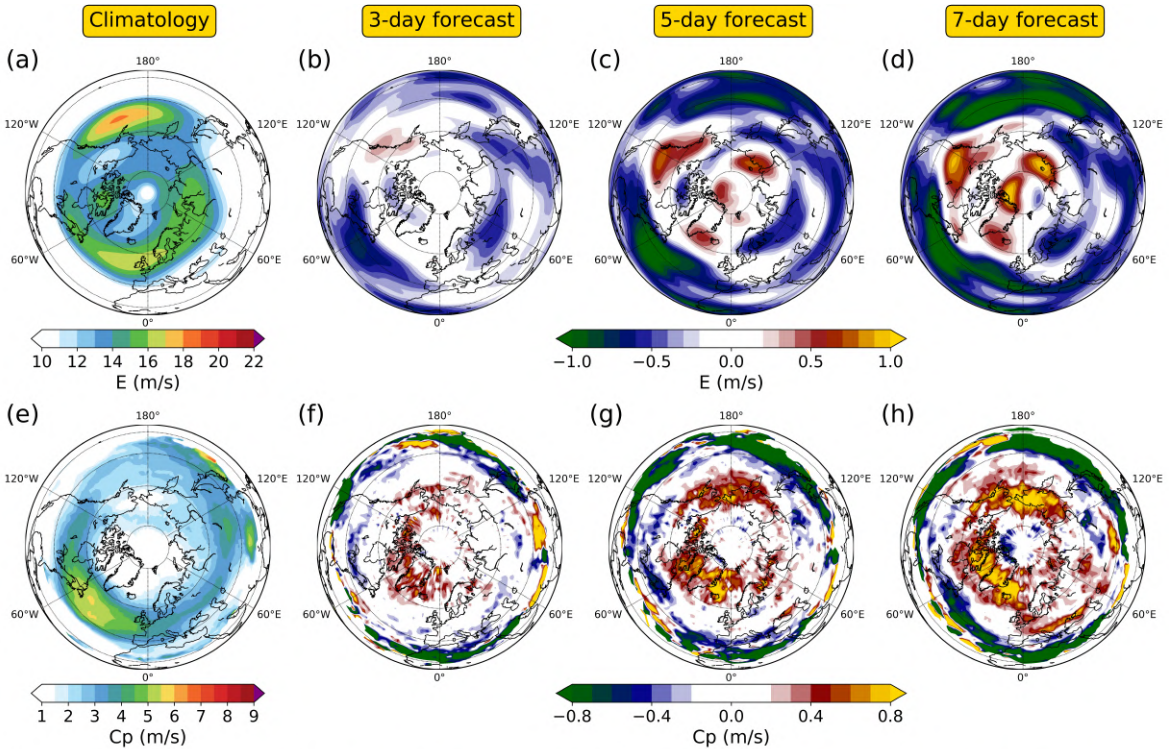

Fig. 6.4: *Same as Fig. 6.1 but for medium-range forecasts in JJA only.*

6.5 Summary and further remarks

Medium-range forecast biases in the Northern Hemisphere RWP properties were investigated in this chapter using 6 years of ECMWF operational forecasts (2013–2018). Distinct bias patterns with seasonal and inter-regional variability were evident for RWP amplitude and phase velocity. Key outcomes in these patterns include the following:

- An overestimation of c_p that grows with lead time is found in the N. Pacific and is more evident in the mean 7-day forecast bias over the entire period (Fig. 6.1h). This bias cannot be entirely explained by the bias in zonal wind and biases in zonal wavenumber are not significant.

- During JJA, E is underestimated in most parts of the subtropics and midlatitudes. In addition, c_p is overestimated in the mid-to-high latitudes, and underestimated in the subtropics. Based on the findings in previous chapters, this behavior may have implications for the representation of summer heat waves over Europe. In particular, a faster propagating ridge of lower amplitude in the forecast would imply heat waves of lower intensity and duration (see section 5.5).

- During DJF, a narrow band of overestimated E is found over the N. Atlantic, upstream of Europe. This bias seems to grow rapidly with lead time and suggests an overly zonal RWP propagation.

- The observed seasonal variability in the medium-range forecasts of the upper-tropospheric circulation requires further attention. At first sight, it suggests that

these biases are not dominated by imperfections in the numerics of NWP models, but physical processes with pronounced annual cycle are also at play.

- A common feature in the presented bias patterns is the lack of zonal symmetry. This emphasizes the added value of employing diagnostics of local RWP properties in the evaluation of medium-range forecasts.

Although in several cases the sign of the errors formed a spatially coherent pattern, it is not certain whether the presented biases are systematic (characteristic of every forecast run) or episodic (in general weak, but at times strong). Further investigations would be needed in order to shed light on this issue and suggest the physical and numerical processes that lead to the observed biases. As an example, future studies may explore whether the errors preferentially amplify in specific weather regimes (e.g. blocking pattern to the northwest of Europe) and to investigate the effect of the identified biases on the predictability of temperature extreme occurrence, magnitude, and duration (as suggested in section. 4.3).

It should be noted that the magnitudes of the presented biases are in general decreased compared to older IFS model cycles. In fact, the analysis presented here was repeated for the IFS 31r2 (operational from late-2006 to mid-2007) deterministic forecasts with the ERA-Interim reanalysis as initial conditions for the period 1979–2016 (Berrisford *et al.* 2009; these data were also used in the analysis of chapter 4). The patterns of the biases were somewhat different, but their magnitudes were systematically larger in most parts of the Northern Hemisphere. In the quest of exploring the predictability of local weather and the physical or numerical processes limiting it, it is important to keep investigating and reporting on the biases in the upper-tropospheric circulation, as new upgrades in the NWP models are implemented.

Chapter 7

Conclusion

7.1 Summary

Driven by the rotation and sphericity of the Earth, Rossby waves are a dominant feature of the upper-tropospheric circulation. The succession of northerly and southerly components in the midlatitude flow at scales of a few thousand kilometers is a manifestation of Rossby waves that makes them highly relevant for surface weather. Their typical evolution in the real atmosphere takes the form of eastward propagating wave packets (RWPs) that, as the term implies, are not circumglobal but confined in a longitudinal range. This observation necessitates the development of diagnostic methods that can identify and investigate the RWP properties locally in space and time.

The work presented here dealt extensively with the development of local diagnostic methods that were used to shed light on important properties of the RWP evolution. Such properties include the local amplitude, wavenumber, phase velocity, and group velocity of RWPs. The diagnosis of the first three involved computing the analytic signal of a filtered upper-tropospheric meridional wind along latitude circles (sections 3.2 and 5.3). The diagnosis of the group velocity vector field followed the same principle on the envelope function of RWP objects (section 5.3). It was demonstrated that these properties generally vary between RWPs, but also exhibit inhomogeneities within individual RWPs, which justified the need to develop local diagnostic methods for the investigation of RWPs. In terms of their climatological imprint, a distinct seasonal and inter-regional variability in the aforementioned RWP properties was found in the analysis of section 5.4. These global climatologies revealed several interesting aspects of the upper-tropospheric large-scale circulation characteristics in both hemispheres.

With the aforementioned tools, the role of RWPs in the occurrence, magnitude, and duration of temperature extremes were investigated. An improved understanding in this respect was achieved through case studies of major heat waves of the past, but also statistical analyses in samples that included all hot and cold extremes during the past 4 decades in parts of Europe. Key outcomes from these analyses are listed below:

- The probability for a temperature extreme in Central Europe is significantly larger during days with a strong RWP amplitude (section 3.3.1). On a day with an extreme RWP amplitude (above the 90^{th} percentile), the probability for a warm/cold temperature extreme is approximately 40%. Such a good connec-

tion was also found for many regions in the Northern Hemisphere midlatitudes (section 3.3.2).

- The advantage of identifying and following the evolution of RWPs was also revealed in case studies of the 2003 and 2010 heat waves in Western Europe and Russia respectively (section 3.4). Although both events were equally severe for the society, their meteorological lifetime was in many regards different, suggesting that the mechanisms linking RWPs and temperature extremes are case dependent. In the 2003 case, the approach of a single unseasonably strong RWP led to positive temperature anomalies over most parts of Western Europe, which then rapidly turned extreme driven to a large extent by the quasi-stationarity of the associated ridge. On the other hand, the 2010 heat wave was characterized by a continuous succession of strong RWPs over the North Atlantic and Europe and a gradual build-up of anomalously warm temperatures in Western Russia that were sustained for 3 weeks more than in the 2003 case ($\sim$5 weeks in total).

- Noteworthy, at any given instance in the 2003 and 2010 heat waves RWP activity was conspicuous and non-circumglobal. Related to that, all analyses in chapter 3 indicated that the RWP amplitude is much better linked to temperature extremes than the circumglobal Fourier amplitudes that instead obscure the spatiotemporal evolution of upper-tropospheric waviness (e.g., Petoukhov *et al.* 2013b).

- The role of RWPs was further emphasized in an investigation of Southeastern European hot and cold extremes (chapter 4). Distinguishing between short-lived and persistent extremes of each season revealed differences in the spatiotemporal evolution of the upper-tropospheric flow. A far-upstream precursor signal in the form of RWPs was evident for several types of temperature extremes. A clear feature of the persistent ones was the low phase velocity, as inferred from the employed composite Hovmöller diagrams. In several cases, a preferential in-phase RWP propagation with pronounced downstream development was evident in the days preceding the extremes.

- The important role of RWP amplitude and zonal phase velocity in the occurrence and duration of Central European temperature extremes was verified in a quantitative fashion in chapter 5. It was shown that the occurrence of both hot and cold extremes is associated with an enhanced RWP amplitude, but for the persistence of the events a below-normal phase velocity in the trough–ridge pattern aloft is essential.

These findings suggest that during a temperature extreme, the planetary-scale flow in which the troughs and ridges develop is crucial. Regarding heat waves, their onset, severity and duration is influenced by the amplitude and phase velocity of the associated ridge as it is reflected in the upper-tropospheric meridional wind field. This ridge sets a stage that favors meteorological conditions that can lead to extreme near-surface temperatures (e.g., high pressure, clear skies, subsidence, excess surface heat fluxes, decreased latent cooling etc). The ridge in turn, is not undergoing a purely independent life cycle, but is modulated by the larger scale RWP that embodies it.

The aforementioned observations corroborate the need for local diagnostics and emphasize their advantage in revealing aspects of the often complex structure and incoherent propagation of RWPs. Motivated by the demonstrated role of RWP properties in temperature extremes, chapter 6 focused on medium-range forecast biases of the Northern Hemisphere RWP properties using 6 years of ECMWF operational forecasts (2013–2018). The detected bias patterns in RWP amplitude and phase velocity suggest possible implications for the practical predictability of the temperature extremes occurrence and duration.

7.2 Outlook

The work presented here contributes to the overarching goal of improving our understanding of RWPs and temperature extremes. The development of new tools for the diagnosis of RWP properties provides a powerful addition for the investigation of their crucial role in temperature extremes. Moreover, the novel diagnostic of local dominant wavenumber based on a wavelet analysis of meridional wind (section 5.7.3; Appendix A) was successfully employed for the diagnosis of RWPs based on the local wave activity (Ghinassi *et al.* 2018). Adding to the presented results, a collaboration with Philipp Zschenderlein and Andreas Fink (Karlsruhe Institute of Technology) on a case study of the 2016 heat wave (Fig. 1.4) proved fruitful in combining processes across scales that collectively determine the spatiotemporal characteristics of heat waves (Zschenderlein *et al.* 2018). Ongoing work also involves the effects of RWP characteristics in conjunction with moisture transport and orographic lifting in Northern Italy precipitation extremes (Grazzini *et al.* 2019). Given the fact that the concentration of greenhouse gases continues to rise, these studies contribute to the continuing efforts of the community in investigating the characteristics of weather extremes in the past, current and projected climate.

Based on the above, new avenues open up for future research on the processes that affect the evolution of RWPs, as well as research on their implications for the occurrence and predictability of weather extremes. Ideas for studies that could benefit from the presented methods and build on the outcomes of this work were discussed in the concluding remarks of each chapter (sections 3.5, 4.4, 5.6, and 6.5). An interesting question to be addressed is whether and how do RWPs modulate the evolution of the individual eddies that comprise them. If all the eddies within a well-shaped RWP propagate with similar phase velocities, this suggests that RWPs modulate the evolution of the individual eddies they embody (e.g. the interplay between a warm conveyor belt outflow and the downstream ridge). It is crucial therefore to study the factors that determine the three-dimensional evolution of RWPs and investigate their two-way interactions with individual eddies. Regarding temperature extremes, continuing studies in the combined role of RWPs and other relevant physical processes would enable the investigation of which scales and specific processes limit the predictability of their onset, intensity, duration, and spatial extent

Appendix A

Local wavenumber through wavelet analysis

This appendix is adapted as is from the peer-reviewed article entitled: "Local Finite-Amplitude Wave Activity as a Diagnostic for Rossby Wave Packets" by P. Ghinassi, G. Fragkoulidis, and V. Wirth that was published in the December 2018 issue of the Monthly Weather Review (Ghinassi et al. *2018)* [*]*. The text is integrated as is into the dissertation and the section and figure numbers are adjusted accordingly. The references are listed in the unified bibliography at the end of the dissertation.*

Here we describe our algorithm designed to find a local (in space) zonal wavenumber. The analysis is based on the wavelet transform of the meridional wind v for each given latitude circle on the selected isentrope. The following steps are performed.

(i) The basis function for our wavelet analysis is the complex-valued Morlet wavelet as a function of longitude,

$$\Psi_0(\lambda) = (\pi\sigma_\lambda^2)^{-\frac{1}{4}}\, e^{is_0\lambda}\, e^{-\frac{\lambda^2}{2\sigma_\lambda^2}}\,, \tag{A.1}$$

where s_0 is the center wavenumber and σ_λ is the shape parameter (Yi and Shu 2012). This wavelet is suitable for our purposes, partly because its real part resembles the RWPs that we are trying to analyze. The parameters s_0 and σ_λ were taken to be 6 and 0.7; this choice guarantees important properties of the Morlet wavelet, namely its admissibility (Farge 1992) and a good compromise between wavenumber and space localization.

(ii) The meridional wind field is filtered by applying a Fourier series expansion in longitude and discarding zonal wavenumbers greater than 20.

(iii) The continuous wavelet transform in the zonal direction yields the following

wavelet coefficients,

$$W_n(L) = \sum_{n'=0}^{N-1} v_{n'} \Psi_0^* \left[\frac{(n'-n)\Delta\lambda}{L} \right] , \tag{A.2}$$

where L denotes the scale, n $(= 0, 1, \ldots N-1)$ numbers the grid points in the zonal direction, v_n is the meridional wind at grid point n, $\Delta\lambda$ is the grid spacing in the zonal direction, and the asterisk denotes complex conjugation (Torrence and Compo 1998). At every grid point, $W_n(L)$ is evaluated for various values of the scale L, which effectively probe the different spatial scales in the neighborhood of this grid point. Note that edge effects are not an issue in our application since we are dealing with a periodic domain.

For an efficient computation, we actually perform the convolution on the right hand side of (A.2) in Fourier space. The wavelet coefficients can, thus, be written as

$$W_n(L) = \sum_{s=0}^{N-1} \hat{v}_s \hat{\Psi}^*(Ls) e^{isn\Delta\lambda} , \tag{A.3}$$

where s is the zonal wavenumber, $\hat{v}_s$ represents the discrete Fourier transform of v_n, and

$$\hat{\Psi}(Ls) \coloneqq C\ \hat{\Psi}_0(Ls) = C\ (4\pi\sigma_\lambda^2)^{\frac{1}{4}}\ e^{\frac{-\sigma_\lambda^2 (Ls - s_0)^2}{2}} \tag{A.4}$$

is the Fourier transform of the Morlet wavelet (Yi and Shu 2012), multiplied by the normalization factor $C = (2\pi L/\Delta\lambda)^{\frac{1}{2}}$ to achieve unit energy at each scale (Torrence and Compo 1998).

(iv) The two-dimensional *wavelet power spectrum* is then obtained by computing $|W_n(L)|^2$ at every grid point for a finite number of scales ($L_m = L_0\, 2^{m\delta_m}$, $m = 0, 1, \ldots 300$, with $L_0 = 0.2$ being the smallest resolvable scale and $\delta_m = 0.02$ the scale resolution). Following Liu *et al.* (2007), each value of the power spectrum is then divided by its respective scale in order to partially account for the dispersion (in scale) bias at small scales.

(v) The above set of scales is converted to the associated zonal wavenumbers through $s_m = 2\pi/(fL_m)$ where $f = 4\pi/\left(s_0 + \sqrt{2 + s_0^2}\right)$ (Torrence and Compo 1998). At each grid point n of the resulting $|W_n(s_m)|^2$ spectrum, the wavenumber that corresponds to the maximum power constitutes the *local dominant wavenumber* s_d of the respective longitude λ.

(vi) Steps (iii)–(v) are repeated for every latitude, eventually providing the two-dimensional field of local dominant wavenumber $s_d(\lambda, \phi)$.

(vii) Finally, we apply a filter to $s_d(\lambda, \phi)$ by convolution with a Hann-window (Harris 1978) of 21° (full width at half maximum) in the zonal direction, followed by a 7° Hann window in the meridional direction.

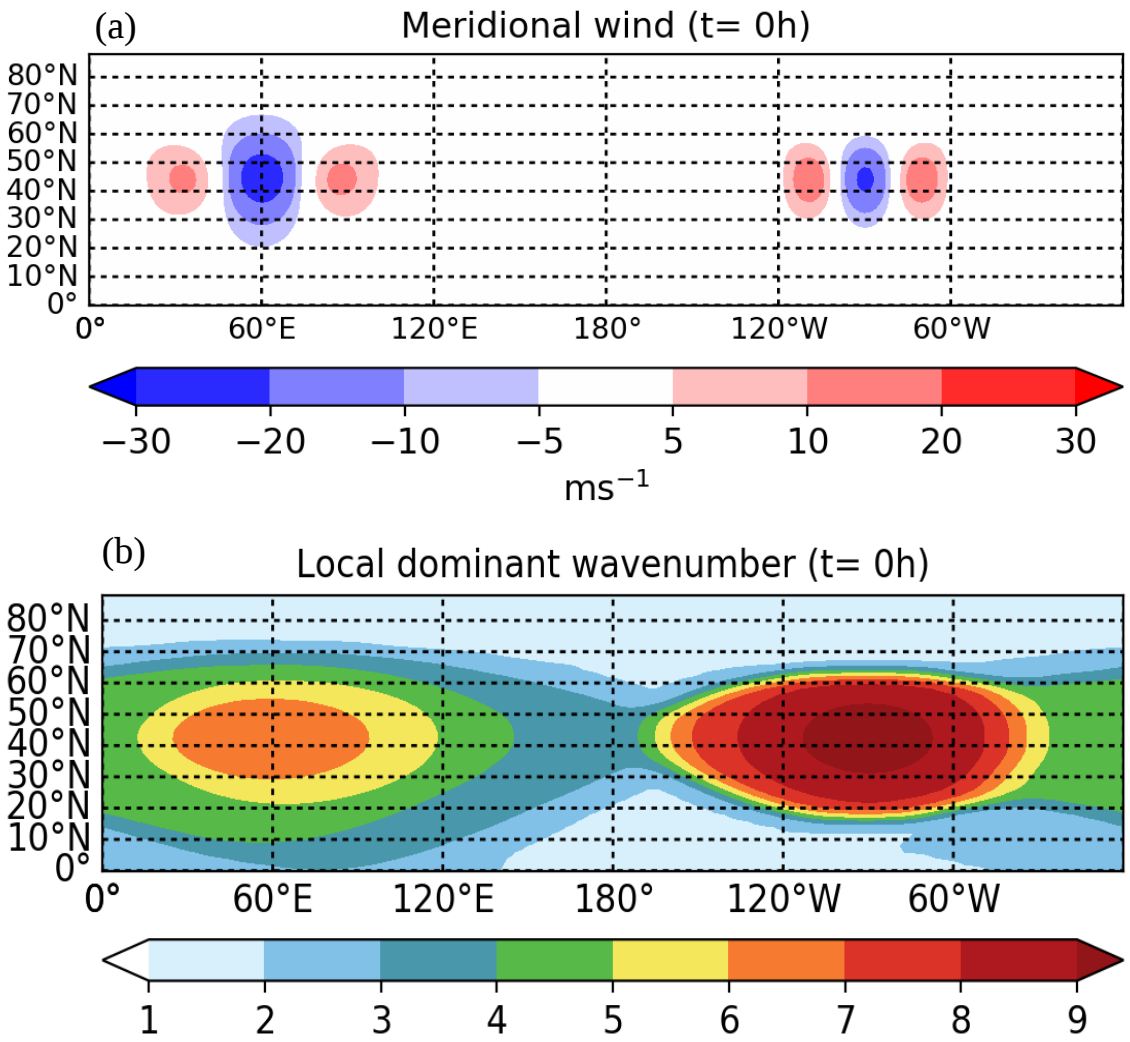

Fig. A.1: *Initial state of the barotropic model simulation: (a) meridional wind v (color shading, in* $\mathrm{m\ s^{-1}}$ *) and (b) local dominant wavenumber (color shading, dimensionless) from wavelet analysis.*

As an example, we show in Fig. A.1 the field of the meridional wind and the associated locally dominant wavenumber for the initial state of our barotropic simulation. Remember that the two wave packets were initialized with carrier wavenumbers 6 and 9, respectively. Apparently, our algorithm does a good job in reproducing these wavenumbers in the center of the respective wave packets, with a smooth transition between them. The performance for the real flow situation of 0000UTC 11 April 2011 is shown in Fig. A.2. This field is more complex, but again there seems to be a reasonable compromise between local detail and overall representativeness in the field $s_d(\lambda, \phi)$.

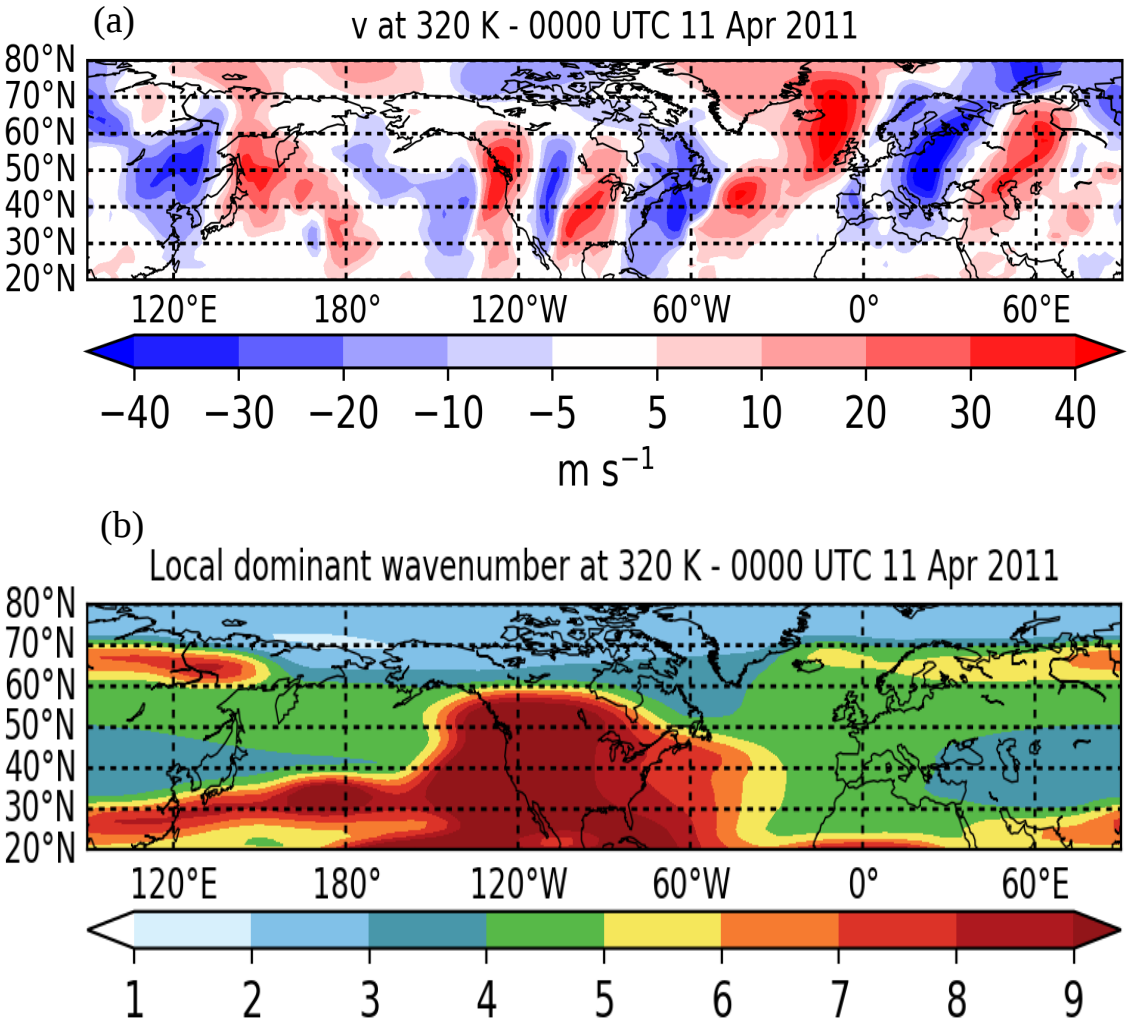

Fig. A.2: *Same analysis as in Fig. A.1, but here for the flow on the 320 K isentrope on 0000 UTC 11 April 2011.*

List of Figures

1.1 Schematic depiction of the Rossby wave mechanism on a β-plane. See description in the text. 3

1.2 Schematic depiction of a one-dimensional sinusoidal Rossby wave (gray dashed line) and a Rossby wave packet (blue solid line) modulated by an envelope (E; red solid line). 5

1.3 Upper-tropospheric circulation properties on 1200 UTC 20 August 2016. (a) PV anomaly (color shading; in PVU) and isoline of 2 PVU (black contour) at 330 K. (b) Color shading depicts meridional wind anomaly at 300 hPa (in ms^{-1}). Yellow (green) hatching represents areas where temperature anomaly at 850 hPa is greater (less) than the 95^{th} (5^{th}) percentile. (c) Color shading depicts temperature anomaly at 850 hPa (in K) and black contours represent geopotential height anomalies at 500 hPa. (d) RWP amplitude at 300 hPa (in ms^{-1}). (e) Wind velocity (color shading; in ms^{-1}) and wind streamlines at 300 hPa. 6

1.4 Same as Fig. 1.3, but for 1200 UTC 23 August 2016. 7

1.5 Schematic depiction of the main RWP properties. Shaded color represents meridional wind velocity in the latitude–longitude domain (yellow arrows show direction). The gray line indicates the corresponding envelope, E, along a latitude circle. The schematic involves two successive timesteps with the initial time step represented by the dashed contours. Phase velocity, c_p, and group velocity, c_g, are indicated by the black and green arrows respectively. 8

1.6 Daily mean temperature anomaly at 850hPa on 8 August 2003. 9

1.7 Left: Hovmöller diagram illustrating the upper tropospheric circulation during the 2003 heat wave (ERA-Interim data). The black contours depict RWP amplitude at 300hPa (every 4ms^{-1}from 22 to 38ms^{-1}). Color shading represents the meridional wind anomaly at 300 hPa; blue for southward anomaly and red for northward. The two fields are meridionally averaged over a 20° latitude band which self-adjusts (within the 30°N –70°N band) to those latitudes in which the highest RWP amplitudes occur. The time resolution is 6 hours. A weak bivariate interpolation using cubic Hermite splines is applied in view of smoother RWP contours. The slope of the drawn green dashed arrow indicates the group velocity of the eastward propagating RWP. Right: The red line depicts the time series of the normalized temperature anomaly at 850hPa for the same time period (given in standard deviations), averaged — with a weighting to the cosine of latitude — over the [38°N –58°N , 6°W –14°E] area (red rectangle in the lower right corner). Orange shading indicates that at the respective time the temperature anomaly exceeds the 95^{th} percentile of JJA temperature anomalies in the period 1979–2016 (blue dashed line). 11

1.8 Same as Fig. 1.7 but for the 2016 compound heat wave in Western Europe. The normalized temperature anomaly at 850 hPa in the right panel is now averaged over the [35°N –55°N , 11°W –15°E] area (red rectangle in the lower right corner). Orange shading corresponds to temperature anomaly values in excess of the 90^{th} percentile for the months of August and September (blue dashed line). Adapted from Zschenderlein *et al.* (2018). 12

1.9 Satellite imagery of Europe from the Moderate Resolution Imaging Spectroradiometer (MODIS) instrument on board NASA's Terra satellite†on: (a) 8 August 2003 and (b) 23 August 2016. 13

2.1 Mean annual cycle calculation and smoothing. 16

2.2 Wavelength limits in the zonal filtering of meridional wind at 300 hPa. The blue and red lines show for each latitude the wavenumber limits that correspond to wavelengths of 2000 km and 10000 km respectively. 17

2.3 Example of zonal wavelength restriction to 2000–10000 km. The upper panel shows a Tukey window of α=0.3 (70% of the window has a weight of 1 and 30% is cosine-tapered) in the wavenumber domain. At 50°N , the 2000–10000 km restriction corresponds to wavenumbers of approximately 2.6–12.9. As per our methodology, the Tukey window limits are placed at wavenumbers 1.1 and 14.4 and wavenumbers that are close to the tails will have a lower contribution. For example, the power at wavenumber 14 is multiplied by a factor of 0.1 and the power at wavenumber 13 by a factor of 0.8. The middle panel shows the effect of the Tukey window in the Fourier spectrum of an exemplary meridional wind latitude circle. The lower panel shows the smoothing effect in the signal itself. 18

2.4 Spatial filtering example on 1200 UTC 24 August 2016. a) Original meridional wind field, b) zonal restriction to 2000–10000 km, c) zonal restriction to 2000–10000 km followed by meridional convolution with a Hann window of 7° width at half maximum. In all panels the yellow contour corresponds to E=20ms^{-1}. 19

3.1 (a) Map of the 10-day mean (2–12 June 1988) meridional wind anomaly v' (colour, in ms^{-1}) at 300 hPa; (b) meridional wind anomaly v' at 50°N (green line, in ms^{-1}). 22

3.2 RWP diagnosis example for 6 August 2003 0000 UTC. (a) Map of the meridional wind anomaly v' (colour, in ms^{-1}) at 300 hPa; (b) meridional wind anomaly v' at 50°N (green line, in ms^{-1}) and its envelope E (blue line, in ms^{-1}); (c) map of the envelope field E (RWP amplitude, ms^{-1}). 25

3.3 Analysis of the temporal correlation between daily mean RWP amplitudes at 300 hPa and temperature anomalies at 850 hPa for the 36–56°N , 0–20°E region in Europe during JJA. (a) Scatter plot of normalized $|T'|$ against normalized E. The colour shading depicts a kernel-density estimate using Gaussian kernels. The vertical dashed lines indicate specific quantiles of the values for E separating the data in 10 equally populated bins. The horizontal blue line depicts the 90^{th} percentile of the temperature distribution. The Spearman's rank correlation coefficient is shown in the yellow box. (b) Percentage (%) of temperature extremes (daily average $|T'| > 90^{th}$ percentile) in each E-bin, where each E-bin is represented on the abscissa by its median. The red shading shows the statistical uncertainty $\Delta P_{\mathrm{ex}}(E)$ of each value. (c), (d) Same as (a) and (b), except that the horizontal axis now refers to the normalized Fourier amplitude instead of RWP amplitude (see text for explanation). 27

3.4 Percentage $\mathcal{P}$ of temperature extremes at 850 hPa for (a) JJA and (b) DJF days with strong upper-tropospheric waviness, as measured by RWP amplitudes. The value for each grid point corresponds to the 20° ×20° region that is centered on it. Grid points with a mean surface pressure below 850 hPa are indicated in black. 29

3.5 Percentage $\mathcal{P}$ of temperature extremes at 850 hPa for (a) JJA and (b) DJF days with strong upper-tropospheric waviness, as measured by Fourier amplitudes. For each grid point, $|T'|$ is averaged over the 20° ×20° region that is centered on it and the corresponding Fourier amplitudes are calculated from the 300 hPa v' field, meridionally averaged over the 20° zonal band that covers the latitudinal extent of the respective region. Grid points with a mean surface pressure below 850 hPa are indicated in black. 30

3.6 Percentage $\mathcal{P}$ of temperature extremes at 2 metres for days with strong RWP amplitude for (a) JJA and (b) DJF during 1979–2015. The value for each grid point corresponds to the 20° × 20° region centered on it. . 31

3.7 Comparison between temperature anomalies at 850 hPa and 2 metres using the 1200 and 1800 UTC average values at two European sites: (a) 40°N , 4°W (Madrid) and (b) 52°N , 0°E (London). The plot contains data for all Northern Hemisphere summer days between 1979 and 2015. The temperature values are expressed in percentiles of the corresponding distribution. The black diagonal depicts the $x = y$ axis. 32

3.8 Concurrence C_2^{850} in percentage between 850 hPa and 2-metre temperature extremes for (a) JJA and (b) DJF during 1979–2015. Grid points with a mean surface pressure below 850 hPa are indicated in orange. . . 32

3.9 HWMId (dimensionless) for (a) 4–14 August 2003 and (b) 2–12 August 2010. The blue dashed lines indicate the latitude band of 850 hPa temperature anomaly averaging in Figure 3.10. 34

3.10 Hovmöller diagrams of temperature anomalies and RWP amplitudes for (a) the 2003 heat wave, and (b) the 2010 heat wave. The colour fill depicts 850 hPa T' (in K), averaged over 40–60°N in (a) and over 44–64°N in (b). The black contours depict the latitudinal average of 300 hPa E (every 2 ms^{-1}, starting from 20 ms^{-1}). The latitudinal averaging for E is explained in the text. 35

3.11 Location of the RWP highest amplitudes ($E = 35$ ms^{-1}) on consecutive days between the 5^{th} and 10^{th} of August during the 2003 heat wave. Each colour contour represents a different day (see legend). 36

3.12 Hovmöller diagrams illustrating the upper-tropospheric flow for (a) the 2003 heat wave, and (b) the 2010 heat wave. The black contours depict the latitudinal average of 300 hPa E (every 2 ms^{-1}, starting from 20 ms^{-1}). The colour fill depicts 300 hPa v'. Finally, the green arrow in (a) indicates the group velocity ($\boldsymbol{c_g}$) of the RWP. 37

3.13 Summer (JJA) 90^{th} percentile of daily mean (a) $|T'|$ at 850 hPa (K), (c) $|T'|$ at 2 metres (K) (e) RWP amplitude (ms^{-1}) and (g) root mean square of the Fourier transform zonal wavenumber 1–15 amplitudes of the 300 hPa v'. (b), (d), (f), (h) Winter (DJF) 90^{th} percentile maps for the respective quantities. The percentiles in (a)–(f) are calculated for the spatial averages of the 20° ×20° regions centered on every grid point. In (g) and (h), the values correspond to v', meridionally averaged in the 20° zonal band centered over every grid point. In (a) and (b) grid points with a mean surface pressure below 850 hPa are indicated in black. . . 43

4.1 Region of T' averaging in the extremes selection. 46

4.2 a) Composite of 850 hPa T' (color shading) at the onset of JJA hot extremes. Stars denote statistically significant values of T' at α=0.10. b) Same as a) but for DJF cold extremes. c) Evolution of 300 hPa v' (color shading) and 500 hPa Z' (blue/magenta contours indicate negative/positive anomalies at ±3, ±6, ±9, ... gpdam) composites from Day –6 to Day 2 of JJA hot extremes. Stars (hatching) denote statistically significant values of v' (Z') at α=0.10. d) Same as c) but for DJF cold extremes. 47

4.3 a) Hovmöller composites of 850 hPa T' (color shading) and 300 hPa v' (blue/magenta contours indicate negative/positive anomalies at ±3, ±5, ±7, ... m/s) during DJF persistent (left) and short-term (right) cold extremes. Stars (hatching) denote statistically significant values of T' (v') at α=0.10. b) Same as a) but for hot extremes. c), d) Same for MAM. e), f) Same for JJA. g), h) Same for SON. 48

4.4 a) Left: Hovmöller composites of 850 hPa T' (color shading) and 300 hPa v' forecasts (blue/magenta contours indicate negative/positive anomalies at ±3, ±5, ±7, ... m/s), issued 3 days prior to JJA persistent hot extremes. Stars (hatching) denote statistically significant values of T' (v') at α=0.10. Right: Deviation of the forecasted 850 hPa T' (color shading) and 300 hPa v' (solid/dashed contours indicate positive/negative anomalies at ±2, ±3, ±4, ... m/s) from the respective reanalysis fields (Fig. 3f left). Statistically significant deviations are assumed where both the forecast and reanalysis fields are significant at α=0.10. b) Same as a) but for DJF persistent cold extremes. c),d) Same as a),b) but for forecasts issued 5 days prior to the extremes. 50

5.1 Illustration of the c_p and c_{gx} diagnosis in the barotropic model simulation. (a)–(c) v at three consecutive 6-hourly time steps (color shading) and isoline of $E_0 = 3ms^{-1}$ (yellow contour). (d) v_ℓ evolution at 40°N . (e) Φ_{v_ℓ} evolution at 40°N . (f) c_p at 40°N . (g) Map of c_p at t_0. (h)–(j) E at three consecutive 6-hourly time steps. (k) E_ℓ (solid lines) and E'_ℓ (dotted lines) evolution at 40°N . (l) $\Phi_{E'_\ell}$ evolution at 40°N . (f) c_{gx} at 40°N . (g) Map of c_{gx} at t_0. Orange, green and blue colors in (d)–(f) and (k)–(m) correspond to the $t_0 - 6hr$, t_0 and $t_0 + 6hr$ time steps respectively (as indicated in the legends). Gray shading in (f) and (m) indicates longitudes where c_p and c_{gx} are not defined. 61

5.2 Illustration of the c_{gy} diagnosis in the barotropic model simulation. (a) E_n (solid lines) and E'_n (dotted lines) at 80°E for the three consecutive 6-hourly time steps. (b) $\Phi_{E'_n}$ evolution at 80°E . (c) c_{gy} at 80°E . (d) Map of c_{gy} at t_0. Orange, green and blue colors in (a)–(c) correspond to the $t_0 - 6hr$, t_0 and $t_0 + 6hr$ time steps respectively (as indicated in the legends). Gray shading in (c) indicates longitudes where c_{gy} is not defined. 62

5.3 Illustration of the c_p and $\boldsymbol{c_g}$ diagnosis at t_0: 23 August 2016 - 1200 UTC. (a)–(c) v at three consecutive 6-hourly time steps (color shading) and isoline of $E_0 = 15ms^{-1}$ (yellow contour). (d) Map of c_p at t_0. (e)–(g) E at three consecutive 6-hourly time steps. (h) c_{gx} (color shading) in [deg/6hr] and arrows of $\boldsymbol{c_g}$ in [m/s] (scale is at the lower right) at t_0. . 63

5.4 Northern Hemisphere climatology of RWP properties. Seasonal median of: (a)–(d) E, (e)–(h) c_p, (i)–(l) c_{gx} and (m)–(p) c_{gy} at 300 hPa in the 1979–2018 period. Each column of panels corresponds to the season indicated at the yellow label atop. 68

5.5 Same as Fig. 5.4, but for the Southern Hemisphere. 69

5.6 Areas used in averaging E and c_p at 300 hPa (blue rectangle) and T' at 850 hPa (red rectangle). The blue rectangle spans the area: 38°N –62°N , 2°W –22°E and the red rectangle spans the area: 46°N –54°N , 6°E –14°E . 70

5.7 (a) Histogram (left axis) and the corresponding KDE (right axis) of the normalized (area-averaged) daily mean c_p at 300 hPa during hot extreme days over Central Europe. Red (orange) colors correspond to persistent (short-lived) hot extremes. Each bin accounts for 0.2 σ. (b) Same as (a) but for persistent (blue) and short-lived (purple) cold extremes. Shown in the legend is the mean ($\bar{c_p}$) and standard deviation (s) of c_p for each type of extreme. The KDE bandwidth parameter for persistent (short-lived) hot extremes is 0.27 (0.28) and for persistent (short-lived) cold extremes it is 0.36 (0.39). 71

5.8 Two-dimensional KDE of the normalized (area-averaged) daily mean E against c_p at 300 hPa. Black contours correspond to the climatology (1979–2018), while the color shading depicts the anomaly during persistent (a) and short-lived (b) hot extremes, and persistent (c) and short-lived (d) cold extremes over Central Europe. The KDE bandwidth parameter for climatology is 0.19, for persistent (short-lived) hot extremes it is 0.34 (0.33) and for persistent (short-lived) cold extremes it is 0.39 (0.38). 73

5.9 Inter-quartile mean of daily mean c_p (color shading), E (black contours at $18, 20, 22, 24\ ms^{-1}$) and Z' at 500 hPa (magenta contours at $\pm 4, \pm 8, \pm 12, \pm 16\ gpdam$) during temperature extreme days over Central Europe. The panels correspond to: (a) JJA persistent hot, (b) JJA short-lived hot, (c) DJF persistent cold, and (d) DJF short-lived cold extreme days. For Z', solid (dashed) contours correspond to positive (negative) anomalies. 74

5.10 Local phase diagnosis in the case of two RWPs with equal amplitude and length. Panel (a) depicts the original function ($v(x)$, blue solid line), the imaginary part of its analytic signal ($Im[A_v]$, blue dotted line), the envelope (E, gray line), the envelope deviation from the mean (E', red solid line) and the imaginary part of its analytic signal ($Im[A_{E'}]$, red dotted line). Panel (b) shows the local phase of v (Φ_v, thick blue dotted line) and E' ($\Phi_{E'}$, thick red dotted line). 78

5.11 Same as Fig. 5.10, but for the case of two RWPs with equal length but unequal amplitude. 78

5.12 Object-based envelope phase diagnosis in the case of the two RWPs in Fig. 5.11. Panel (a) depicts the original envelope (E, gray line), the envelope deviation from the object zonal mean (E', thick red dotted line) and the imaginary part of the analytic signal of the two RWPs ($Im[A_{E'}]$, red dotted line). Panel (b) shows the local phase of E' ($\Phi_{E'}$, thick red dotted line). 79

5.13 Illustration of the c_{gy} diagnosis as in Fig. 5.2 of the paper, but without the equal-length requirement. (a) E_n (solid lines) and E'_n (dotted lines) at 80°E for the three consecutive 6-hourly time steps. (b) $\Phi_{E'_n}$ evolution at 80°E . (c) c_{gy} at 80°E . (d) Map of c_{gy} at t_0. Orange, green and blue colors in (a)–(c) correspond to the $t_0 - 6hr$, t_0 and $t_0 + 6hr$ time steps respectively (as indicated in the legends). Gray shading in (c) indicates longitudes where c_{gy} is not defined. 81

5.14 Wavelet analysis on meridional wind along a latitude circle at 21/8/2016 - 1200 UTC (Fig. 5.3 in the paper). (a) Meridional wind anomaly, v'_ℓ, and its envelope, E_ℓ, at 60°N . (b) Wavelet power spectrum (color shading) and its maximum at every longitude (black dashed line) which corresponds to the dominant wavenumber. The black line corresponds to the local wavenumber as computed by the Hilbert transform method (eq. 5.10 in the paper). 82

5.15 RWP frequency (%) at 300hPa in the Northern (a)–(d) and Southern (e)–(h) Hemispheres. Each column of panels corresponds to the season indicated at the yellow label atop. 83

5.16 Median zonal wind speed at 300hPa in the Northern (a)–(d) and Southern (e)–(h) Hemispheres. Each column of panels corresponds to the season indicated at the yellow label atop. 84

5.17 Median meridional wind speed at 300hPa in the Northern (a)–(d) and Southern (e)–(h) Hemispheres. Each column of panels corresponds to the season indicated at the yellow label atop. 84

5.18 Two-dimensional kernel density estimation of the normalized (area-averaged) daily mean E against c_p at 300hPa. Black contours correspond to the climatology (1979–2018). The 3 rectangles indicate the regimes at the 3 vertices of the distribution. Their specific range in percentiles of E and c_p is: a) $E \in (85^{th}, 98^{th})$ and $c_p \in (30^{th}, 70^{th})$, b) $E \in (5^{th}, 50^{th})$ and $c_p \in (2^{th}, 15^{th})$, c) $E \in (5^{th}, 50^{th})$ and $c_p \in (85^{th}, 98^{th})$. 85

5.19 (a) Composites of c_p (color shading) and E (black contours) over the (a) 727 days that occupy the regime of high E values (orange rectangle in Fig. 5.16), (b) 719 days that occupy the regime of low E and low c_p values (red rectangle in Fig. 5.16) and (c) 837 days that occupy the regime of low E and high c_p values (blue rectangle in Fig. 5.16). . . . 86

6.1 Medium-range forecast biases in Northern Hemisphere RWP properties. The first column of panels shows the inter-quartile mean of E (a) and c_p (e) in the 2013–2018 period based on the ERA5 reanalysis. The second column of panels (b,f) shows the deviation of the deterministic 3-day forecast inter-quartile mean from the reanalysis of the respective field. The third (c,g) and fourth columns (d,h) correspond to the 5-day and 7-day forecast inter-quartile means respectively. 90

6.2 Medium-range forecast biases in Northern Hemisphere RWP properties and the jet stream. The first column of panels shows the inter-quartile mean of ω (a), k (e), and u (i) in the 2013–2018 period based on the ERA5 reanalysis. The second column of panels (b,f,j) shows the deviation of the deterministic 3-day forecast inter-quartile mean from the reanalysis of the respective field. The third (c,g,k) and fourth columns (d,h,l) correspond to the 5-day and 7-day forecast inter-quartile means respectively. 91
6.3 Same as Fig. 6.1 but for medium-range forecasts in DJF only. 92
6.4 Same as Fig. 6.1 but for medium-range forecasts in JJA only. 93

A.1 Initial state of the barotropic model simulation: (a) meridional wind v (color shading, in $\mathrm{m\,s^{-1}}$) and (b) local dominant wavenumber (color shading, dimensionless) from wavelet analysis. 100
A.2 Same analysis as in Fig. A.1, but here for the flow on the 320 K isentrope on 0000 UTC 11 April 2011. 101

List of Tables

4.1 Number and mean duration (in days) of hot and cold extremes. Values in the parenthesis correspond to persistent temperature extremes. . . . 46

5.1 Number of Central European temperature extremes for each type and season. The values correspond to the number of extreme events and the parentheses show the total number of extreme days. 86
5.2 List of Python modules used in this study. In the Notes column we indicate their specific application. 87

Bibliography

Ahmadi-Givi F, Nasr-Esfahany M, Mohebalhojeh AR. 2014. Interaction of North Atlantic baroclinic wave packets and the Mediterranean storm track. *Quarterly Journal of the Royal Meteorological Society* **140**(680): 754–765, doi:10.1002/qj.2171.

Anthes RA, Kuo YH, Baumhefner DP, Errico RM, Bettge TW. 1985. Predictability of mesoscale atmospheric motions. *Advances in Geophysics* **28**: 159–202, doi:10.1016/S0065-2687(08)60188-0.

Barnes EA, Screen JA. 2015. The impact of Arctic warming on the midlatitude jetstream: Can it? Has it? Will it? *Wiley Interdisciplinary Reviews: Climate Change* **6**(3): 277–286, doi:10.1002/wcc.337.

Baumgart M, Ghinassi P, Wirth V, Selz T, Craig GC, Riemer M. 2019. Quantitative View on the Processes Governing the Upscale Error Growth up to the Planetary Scale Using a Stochastic Convection Scheme. *Monthly Weather Review* **147**(5): 1713–1731, doi:10.1175/MWR-D-18-0292.1.

Berbery EH, Vera CS, Berbery EH, Vera CS. 1996. Characteristics of the Southern Hemisphere Winter Storm Track with Filtered and Unfiltered Data. *Journal of the Atmospheric Sciences* **53**(3): 468–481, doi:10.1175/1520-0469(1996)053⟨0468:COTSHW⟩2.0.CO;2.

Berrisford P, Dee D, Fielding K, Fuentes M, Kallberg P, Kobayashi S, Uppala S. 2009. The ERA-Interim Archive. *ERA report series* **1**(1): 1–16.

Bieli M, Pfahl S, Wernli H. 2015a. A lagrangian investigation of hot and cold temperature extremes in europe. *Quarterly Journal of the Royal Meteorological Society* **141**(686): 98–108, doi:10.1002/qj.2339.

Bieli M, Pfahl S, Wernli H. 2015b. A Lagrangian investigation of hot and cold temperature extremes in Europe. *Quarterly Journal of the Royal Meteorological Society* **141**(686): 98–108, doi:10.1002/qj.2339.

Black E, Blackburn M, Harrison G, Hoskins B, Methven J. 2004. Factors contributing to the summer 2003 European heatwave. *Weather* **59**(8): 217–223, doi:10.1256/wea.74.04.

Blackmon ML, Lee YH, Wallace JM, Hsu HH. 1984. Time Variation of 500 mb Height Fluctuations with Long, Intermediate and Short Time Scales as Deduced from Lag-Correlation Statistics. *Journal of the Atmospheric Sciences* **41**(6): 981–991, doi:10.1175/1520-0469(1984)041⟨0981:TVOMHF⟩2.0.CO;2.

Bougeault P, Toth Z, Bishop C, Brown B, Burridge D, Chen DH, Ebert B, Fuentes M, Hamill TM, Mylne K, Nicolau J, Paccagnella T, Park YY, Parsons D, Raoult

B, Schuster D, Dias PS, Swinbank R, Takeuchi Y, Tennant W, Wilson L, Worley S. 2010. The THORPEX Interactive Grand Global Ensemble. *Bulletin of the American Meteorological Society* **91**(8): 1059–1072, doi:10.1175/2010BAMS2853.1.

Branstator G. 2002. Circumglobal teleconnections, the jet stream waveguide, and the North Atlantic Oscillation. *Journal of Climate* **15**(14): 1893–1910, doi:10.1175/1520-0442(2002)015⟨1893:CTTJSW⟩2.0.CO;2.

Butler AH, Thompson DW, Heikes R. 2010. The steady-state atmospheric circulation response to climate change–like thermal forcings in a simple general circulation model. *Journal of Climate* **23**(13): 3474–3496, doi:10.1175/2010JCLI3228.1.

Cai M, Huang B. 2013. A Dissection of Energetics of the Geostrophic Flow: Reconciliation of Rossby Wave Energy Flux and Group Velocity. *Journal of the Atmospheric Sciences* **70**(7): 2179–2196, doi:10.1175/JAS-D-12-0249.1.

Chang E. 2001a. GCM and Observational Diagnoses of the Seasonal and Interannual Variations of the Pacific Storm Track during the Cool Season. *Journal of the Atmospheric Sciences* **58**(1992): 1784–1800, doi:10.1175/1520-0469(2001)058⟨1784:GAODOT⟩2.0.CO;2.

Chang EK. 2001b. The structure of baroclinic wave packets. *Journal of the Atmospheric Sciences* **58**(13): 1694–1713, doi:10.1175/1520-0469(2001)058⟨1694:TSOBWP⟩2.0.CO;2.

Chang EK, Ma CG, Zheng C, Yau AM. 2016. Observed and projected decrease in Northern Hemisphere extratropical cyclone activity in summer and its impacts on maximum temperature. *Geophysical Research Letters* **43**(5): 2200–2208, doi:10.1002/2016GL068172.

Chang EKM. 1993. Downstream Development of Baroclinic Waves As Inferred from Regression Analysis. doi:10.1175/1520-0469(1993)050⟨2038:DDOBWA⟩2.0.CO;2.

Chang EKM. 1999. Characteristics of Wave Packets in the Upper Troposphere. Part II: Seasonal and Hemispheric Variations. *Journal of the Atmospheric Sciences* **56**(11): 1729–1747, doi:10.1175/1520-0469(1999)056⟨1729:COWPIT⟩2.0.CO;2.

Chang EKM. 2005. The Impact of Wave Packets Propagating across Asia on Pacific Cyclone Development. *Monthly Weather Review* **133**(7): 1998–2015, doi:10.1175/MWR2953.1.

Chang EKM, Lee S, Swanson KL. 2002. Storm Track Dynamics. *Journal of Climate* **15**(16): 2163–2183, doi:10.1175/1520-0442(2002)015⟨02163:STD⟩2.0.CO;2.

Chang EKM, Orlanski I. 1994. On Energy Flux and Group Velocity of Waves in Baroclinic Flows. *Journal of the Atmospheric Sciences* **51**(24): 3823–3828, doi:10.1175/1520-0469(1994)051⟨3823:OEFAGV⟩2.0.CO;2.

Chang EKM, Yu DB. 1999. Characteristics of Wave Packets in the Upper Troposphere. Part I: Northern Hemisphere Winter. *Journal of the Atmospheric Sciences* **56**(11): 1708–1728, doi:10.1175/1520-0469(1999)056⟨1708:COWPIT⟩2.0.CO;2.

Chaudhury KN, Unser M. 2009. Construction of Hilbert transform pairs of wavelet bases and gabor-like transforms. *IEEE Transactions on Signal Processing* **57**(9): 3411–3425, doi:10.1109/TSP.2009.2020767.

Cohen L. 1995. *Time-frequency analysis*. Prentice Hall PTR, ISBN 0-13-594532-1.

Copernicus Climate Change Service (C3S). 2017. ERA5: Fifth generation of ECMWF atmospheric reanalyses of the global climate. *Copernicus Climate Change Service Climate Data Store (CDS). Date of access: February 2019.* URL `https://cds.climate.copernicus.eu/cdsapp#!/home`.

Coumou D, Petoukhov V, Rahmstorf S, Petri S, Schellnhuber HJ. 2014. Quasi-resonant circulation regimes and hemispheric synchronization of extreme weather in boreal summer. *Proceedings of the National Academy of Sciences* **111**(34): 12 331–12 336, doi:10.1073/pnas.1412797111.

Davies HC. 2015a. The Quasigeostrophic Omega Equation: Reappraisal, Refinements, and Relevance. *Monthly Weather Review* **143**(1): 3–25, doi:10.1175/MWR-D-14-00098.1.

Davies HC. 2015b. Weather chains during the 2013/2014 winter and their significance for seasonal prediction. *Nature Geoscience* **8**(11): 833–837, doi:10.1038/ngeo2561.

Dee DP, Uppala SM, Simmons AJ, Berrisford P, Poli P, Kobayashi S, Andrae U, Balmaseda MA, Balsamo G, Bauer P, Bechtold P, Beljaars AC, van de Berg L, Bidlot J, Bormann N, Delsol C, Dragani R, Fuentes M, Geer AJ, Haimberger L, Healy SB, Hersbach H, Hólm EV, Isaksen L, Kållberg P, Köhler M, Matricardi M, Mcnally AP, Monge-Sanz BM, Morcrette JJ, Park BK, Peubey C, de Rosnay P, Tavolato C, Thépaut JN, Vitart F. 2011. The ERA-Interim reanalysis: Configuration and performance of the data assimilation system. *Quarterly Journal of the Royal Meteorological Society* **137**(656): 553–597, doi:10.1002/qj.828.

Dickinson RE. 1978. Rossby Waves–Long-Period Oscillations of Oceans and Atmospheres. *Annual Review of Fluid Mechanics* **10**(1): 159–195, doi:10.1146/annurev.fl.10.010178.001111.

Domeisen DIV, Martius O, Jiménez-Esteve B. 2018. Rossby Wave Propagation into the Northern Hemisphere Stratosphere: The Role of Zonal Phase Speed. *Geophysical Research Letters* **45**(4): 2064–2071, doi:10.1002/2017GL076886.

Esler J, Haynes P. 1999a. Mechanisms for wave packet formation and maintenance in a quasigeostrophic two-layer model. *Journal of the Atmospheric Sciences* **56**(15): 2457–2490, doi:10.1175/1520-0469(0)056⟨2457:MFWPFA⟩2.0.CO;2.

Esler JG. 2004. Benjamin–Feir instability of Rossby waves on a jet. *Quarterly Journal of the Royal Meteorological Society* **130**(600): 1611–1630, doi:10.1256/qj.03.74.

Esler JG, Haynes PH. 1999b. Baroclinic Wave Breaking and the Internal Variability of the Tropospheric Circulation. *Journal of the Atmospheric Sciences* **56**(23): 4014–4031, doi:10.1175/1520-0469(1999)056⟨4014:BWBATI⟩2.0.CO;2.

Farge M. 1992. Wavelet transforms and their applications to turbulence. *Annual review of fluid mechanics* **24**(1): 395–458, doi:10.1146/annurev.fl.24.010192.002143.

Feldstein SB, Dayan U. 2008. Circumglobal teleconnections and wave packets associated with Israeli winter precipitation. *Quarterly Journal of the Royal Meteorological Society* **134**(631): 455–467, doi:10.1002/qj.225.

Feudale L, Shukla J. 2011. Influence of sea surface temperature on the European heat

wave of 2003 summer. Part I: an observational study. *Climate dynamics* **36**(9-10): 1691–1703, doi:10.1007/s00382-010-0788-0.

Fink AH, Brücher T, Krüger A, Leckebusch GC, Pinto JG, Ulbrich U. 2004. The 2003 European summer heatwaves and drought–synoptic diagnosis and impacts. *Weather* **59**(8): 209–216, doi:10.1256/wea.73.04.

Fischer EM, Seneviratne S, Vidale P, Lüthi D, Schär C. 2007a. Soil moisture-atmosphere interactions during the 2003 European summer heat wave. *Journal of Climate* **20**(20): 5081–5099, doi:10.1175/JCLI4288.1.

Fischer EM, Seneviratne SI, Lüthi D, Schär C. 2007b. Contribution of land-atmosphere coupling to recent European summer heat waves. *Geophysical Research Letters* **34**(6), doi:10.1029/2006GL029068.

Founda D, Giannakopoulos C. 2009. The exceptionally hot summer of 2007 in Athens, Greece - A typical summer in the future climate? *Global and Planetary Change* **67**(3-4): 227–236, doi:10.1016/j.gloplacha.2009.03.013.

Fragkoulidis G, Wirth V. 2018. Synoptic circulation patterns during temperature extremes in southeastern Europe. In: *Proceedings of the 14th International Conference on Meteorology, Climatology and Atmospheric Physics, Alexandroupoli, Greece*, ISBN 978-960-98220-4-6.

Fragkoulidis G, Wirth V, Bossmann P, Fink AH. 2018. Linking Northern Hemisphere temperature extremes to Rossby wave packets. *Quarterly Journal of the Royal Meteorological Society* **144**(711): 553–566, doi:10.1002/qj.3228.

Gabor D. 1946. Theory of communication. Part 1: The analysis of information. *Journal of the Institution of Electrical Engineers - Part III: Radio and Communication Engineering* **93**(26): 429–441, doi:10.1049/ji-3-2.1946.0074.

Gabriel A, Peters D. 2008. A Diagnostic Study of Different Types of Rossby Wave Breaking Events in the Northern Extratropics. *Journal of the Meteorological Society of Japan* **86**(5): 613–631, doi:10.2151/jmsj.86.613.

García-Herrera R, Díaz J, Trigo R, Luterbacher J, Fischer E. 2010. A review of the European summer heat wave of 2003. *Critical Reviews in Environmental Science and Technology* **40**(4): 267–306, doi:10.1080/10643380802238137.

Garfinkel CI, Harnik N. 2017. The non-Gaussianity and spatial asymmetry of temperature extremes relative to the storm track: The role of horizontal advection. *Journal of Climate* **30**(2): 445–464, doi:10.1175/JCLI-D-15-0806.1.

Ghinassi P, Fragkoulidis G, Wirth V, Ghinassi P, Fragkoulidis G, Wirth V. 2018. Local Finite-Amplitude Wave Activity as a Diagnostic for Rossby Wave Packets. *Monthly Weather Review* **146**(12): 4099–4114, doi:10.1175/MWR-D-18-0068.1.

Glatt I, Dörnbrack A, Jones S, Keller J, Martius O, Müller A, Peters DH, Wirth V. 2011. Utility of Hovmöller diagrams to diagnose Rossby wave trains. *Tellus, Series A: Dynamic Meteorology and Oceanography* **63**(5): 991–1006, doi:10.1111/j.1600-0870.2011.00541.x.

Glatt I, Wirth V. 2014. Identifying Rossby wave trains and quantifying their properties. *Quarterly Journal of the Royal Meteorological Society* **140**(679): 384–396, doi:10.

1002/qj.2139.

Gray SL, Dunning CM, Methven J, Masato G, Chagnon JM. 2014. Systematic model forecast error in Rossby wave structure. *Geophysical Research Letters* **41**(8): 2979–2987, doi:10.1002/2014GL059282.

Grazzini F, Fragkoulidis G, Wirth V, Craig GC. 2019. Extreme precipitation events over Northern Italy. Part (II): the role of Rossby wave packets as dynamical precursor. *Quarterly Journal of the Royal Meteorological Society, in preparation* .

Grazzini F, Vitart F. 2015. Atmospheric predictability and Rossby wave packets. *Quarterly Journal of the Royal Meteorological Society* **141**(692): 2793–2802, doi:10.1002/qj.2564.

Hakim GJ. 2003. Developing Wave Packets in the North Pacific Storm Track. *Monthly Weather Review* **131**(11): 2824–2837, doi:10.1175/1520-0493(2003)131⟨2824:DWPITN⟩2.0.CO;2.

Harris FJ. 1978. On the use of windows for harmonic analysis with the discrete Fourier transform. *Proceedings of the Institute of Electrical and Electronic Engineers* **66**(1): 51–83.

Hartmann DL. 2015. *Global physical climatology*, vol. 103. Newnes.

Harvey B, Methven J, Ambaum MHP. 2018. An Adiabatic Mechanism for the Reduction of Jet Meander Amplitude by Potential Vorticity Filamentation. *Journal of the Atmospheric Sciences* **75**(12): 4091–4106, doi:10.1175/JAS-D-18-0136.1.

Harvey B, Shaffrey L, Woollings T. 2014. Equator-to-pole temperature differences and the extra-tropical storm track responses of the CMIP5 climate models. *Climate Dynamics* **43**(5-6): 1171–1182, doi:10.1007/s00382-013-1883-9.

Harvey BJ, Methven J, Ambaum MHP. 2016. Rossby wave propagation on potential vorticity fronts with finite width. *Journal of Fluid Mechanics* **794**: 775–797, doi:10.1017/jfm.2016.180.

Haurwitz B. 1940. The motion of atmospheric disturbances on the spherical earth. *J. Mar. Res.* **3**: 254–267.

Hauser M, Orth R, Seneviratne SI. 2016. Role of soil moisture versus recent climate change for the 2010 heat wave in western Russia. *Geophysical Research Letters* **43**(6): 2819–2826, doi:10.1002/2016GL068036.

Hayashi Y. 1982. Space-Time Spectral Analysis and its Applications to Atmospheric Waves. *Journal of the Meteorological Society of Japan. Ser. II* **60**(1): 156–171, doi:10.2151/jmsj1965.60.1_156.

Held IM. 1983. Stationary and quasi-stationary eddies in the extratropical troposphere: Theory. doi:10.1175/1520-0469(1993)050⟨0212:AGFIDA⟩2.0.CO;2.

Held IM, Hoskins BJ. 1985. Large-Scale Eddies and the General Circulation of the Troposphere. *Advances in Geophysics* **28**(PA): 3–31, doi:10.1016/S0065-2687(08)60218-6.

Hirschi M, Seneviratne SI, Alexandrov V, Boberg F, Boroneant C, Christensen OB, Formayer H, Orlowsky B, Stepanek P. 2011. Observational evidence for soil-moisture impact on hot extremes in southeastern Europe. *Nature Geoscience* **4**(1): 17–21, doi:

10.1038/ngeo1032.

Holton J, Hakim G. 2013. *An Introduction to Dynamic Meteorology, 5th Edition*. Academic Press, ISBN 9780123848673, doi:10.1016/C2009-0-63394-8.

Horton RM, Mankin JS, Lesk C, Coffel E, Raymond C. 2016. A review of recent advances in research on extreme heat events. *Current Climate Change Reports* **2**(4): 242–259, doi:10.1007/s40641-016-0042-x.

Hoskins B, Woollings T. 2015. Persistent extratropical regimes and climate extremes. *Current Climate Change Reports* **1**(3): 115–124, doi:10.1007/s40641-015-0020-8.

Hoskins BJ, Ambrizzi T. 1993. Rossby wave propagation on a realistic longitudinally varying flow. *Journal of the Atmospheric Sciences* **50**(12): 1661–1671, doi:10.1175/1520-0469(1993)050⟨1661:RWPOAR⟩2.0.CO;2.

Hoskins BJ, Karoly DJ. 1981. The Steady Linear Response of a Spherical Atmosphere to Thermal and Orographic Forcing. *Journal of the Atmospheric Sciences* **38**(6): 1179–1196, doi:10.1175/1520-0469(1981)038⟨1179:TSLROA⟩2.0.CO;2.

Hovmöller E. 1949. The trough-and-ridge diagram. *Tellus* **1**(2): 62–66, doi:10.1111/j.2153-3490.1949.tb01260.x.

Hsu HH. 1987. Propagation of Low-Level Circulation Features in the Vicinity of Mountain Ranges. *Monthly Weather Review* **115**(9): 1864–1893, doi:10.1175/1520-0493(1987)115⟨1864:POLLCF⟩2.0.CO;2.

Huang NE, Shen Z, Long SR, Wu MC, Shih HH, Zheng Q, Yen NC, Tung CC, Liu HH. 1998. The empirical mode decomposition and the Hilbert spectrum for nonlinear and non-stationary time series analysis. *Proceedings of the Royal Society of London. Series A: Mathematical, Physical and Engineering Sciences* **454**(1971): 903–995, doi:10.1098/rspa.1998.0193.

Huang NE, Wu Z, Long SR, Arnold KC, Chen X, Blank K. 2009. On instantaneous frequency. *Advances in Adaptive Data Analysis* **1**(2): 177–229, doi:10.1142/S1793536909000096.

Hunter JD. 2007. Matplotlib: A 2D Graphics Environment. *Computing in Science & Engineering* **9**(3): 90–95, doi:10.1109/MCSE.2007.55.

Joung CH, Hitchman MH. 1982. On the Role of Successive Downstream Development in East Asian Polar Air Outbreaks. *Monthly Weather Review* **110**(9): 1224–1237, doi:10.1175/1520-0493(1982)110⟨1224:OTROSD⟩2.0.CO;2.

Kohavi R. 1995. A study of cross-validation and bootstrap for accuracy estimation and model selection. *Proceedings of the 14th international joint conference on Artificial intelligence* **2**: 1137–1143.

Kornhuber K, Petoukhov V, Karoly D, Petri S, Rahmstorf S, Coumou D. 2017a. Summertime Planetary Wave Resonance in the Northern and Southern Hemispheres. *Journal of Climate* **30**(16): 6133–6150, doi:10.1175/JCLI-D-16-0703.1.

Kornhuber K, Petoukhov V, Petri S, Rahmstorf S, Coumou D. 2017b. Evidence for wave resonance as a key mechanism for generating high-amplitude quasi-stationary waves in boreal summer. *Climate Dynamics* **49**(5-6): 1961–1979, doi:10.1007/s00382-016-3399-6.

Kornhuber K, Petoukhov V, Petri S, Rahmstorf S, Coumou D. 2017c. Evidence for wave resonance as a key mechanism for generating high-amplitude quasi-stationary waves in boreal summer. *Climate Dynamics* **49**(5-6): 1961–1979, doi:10.1007/s00382-016-3399-6.

Kyselý J. 2008. Influence of the persistence of circulation patterns on warm and cold temperature anomalies in Europe: Analysis over the 20th century. *Global and Planetary Change* **62**(1-2): 147–163, doi:10.1016/j.gloplacha.2008.01.003.

Lackmann G. 2011. *Midlatitude synoptic meteorology*. American Meteorological Society.

Lau NC, Nath MJ. 2014. Model simulation and projection of European heat waves in present-day and future climates. *Journal of Climate* **27**(10): 3713–3730, doi:10.1175/JCLI-D-13-00284.1.

Lau WK, Kim KM. 2012. The 2010 Pakistan flood and Russian heat wave: Teleconnection of hydrometeorological extremes. *Journal of Hydrometeorology* **13**(1): 392–403, doi:10.1175/JHM-D-11-016.1.

Lee S, Held IM. 1993. Baroclinic Wave Packets in Models and Observations. *Journal of the Atmospheric Sciences* **50**(10): 1413–1428, doi:10.1175/1520-0469(1993)050⟨1413:BWPIMA⟩2.0.CO;2.

Liu Y, San Liang X, Weisberg RH. 2007. Rectification of the bias in the wavelet power spectrum. *Journal of Atmospheric and Oceanic Technology* **24**(12): 2093–2102, doi:10.1175/2007JTECHO511.1.

Lyon B, Dole RM. 1995. A diagnostic comparison of the 1980 and 1988 US summer heat wave-droughts. *Journal of Climate* **8**(6): 1658–1675, doi:10.1175/1520-0442(1995)008⟨1658:ADCOTA⟩2.0.CO;2.

Marple LS. 1999. Computing the discrete-time "analytic" signal via FFT. *IEEE Transactions on Signal Processing* **47**(9): 2600–2603, doi:10.1109/78.782222.

Martínez-Alvarado O, Madonna E, Gray SL, Joos H. 2016. A route to systematic error in forecasts of Rossby waves. *Quarterly Journal of the Royal Meteorological Society* **142**(694): 196–210, doi:10.1002/qj.2645, URL `http://doi.wiley.com/10.1002/qj.2645`.

Martius O, Schwierz C, Davies HC. 2008. Far-upstream precursors of heavy precipitation events on the Alpine south-side. *Quarterly Journal of the Royal Meteorological Society* **134**(631 PART B): 417–428, doi:10.1002/qj.229.

Matsueda M. 2011. Predictability of Euro-Russian blocking in summer of 2010. *Geophysical Research Letters* **38**(6), doi:10.1029/2010GL046557.

Meehl GA, Tebaldi C. 2004. More intense, more frequent, and longer lasting heat waves in the 21st century. *Science* **305**(5686): 994–997, doi:10.1126/science.1098704.

Miralles DG, Teuling AJ, Van Heerwaarden CC, de Arellano JVG. 2014. Mega-heatwave temperatures due to combined soil desiccation and atmospheric heat accumulation. *Nature Geoscience* **7**(5): 345–349, doi:10.1038/ngeo2141.

Nakamura H. 1992. Midwinter Suppression of Baroclinic Wave Activity in the Pacific. *Journal of the Atmospheric Sciences* **49**(17): 1629–1642, doi:10.1175/1520-0469(1992)049⟨1629:MSOBWA⟩2.0.CO;2.

Nakamura H, Shimpo A. 2004. Seasonal variations in the Southern Hemisphere storm tracks and jet streams as revealed in a reanalysis dataset. *Journal of Climate* **17**(9): 1828–1844, doi:10.1175/1520-0442(2004)017⟨1828:SVITSH⟩2.0.CO;2.

O'Brien L, Reeder MJ. 2017. Southern Hemisphere summertime Rossby waves and weather in the Australian region. *Quarterly Journal of the Royal Meteorological Society* **143**(707): 2374–2388, doi:10.1002/qj.3090.

Orlanski I, Chang EKM. 1993. Ageostrophic Geopotential Fluxes in Downstream and Upstream Development of Baroclinic Waves. *Journal of the Atmospheric Sciences* **50**(2): 212–225, doi:10.1175/1520-0469(1993)050⟨0212:AGFIDA⟩2.0.CO;2.

Otto FE, Massey N, Oldenborgh G, Jones R, Allen M. 2012. Reconciling two approaches to attribution of the 2010 Russian heat wave. *Geophysical Research Letters* **39**(4), doi:10.1029/2011GL050422.

Papritz L, Pfahl S, Sodemann H, Wernli H. 2015. A climatology of cold air outbreaks and their impact on air-sea heat fluxes in the high-latitude South Pacific. *Journal of Climate* **28**(1): 342–364, doi:10.1175/JCLI-D-14-00482.1.

Pedlosky J. 2003. *Waves in the Ocean and Atmosphere: Introduction to Wave Dynamics*. Springer Berlin Heidelberg: Berlin, Heidelberg, ISBN 978-3-642-05564-5, doi:10.1007/978-3-662-05131-3.

Pedregosa F, Weiss R, Brucher M. 2011. Scikitlearn: Machine Learning in Python. *Journal of Machine Learning Research* **12**(Oct): 2825–2830, doi:10.1007/s13398-014-0173-7.2.

Petoukhov V, Rahmstorf S, Petri S, Schellnhuber HJ. 2013a. Quasiresonant amplification of planetary waves and recent Northern Hemisphere weather extremes. *Proceedings of the National Academy of Sciences* **110**(14): 5336–5341, doi:10.1073/pnas.1222000110.

Petoukhov V, Rahmstorf S, Petri S, Schellnhuber HJ. 2013b. Quasiresonant amplification of planetary waves and recent Northern Hemisphere weather extremes. *Proceedings of the National Academy of Sciences* **110**(14): 5336–5341, doi:10.1073/pnas.1222000110.

Pfahl S. 2014. Characterising the relationship between weather extremes in Europe and synoptic circulation features. *Natural Hazards and Earth System Sciences* **14**(6): 1461–1475, doi:10.5194/nhess-14-1461-2014.

Pfahl S, Wernli H. 2012. Quantifying the relevance of atmospheric blocking for co-located temperature extremes in the Northern Hemisphere on (sub-)daily time scales. *Geophysical Research Letters* **39**(12), doi:10.1029/2012GL052261.

Pierrehumbert RT, Swanson KL. 1995. Baroclinic Instability. *Annual Review of Fluid Mechanics* **27**(1): 419–467, doi:10.1146/annurev.fl.27.010195.002223.

Plumb RA. 1985. On the Three-Dimensional Propagation of Stationary Waves. *Journal of the Atmospheric Sciences* **42**(3): 217–229, doi:10.1175/1520-0469(1985)042⟨0217:OTTDPO⟩2.0.CO;2.

Quandt LA, Keller JH, Martius O, Jones SC. 2017. Forecast variability of the blocking system over Russia in summer 2010 and its impact on surface conditions. *Weather*

and Forecasting **32**(1): 61–82, doi:10.1175/WAF-D-16-0065.1.

Quinting JF, Jones SC. 2016. On the Impact of Tropical Cyclones on Rossby Wave Packets: A Climatological Perspective. *Monthly Weather Review* **144**(5): 2021–2048, doi:10.1175/MWR-D-14-00298.1.

Quinting JF, Reeder MJ. 2017. Southeastern Australian heat waves from a trajectory viewpoint. *Monthly Weather Review* (2017).

Quinting JF, Vitart F. 2019. Representation of Synoptic-Scale Rossby Wave Packets and Blocking in the S2S Prediction Project Database. *Geophysical Research Letters* **46**(2): 1070–1078, doi:10.1029/2018GL081381.

Rahmstorf S, Coumou D. 2011. Increase of extreme events in a warming world. *Proceedings of the National Academy of Sciences* **108**(44): 17 905–17 909, doi:10.1073/pnas.1101766108.

Rhines P. 2015. Dynamical Meteorology — Rossby Waves. In: *Encyclopedia of Atmospheric Sciences (Second Edition)*, North GR, Pyle J, Zhang F (eds), Academic Press: Oxford, ISBN 978-0-12-382225-3, pp. 404 – 416, doi:10.1016/B978-0-12-382225-3.00346-7.

Rodwell MJ, Magnusson L, Bauer P, Bechtold P, Bonavita M, Cardinali C, Diamantakis M, Earnshaw P, Garcia-Mendez A, Isaksen L, Källen E, Klocke D, Lopez P, McNally T, Persson A, Prates F, Wedi N. 2013. Characteristics of occasional poor medium-range weather forecasts for Europe. *Bulletin of the American Meteorological Society* **94**(9): 1393–1405, doi:10.1175/BAMS-D-12-00099.1.

Rossby CG. 1940. Planetary flow patterns in the atmosphere. *Quarterly Journal of the Royal Meteorological Society* **66**: 68–97.

Rossby CG, Collaborators. 1939. Relation Between Variations in the Intensity of the Zonal Circulation of the Atmosphere and the Displacements of the Semi-Permanent Centers of Action. *Journal of Marine Research* **2**(1): 38–55, doi:10.1357/002224039806649023.

Röthlisberger M, Frossard L, Bosart LF, Keyser D, Martius O, Röthlisberger M, Frossard L, Bosart LF, Keyser D, Martius O. 2019. Recurrent Synoptic-Scale Rossby Wave Patterns and Their Effect on the Persistence of Cold and Hot Spells. *Journal of Climate* **32**(11): 3207–3226, doi:10.1175/JCLI-D-18-0664.1.

Röthlisberger M, Martius O, Wernli H. 2018. Northern Hemisphere Rossby Wave initiation events on the extratropical jet-A climatological analysis. *Journal of Climate* **31**(2): 743–760, doi:10.1175/JCLI-D-17-0346.1.

Röthlisberger M, Pfahl S, Martius O. 2016. Regional-scale jet waviness modulates the occurrence of midlatitude weather extremes. *Geophysical Research Letters* **43**(20): 10 989–10 997, doi:10.1002/2016GL070944.

Russo S, Dosio A, Graversen RG, Sillmann J, Carrao H, Dunbar MB, Singleton A, Montagna P, Barbola P, Vogt JV. 2014. Magnitude of extreme heat waves in present climate and their projection in a warming world. *Journal of Geophysical Research: Atmospheres* **119**(22): 12 500–12 512, doi:10.1002/2014JD022098.

Russo S, Sillmann J, Fischer EM. 2015. Top ten European heatwaves since 1950 and

their occurrence in the coming decades. *Environmental Research Letters* **10**(12): 124 003, doi:10.1088/1748-9326/10/12/124003.

Ruxton GD. 2006. The unequal variance t-test is an underused alternative to Student's t-test and the Mann-Whitney U test. doi:10.1093/beheco/ark016.

Saffin L, Gray SL, Methven J, Williams KD. 2017. Processes Maintaining Tropopause Sharpness in Numerical Models. *Journal of Geophysical Research: Atmospheres* **122**(18): 9611–9627, doi:10.1002/2017JD026879, URL `http://doi.wiley.com/10.1002/2017JD026879`.

Schär C, Vidale PL, Lüthi D, Frei C, Häberli C, Liniger MA, Appenzeller C. 2004. The role of increasing temperature variability in European summer heatwaves. *Nature* **427**(6972): 332–336, doi:10.1038/nature02300.

Schemm S, Schneider T. 2018. Eddy lifetime, number, and diffusivity and the suppression of eddy kinetic energy in midwinter. *Journal of Climate* **31**(14): 5649–5665, doi:10.1175/JCLI-D-17-0644.1.

Schneider T, Bischoff T, Płotka H. 2015. Physics of changes in synoptic midlatitude temperature variability. *Journal of Climate* **28**(6): 2312–2331, doi:10.1175/JCLI-D-14-00632.1.

Schneidereit A, Schubert S, Vargin P, Lunkeit F, Zhu X, Peters DH, Fraedrich K. 2012. Large-scale flow and the long-lasting blocking high over Russia: summer 2010. *Monthly Weather Review* **140**(9): 2967–2981, doi:10.1175/MWR-D-11-00249.1.

Schoon L, Zülicke C. 2018. A novel method for the extraction of local gravity wave parameters from gridded three-dimensional data: description, validation, and application. *Atmospheric Chemistry and Physics* **18**(9): 6971–6983, doi:10.5194/acp-18-6971-2018.

Schubert S, Wang H, Suarez M. 2011. Warm season subseasonal variability and climate extremes in the Northern Hemisphere: The role of stationary Rossby waves. *Journal of Climate* **24**(18): 4773–4792, doi:10.1175/JCLI-D-10-05035.1.

Schulzweida U. 2019. CDO User Guide. doi:10.5281/zenodo.2558193.

Screen JA, Simmonds I. 2014. Amplified mid-latitude planetary waves favour particular regional weather extremes. *Nature Climate Change* **4**(8): 704–709, doi:10.1038/nclimate2271.

Shepherd TG. 2014. Atmospheric circulation as a source of uncertainty in climate change projections. *Nature Geoscience* **7**(10): 703–708, doi:10.1038/ngeo2253.

Sillmann J, Croci-Maspoli M. 2009. Present and future atmospheric blocking and its impact on European mean and extreme climate. *Geophys. Res. Lett.* **36**(10), doi:10.1029/2009GL038259.

Simmons AJ, Hoskins BJ. 1979. The Downstream and Upstream Development of Unstable Baroclinic Waves. *Journal of the Atmospheric Sciences* **36**(7): 1239–1254, doi:10.1175/1520-0469(1979)036⟨1239:TDAUDO⟩2.0.CO;2.

Souders MB, Colle BA, Chang EKM. 2014a. A Description and Evaluation of an Automated Approach for Feature-Based Tracking of Rossby Wave Packets. *Monthly Weather Review* **142**(10): 3505–3527, doi:10.1175/MWR-D-13-00317.1.

Souders MB, Colle BA, Chang EKM. 2014b. The Climatology and Characteristics of Rossby Wave Packets Using a Feature-Based Tracking Technique. *Monthly Weather Review* **142**(10): 3528–3548, doi:10.1175/MWR-D-13-00371.1.

Sprenger M, Fragkoulidis G, Binder H, Croci-Maspoli M, Graf P, Grams CM, Knippertz P, Madonna E, Schemm S, Škerlak B, Wernli H. 2017. Global climatologies of Eulerian and Lagrangian flow features based on ERA-Interim. *Bulletin of the American Meteorological Society* **98**(8): 1739–1748, doi:10.1175/BAMS-D-15-00299.1.

Stocker T. 2014. *Climate change 2013: the physical science basis: Working group i contribution to the fifth assessment report of the intergovernmental panel on climate change*. Cambridge University Press.

Sun L, Chen G, Lu J. 2013. Sensitivities and mechanisms of the zonal mean atmospheric circulation response to tropical warming. *Journal of the Atmospheric Sciences* **70**(8): 2487–2504, doi:10.1175/JAS-D-12-0298.1.

Takaya K, Nakamura H. 2001. A Formulation of a Phase-Independent Wave-Activity Flux for Stationary and Migratory Quasigeostrophic Eddies on a Zonally Varying Basic Flow. *Journal of the Atmospheric Sciences* **58**(6): 608–627, doi:10.1175/1520-0469(2001)058⟨0608:AFOAPI⟩2.0.CO;2.

Teubler F, Riemer M. 2016. Dynamics of Rossby Wave Packets in a Quantitative Potential Vorticity–Potential Temperature Framework. *Journal of the Atmospheric Sciences* **73**(3): 1063–1081, doi:10.1175/JAS-D-15-0162.1.

Thorncroft CD, Hoskins BJ, McIntyre ME. 1993. Two paradigms of baroclinic-wave life-cycle behaviour. *Quarterly Journal of the Royal Meteorological Society* **119**(509): 17–55, doi:10.1002/qj.49711950903.

Torrence C, Compo GP. 1998. A practical guide to wavelet analysis. *Bulletin of the American Meteorological society* **79**(1): 61–78, doi:10.1175/1520-0477(1998)079⟨0061:APGTWA⟩2.0.CO;2.

Unidata. 2018. Network Common Data Form (NetCDF) [software]. doi:10.5065/D6H70CW6.

Vallis GK. 2017. *Atmospheric and oceanic fluid dynamics: Fundamentals and large-scale circulation, second edition*. Cambridge University Press: Cambridge, ISBN 9781107588417, doi:10.1017/9781107588417.

van der Walt S, Colbert SC, Varoquaux G. 2011. The NumPy Array: A Structure for Efficient Numerical Computation. *Computing in Science & Engineering* **13**(2): 22–30, doi:10.1109/MCSE.2011.37.

Wernli H, Sprenger M. 2007. Identification and ERA-15 Climatology of Potential Vorticity Streamers and Cutoffs near the Extratropical Tropopause. *Journal of the Atmospheric Sciences* **64**(5): 1569–1586, doi:10.1175/jas3912.1.

Wirth V, Eichhorn J. 2014. Long-lived Rossby wave trains as precursors to strong winter cyclones over Europe. *Quarterly Journal of the Royal Meteorological Society* **140**(680): 729–737, doi:10.1002/qj.2191.

Wirth V, Riemer M, Chang EKM, Martius O. 2018. Rossby Wave Packets on the Midlatitude Waveguide — A Review. *Monthly Weather Review* **146**(7): 1965–2001,

doi:10.1175/MWR-D-16-0483.1.

Wolf G, Wirth V. 2015. Implications of the Semigeostrophic Nature of Rossby Waves for Rossby Wave Packet Detection. *Monthly Weather Review* **143**(1): 26–38, doi:10.1175/MWR-D-14-00120.1.

Wolf G, Wirth V. 2017. Diagnosing the Horizontal Propagation of Rossby Wave Packets along the Midlatitude Waveguide. *Monthly Weather Review* **145**(8): 3247–3264, doi:10.1175/MWR-D-16-0355.1.

Yi H, Shu H. 2012. The improvement of the Morlet wavelet for multi-period analysis of climate data. *Comptes Rendus Geoscience* **344**(10): 483–497, doi:10.1016/j.crte.2012.09.007.

Zimin AV, Szunyogh I, Patil DJ, Hunt BR, Ott E. 2003. Extracting Envelopes of Rossby Wave Packets. *Monthly Weather Review* **131**(5): 1011–1017, doi:10.1175/1520-0493(2003)131⟨1011:EEORWP⟩2.0.CO;2.

Zschenderlein P, Fink AH, Pfahl S, Wernli H. 2019. Processes determining heat waves across different European climates. *Quarterly Journal of the Royal Meteorological Society* doi:10.1002/qj.3599.

Zschenderlein P, Fragkoulidis G, Fink AH, Wirth V. 2018. Large-scale Rossby wave and synoptic-scale dynamic analyses of the unusually late 2016 heatwave over Europe. *Weather* **73**(9): 275–283, doi:10.1002/wea.3278.

Acknowledgements

This work is the result of a very constructive collaboration with my supervisor His support in every technical and theoretical issue was invaluable. In addition, his management of the project was ideal and gave me the opportunity to elaborate on my ideas without losing track of our objectives. I would also like to acknowledge insightful discussions with the members of the Theoretical Meteorology group.

The research leading to these results has been done within the subproject "C4 - Coupling of planetary-scale Rossby wave trains to local extremes in heat waves over Europe" of the Transregional Collaborative Research Center SFB / TRR 165 "Waves to Weather" (www.wavestoweather.de) funded by the German Research Foundation (DFG).

Finally, I am grateful to the ECMWF and the Copernicus Climate Change Service for providing free access to the ERA-Interim and ERA5 reanalysis data. This work was also based on TIGGE data. TIGGE (The Interactive Grand Global Ensemble) is an initiative of the World Weather Research Programme (WWRP). I also gratefully acknowledge the computing time granted on the supercomputer Mogon at the Johannes Gutenberg University Mainz (hpc.uni-mainz.de).